Investigations of Molecular Orientational Orderings in Ferro-, Antiferro-, and Ferri-Electric Liquid Crystals by Polarized Raman Scattering

Naoki Hayashi

DOCTOR OF PHILOSOPHY

Department of Functional Molecular Science
School of Mathematical and Physical Science
The Graduate University for Advanced Studies

2002

Contents

Chapter 1

Preface

1.1 What is liquid crystal?

1.1.1 Discovery of liquid crystal phase

In 1888, Reinitzer, an Austrian botanist, synthesized the derivertive of a cholesteryl benzoate (Fig. 1.1) [1]. He found that it showed a viscous and clouded state at the temperature range between the a crystal and a liquid phases. Lehmann observed this material by polarizing optical microscope and found an optical anisotropy as well as a fluidity [2]. He had named this state 'flüssige Kristalle (liquid crystal).'

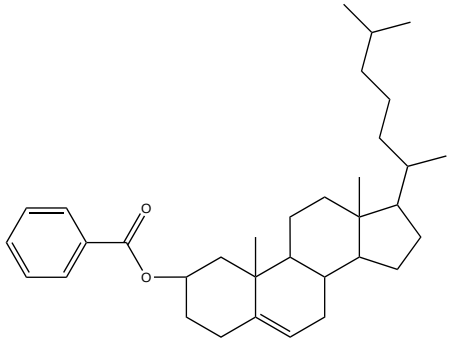

Figure 1.1: The chemical structure of the derivertive of cholesteryl benzoate synthesized by Reinitzer.

1.1.2 Classification of liquid crystals

Liquid crystals are categorized into 'thermotropic liquid crystals' and 'lyotropic liquid crystals' by their component materials. Fig. 1.2 shows the classification of the thermotropic liquid crystals with rod-like shape and low molecular weight. Friedel classified the thermotropic liquid crystal phases into three types on the basis of the observation by a polarizing microscope [3]; i.e., nematic (N), cholesteric (Ch), and smectic (Sm) phases.

The nematic phase has an order about one direction of the molecular orientation. The unit vector pointing the average of the orientations of the molecular long axes is defined as $\boldsymbol{n}$, which is called the $\boldsymbol{n}$-director. There is rotational symmetry of the molecular distribution about its long axis. The system has uniaxial symmetry with respect to the $\boldsymbol{n}$-director.

The cholesteric phase is the same as the nematic phase in terms of the thermodynamics. It can be treated as the nematic phase with helical structure. It is thus called 'chiral nematic phase (N*).' The $\boldsymbol{n}$-director rotates around the helical axis which is perpendicular to the $\boldsymbol{n}$-director.

The smectic phase has a layer structure as well as the orientational order. The phase is further classified into smectic A (SmA) and smectic C (SmC) phases. In the SmA phase, the $\boldsymbol{n}$-director is perpendicular to the layer (parallel to the layer normal) and the phase has uniaxial symmetry. On the other hand, in the SmC phase, the $\boldsymbol{n}$-director tilts with respect to the layer normal and thus the phase has biaxial symmetry. In this phase, introducing the $\boldsymbol{c}$-director is useful to describe this biaxial phase. The $\boldsymbol{c}$-director is the unit vector which is parallel to the projection of the $\boldsymbol{n}$-director on the smectic layer (Fig. 1.3) When a liquid crystal molecule has a chiral structure, the phase (SmC*) shows a helical structure. A helical pitch is very long ($\sim 10^{-1}$ - $\sim 10^{2}$ μm) as compared to the layer thickness which is comparable to the molecular length (a several nanometer). The helical axis is perpendicular to the smectic layer and $\boldsymbol{c}$-director rotates around the helical axis.

In the case of liquid crystal showing all phases described above, the phase sequence is

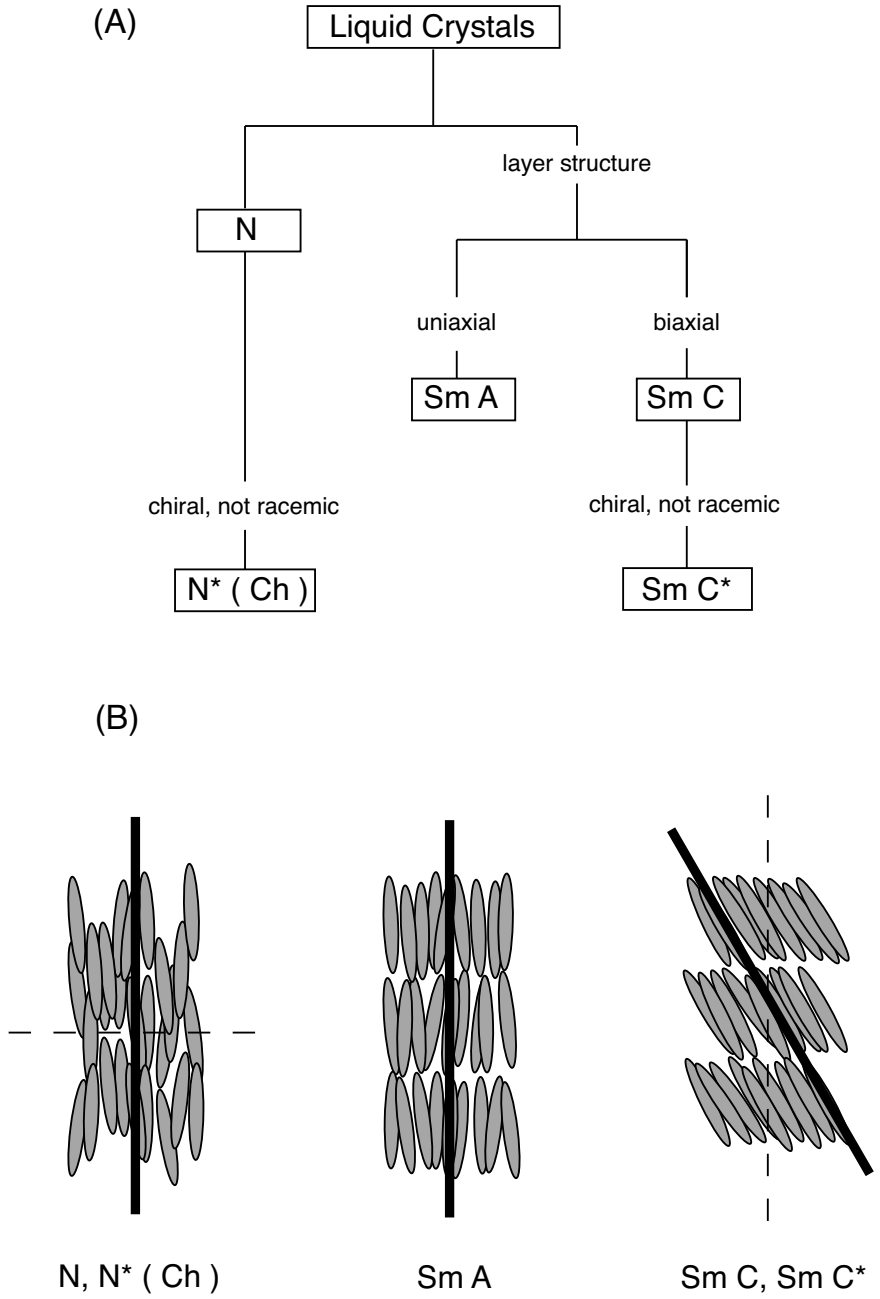

Figure 1.2: (A) The classification of the thermotropic liquid crystals with rod-like shape and low molecular weight. (B) The structures of the thermotropic liquid crystals. The liquid crystal molecules are represented by ellipsoids. The solid lines show the averages of the orientation of the molecular long axes, which are parallel to the $\boldsymbol{n}$-directors. The broken lines do the helical axes when they have helical structures.

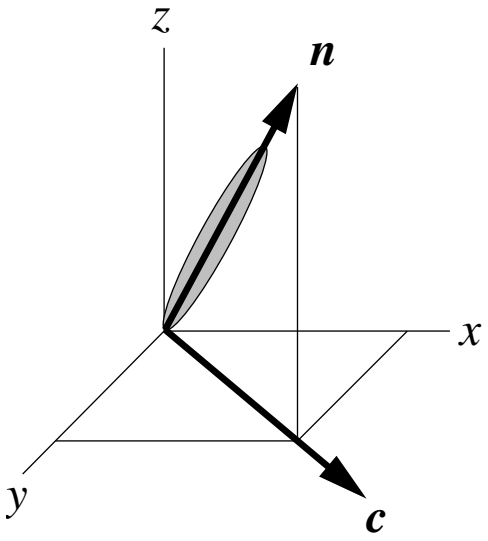

Figure 1.3: The $\boldsymbol{c}$-director in SmC phase. The xy plane is parallel to the smectic layer and z axis is perpendicular to the layer.

isotropic - N - SmA - SmC - crystal.

1.2 Molecular alignment in liquid crystal phase

1.2.1 Orientations of liquid crystal molecules at the surface of solid

The orientation of a liquid crystal molecule depends on various interactions between the molecules and a solid surface. The orientation can be controlled by coating glass plate surface with a proper reagent. When amphiphilic materials or silane couplers are used, the long axes of the molecules orient perpendicular to the substrate plates. This orientational state is called 'homeotropic molecular alignment' [Fig. 1.4(A).] When the materials like as polyvinyl alcohol, nylon, polyimide, etc. are used, the molecular long axes are oriented parallel to the substrate plates. This is 'homogeneous molecular alignment' [Fig. 1.4(B).]

A 'rubbing' procedure is frequently used to orient molecules in one direction. The 'rubbing' makes grooves or scratches on the surface of the coating material to induce

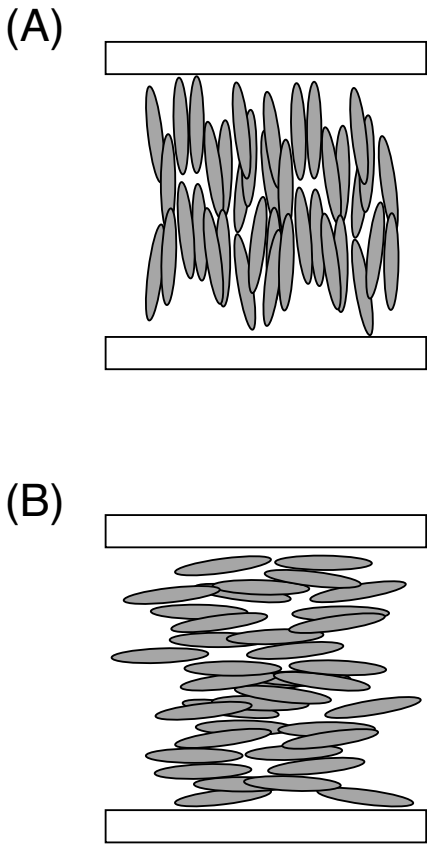

Figure 1.4: Homeotropic molecular alignment (A) and homogeneous molecular alignment (B) in nematic phase.

the anisotropy of the orientation of chains of the coating material molecules.

1.2.2 Bookshelf and chevron layer structure in the homogeneous molecular alignment of smectic phase

The homogeneous molecular alignment in SmA phase shows a bookshelf structure as shown in Fig. 1.5(A). The layer is perpendicular to the substrate surface. After the transition from the SmA to the SmC phase, the molecules tilt by Θ from the layer normal. This molecular tilt gives rise to the layer inclining with respect to the normal axis of the substrate surface [Fig. 1.5(B)] [4–9].

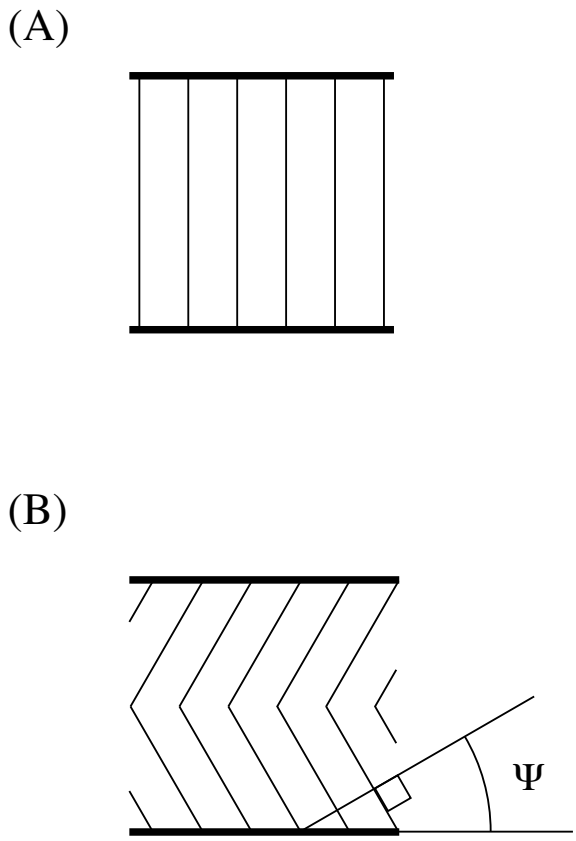

Figure 1.5: Bookshelf structure (A) and chevron layer structure (B) in the homogeneous molecular alignment of the smectic phase.

1.3 Molecular orientational distribution and the orientational order parameters

The nematic phase is uniaxial and thus the thermodynamic state of the phase is described with the molecular orientational distribution function, $f(\beta)$, where β is the angle between the individual molecular long axis and the $\boldsymbol{n}$-director. If the liquid crystal molecule is assumed as a rigid cylindrical rod, the molecular orientational distribution function $f(\beta)$ can be expanded in terms of Legendre polynomials $P_L(\cos\beta)$ [10, 11].

$$f(\beta) = \sum_{L=\text{even}} \frac{2L+1}{8\pi^2} \langle P_L(\cos\beta)\rangle \, P_L(\cos\beta). \tag{1.1}$$

Here, $\langle P_L(\cos\beta)\rangle$ is L-th order orientational order parameter and defined by

$$\langle P_L(\cos\beta)\rangle = \int_0^\pi \sin\beta d\beta P_L(\cos\beta) f(\beta). \tag{1.2}$$

The orientational order parameters can be evaluated by some spectroscopic methods [12]; i.e. polarized vibrational Raman scattering measurements [10, 13–17], EPR [18], NMR [19, 20], IR [21–23] and so on. Especially, the polarized vibrational Raman scattering measurements gives not only the second order parameter $\langle P_2(\cos\beta)\rangle$ but also the fourth one $\langle P_4(\cos\beta)\rangle$.

The description of the biaxial orientational distribution in the SmC* is much complicated. The biaxial molecular orientational distribution is described in Chapter 3.

1.4 Ferroelectric SmC* phase

The SmC phase belongs to the C_{2h} symmetry group. When a chirality is introduced to the liquid crystal molecule, the mirror and inversion operations are lost and the symmetry group is reduced to the C_2. The C_2 symmetry axis is perpendicular to the layer normal and the $\boldsymbol{c}$-director, or the molecular tilting plane. This phase is designated as SmC*. The SmC* phase has the spontaneous polarization parallel to the C_2 symmetry axis. In 1975, Meyer newly synthesized p-decyloxybenzylidene p'-amino 2-methyl butyl cinnamate (DOBAMBC) and confirmed the ferroelectricity in the SmC* phase [Fig. 1.6] [24].

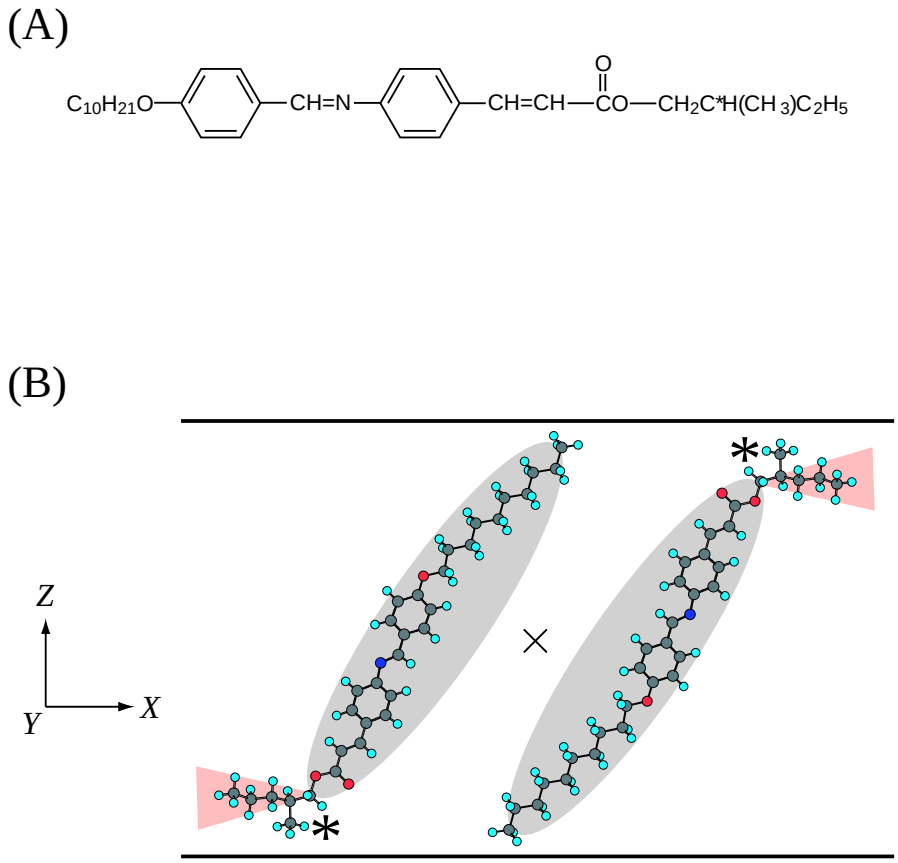

Figure 1.6: (A) The chemical structure of DOBAMBC. (B) The C_2 symmetry within a layer. The Z axis is parallel to the smectic layer normal and the X axis is parallel to the $\boldsymbol{c}$-director. The mark 'X' at the center of the layer indicates the C_2 symmetry axis. The spontaneous polarization appears parallel to this axis.

The electric field whose direction is perpendicular to the substrate plane (parallel to the Y axis) makes the uniform molecular orientation like as the left drawing of Fig. 1.7(a), where the liquid crystal molecules are directed in one direction throughout the cell. Now the tilting angle between the molecular long axis and the smectic layer normal (Z axis) is Θ and $\boldsymbol{c}$-director is parallel to the substrate plane (the XZ plane). When the electric field with opposite sign is applied, the molecules rotate around the Z axis with holding the angle Θ [the middle drawing of Fig. 1.7(a)] and are oriented to the opposite direction at last [the right drawing of Fig. 1.7(a)]. When the periodic electric field of a triangular waveform is applied, the electro-optic response [Fig. 1.7(b)] is observed by the optical microscope with the crossed Nicol configuration, where the smectic layer normal is parallel to one of the two polarizers. Generally, the molecular reorientation shows the hysteresis. This electro-optic response is called the 'bistable switching'.

1.4.1 Antiferro- and ferri-electric SmC* variant phases

Chandani *et al.* had discovered an antiferroelectricity in the SmC*-like phase of 4-(1-methyl-heptyloxycarbonyl)phenyl 4'-octyloxybiphenyl-4-carboxylate (MHPOBC) [25, 26]. This antiferroelectric smectic phase is designated as SmC_A* and shows the 'tristable switching' as shown in Fig. 1.8(b). This type of the switching is also characterized by the threshold and the hysteresis.

It was not long before the ferrielectric SmC*-ike phases, which are designated as SmC_γ* and SmC_α* phase, were also found in MHPOBC [26–29]. The SmC_γ* phase shows the 'tetrastable switching' [29] as shown in Fig. 1.9(b) and the SmC_α* phase does the electro-optic response with the multi-stable state or the nearly continuous change in the transmittance [30].

The one-dimensional Ising model [4,29,31–33] successfully explains the experimental results obtained from the electro-optic response [25, 29, 30], optical selective reflections [28], conoscopic observations [28, 30, 31], resonant X-ray diffractions [34, 35], and so on. The structures of the SmC* variant phases are shown in Fig. 1.10. In the Ising model, only anticlinic and synclinic molecular orderings in the adjacent layers are

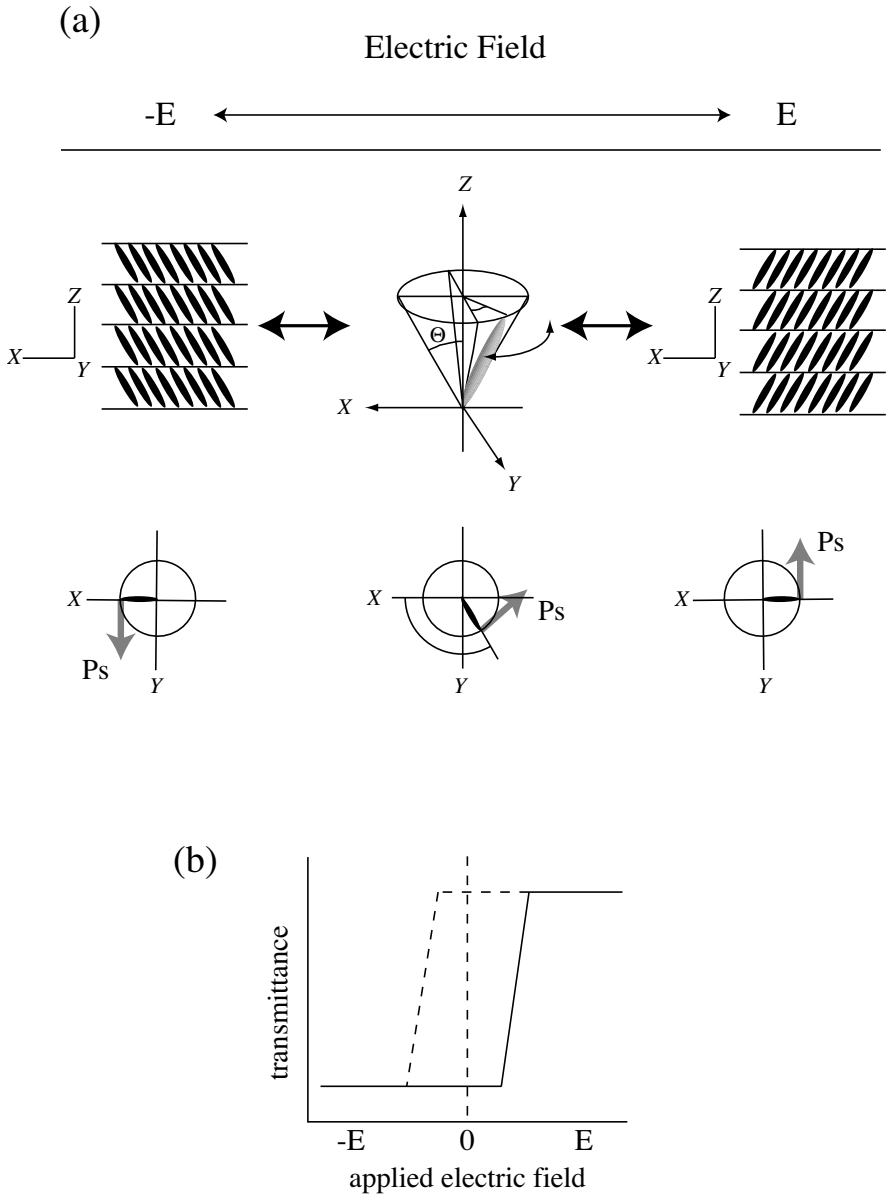

Figure 1.7: (a) The molecular reorientation induced by an electric field in the surface stabilized state. The Z axis is parallel to the smectic layer normal, the XZ plane is parallel to the substrate plane, and the XY plane is parallel to the layer. The electric field is applied parallel to the Y axis. (b) The bistable electro-optic response under the electric field of the triangular waveform with low frequency. The transmittance is observed by an optical microscope with the crossed Nicol configuration, where the molecular orientation at one of the ferroelectric state is parallel to one of the polarizers. The solid line shows the increasing process of the electric field and the broken line does the decreasing process.

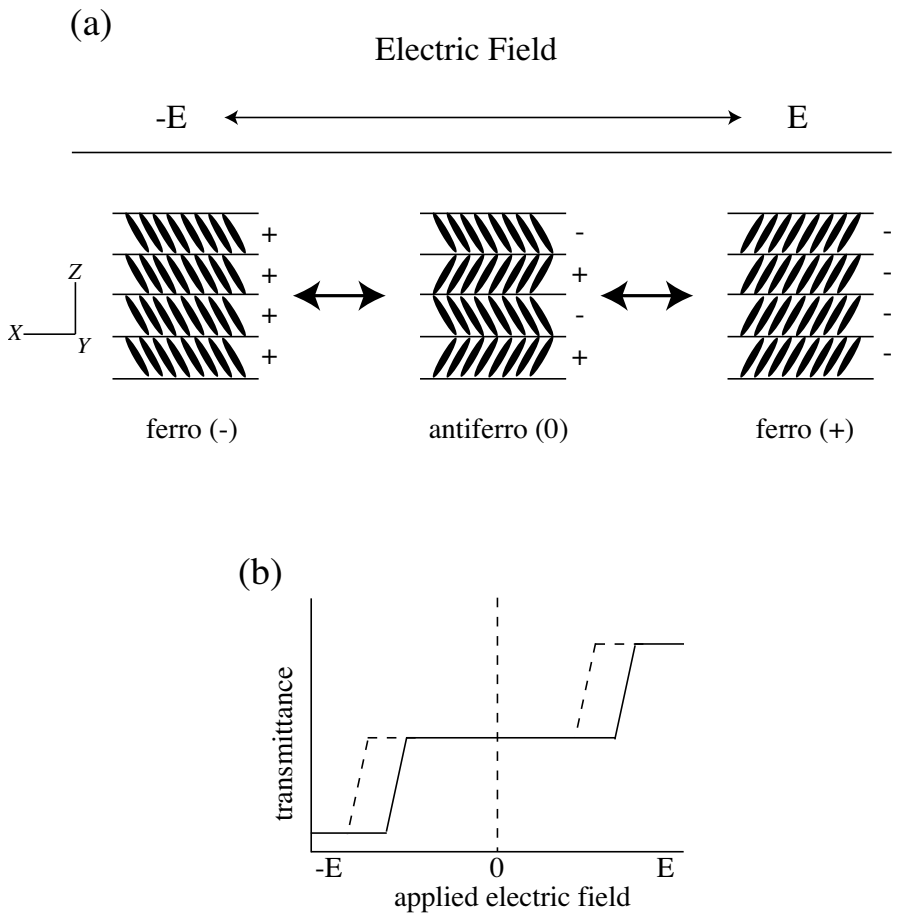

Figure 1.8: (a) The molecular orientation in the tristable electro-optic response. The Z axis is parallel to the smectic layer normal and the XZ plane is parallel to the substrate plane. The electric field is applied along the Y axis. The signs attached next to the layers represent the directions of the spontaneous polarization within the layer. (b) The tristable electro-optic response under the electric field of the triangular waveform with low frequency. The transmittance is observed by an optical microscope with the crossed Nicol configuration, where the molecular orientation at one of the ferroelectric state is parallel to one of the polarizers. The solid line shows the increasing process of the electric field and the broken line does the decreasing process.

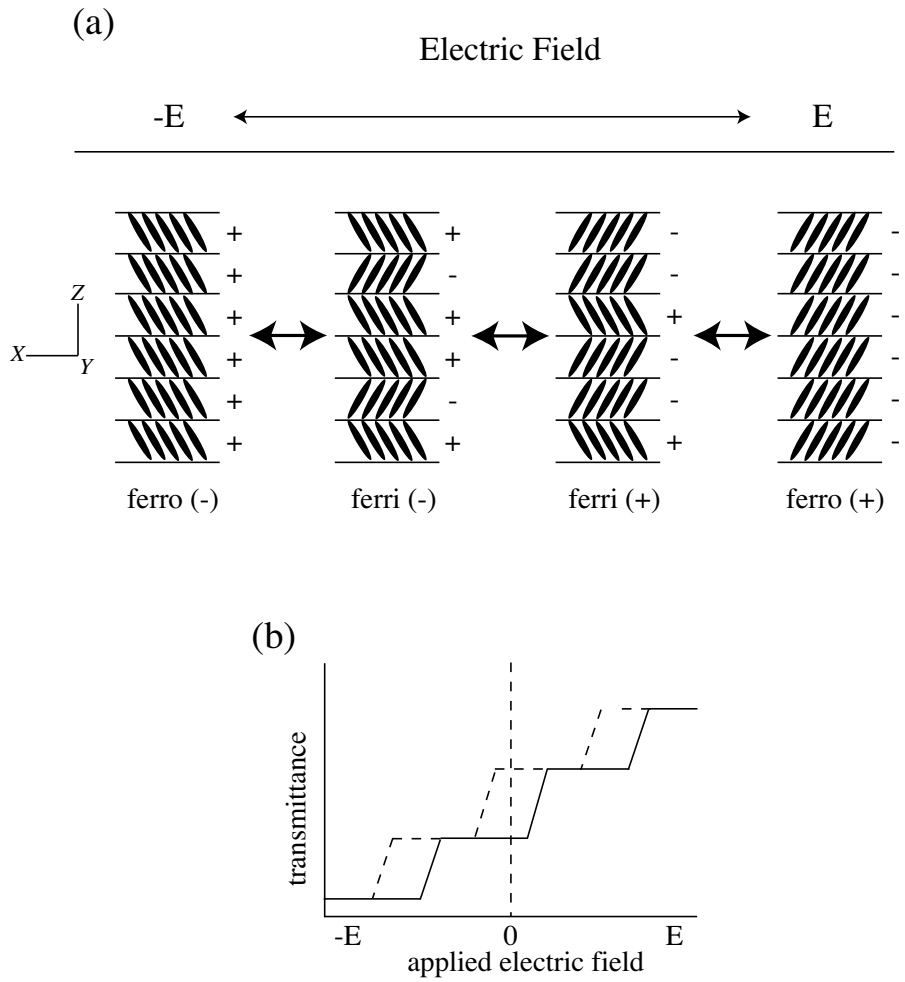

Figure 1.9: (a) The molecular orientation in the tetrastable electro-optic response. The Z axis is parallel to the smectic layer normal and XZ plane is parallel to the substrate plane. The electric field is applied along the Y axis. The signs attached next to the layers represent the directions of the spontaneous polarization within the layer. (b) The tristable electro-optic response under the electric field of the triangular waveform with low frequency. The transmittance is observed by an optical microscope with the crossed Nicol configuration, where the molecular orientation at one of the ferroelectric state is parallel to one of the polarizers. The solid line shows the increasing process of the electric field and the broken line does the decreasing process.

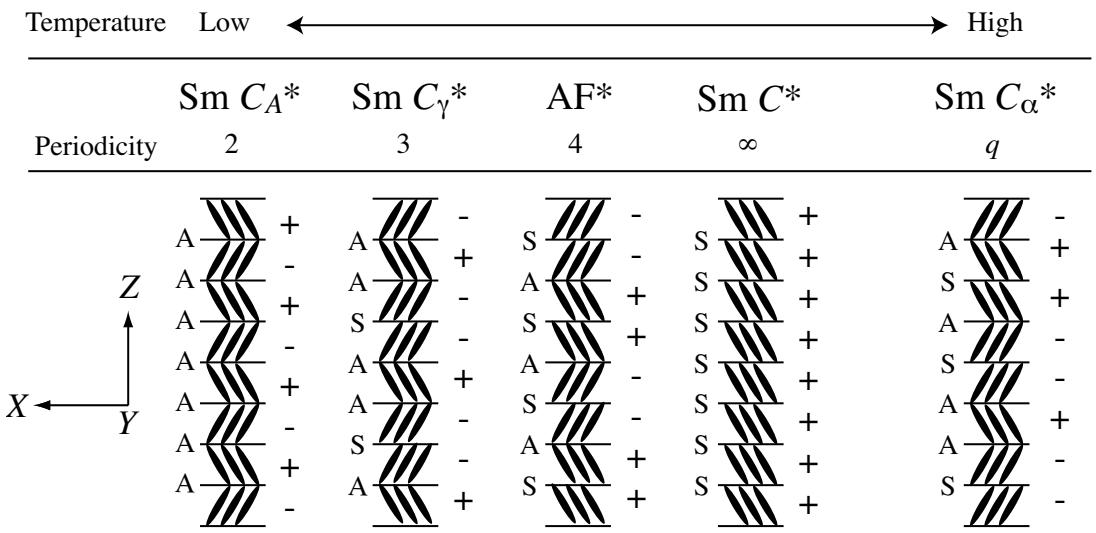

Figure 1.10: Structures of the SmC* and its variant phases given by the one-dimensional Ising model. The layer periodicity q varies with the temperature in SmC_α* phase. The signs on the rights of the layers represent the directions of the spontaneous polarization within the layer. 'A' and 'S' on the lefts of the layers indicate the anticlinic and synclinic molecular orderings, respectively.

allowed, hence the molecules always tilt in the XZ plane. In the SmC_A* phase with two-layer periodicity, the c-director turns left and right alternately; there are only anticlinic molecular orderings. The SmC_γ* phase has a three-layer periodicity. The synclinic molecular ordering appear once in a period. Okabe *et al.* found the another phase with four-layer periodicity [36]. The phase (designated as AF* phase) shows the antiferroelectricity. The anticlinic and synclinic molecular orderings emerge one after the other. A devil's staircase structure was proposed for peculiar SmC_α* phase [37, 38]. This phase does not show a single fixed structure. The layer periodicity and the arrangement of the anticlinic and synclinic molecular orderigns depend on the temperature.

1.5 The V-shaped electro-optic response

The electro-optic responses of the liquid crystals showing SmC* and its variant phases are characterized by the hysteresis and the threshold as shown in Figs. 1.7(b), 1.8(b),

and 1.9(b). Moreover, the switching is followed by the domain growth; a boat shaped domains [39] or the fingerprints-like domains along the smectic layers [40–42]. In 1996, Inui *et al.* reported the material which exhibits the thresholdless, hysteresis-free, letter 'V'-shaped electro-optic response in ferro- and antiferroelectric smectic phases [Fig. 1.11(c)] [43]. This peculiar switching has attracted much attention because of its potential application to liquid crystal displays [44–49].

The 'random switching model' [43, 50–53] is proposed for the mechanism of the V-shaped switching [Fig. 1.11(a)]. The frustration and the competition between the ferro- and antiferroelectricities bring about the reduction of the interlayer molecular interaction in the particular case. The surface of the sample cell is possible to break such a small interlayer interaction. Thus, the Langevin-type reorientation process of the $\boldsymbol{c}$-directors is occurred. The aligning process of the molecules is described as

$$\langle \cos\phi \rangle = \frac{\displaystyle\int_0^{\pi} \exp(x\cos\phi)\cos\phi d\phi}{\displaystyle\int_0^{\pi} \exp(x\cos\phi) d\phi} \tag{1.3}$$

by using a ratio of electric aligning energy, $p_{\mathrm{eff}}E$, to thermal agitating energy, kT_{eff},

$$x = p_{\mathrm{eff}}E/(kT_{\mathrm{eff}}). \tag{1.4}$$

Here, ϕ is an angle between the $\boldsymbol{c}$-director and the electric field, E is an electric field strength, and p_{eff} is the effective dipole moment.

On the other hand, Takezoe *et al.* [54], Park *et al.* [23,55], Rudquist *et al.* [56], and Clark *et al.* [57] asserted the charge stabilization and/or the highly collective rotation of the local in-plane directors on the SmC^* tilt cone in the macroscopic scale, and that the frustration did not play any essential role [Fig. 1.11(b)].

1.6 The aim and the abstracts

The polarized vibrational Raman scattering measurement has some distinguished advantages. First, the vibrational Raman scattering line is accompanied by the vibrational normal coordinate of a molecule, so the polarized signal of the specific Raman

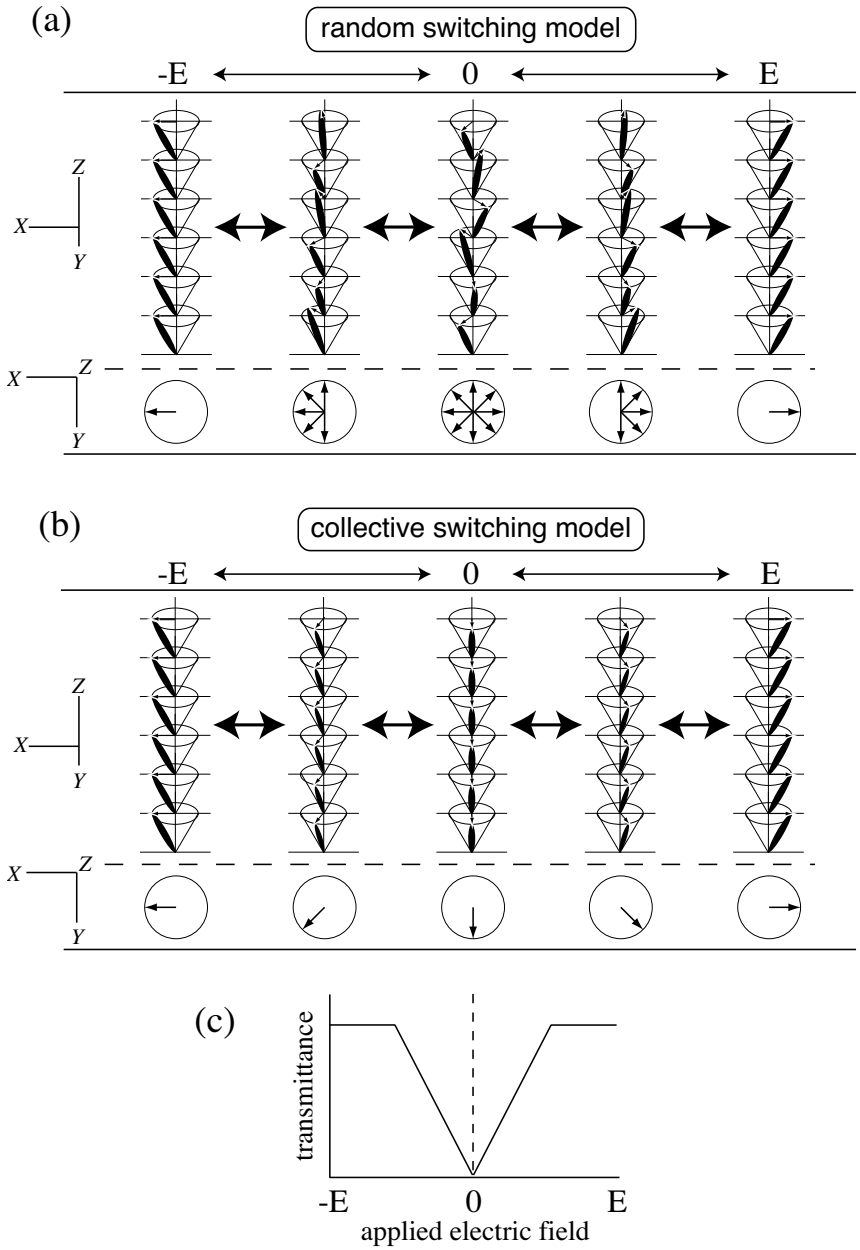

Figure 1.11: (a) The random switching model in the V-shaped electro-optic response. The Z axis is parallel to the smectic layer normal and the XZ plane is parallel to the substrate plane. The electric field is applied along the Y axis. The arrows in the circles represent the $\boldsymbol{c}$-directors in the XY plane. The distribution of the $\boldsymbol{c}$-directors is described by Eq. (1.3). (b) The collective switching model in the V-shaped electro-optic response. (c) The V-shaped electro-optic response under the electric field of the triangular waveform with low frequency. The transmittance is observed by an optical microscope with the crossed Nicol configuration, where the layer normal is parallel to one of the polarizers.

line gives the orientational information about the local structure of a molecule. Secondly, the Raman scattering gives not only the second-order parameter $\langle P_2(\cos\beta)\rangle$ but also the fourth-order one $\langle P_4(\cos\beta)\rangle$. The $\langle P_4(\cos\beta)\rangle$ exhibits a larger sensitivity than $\langle P_2(\cos\beta)\rangle$, so the polarized Raman scattering measurement is much effective in investigating the subtle change or difference in the molecular orientational distribution of the liquid crystal than the other method. The combination of synclinic and anticlinic arrangements characterizes the SmC's variant phase, as mentioned before. The thermal agitation triggers the change of the combination and leads the phase transition within the SmC's variant phase. The change of the combination caused by the distribution of the $\boldsymbol{c}$-director alters the biaxiality in the phase. The observation of the biaxiality by the vibrational polarized Raman scattering can trace the mechanism of the phase transition.

This thesis contains six chapters. The procedure how the orientational order parameters are obtained from the polarized Raman intensities is described in Chapter 2. The improved analysis of the polarized Raman scattering provides more precise order parameters than those ever reported. The order parameters can be obtained even from the small Raman intensities in the time-resolved measurement during the electro-optic response of a thin sample cell ($\sim 1\mu$m). In Chapter 3, the analysis is applied to the system of MHPOBC in the thick homogeneous alignment cell [published in Phys. Rev. E, 63, 02176 (2001)]. The close relation of a biaxial molecular ordering to the successive transition between the SmC* variant phases is investigated. The molecular reorientation induced by an external electric filed in SmC_A* phase is studied in Chapter 4 [Jpn. J. Appl. Phys., in press (2002)]. The reorientation can be described with the interlayer molecular interaction, the spontaneous polarization, and the field strength. The theoretical model proposed before is verified there. In Chapter 5, the molecular orientational distributions of two types of the liquid crystal showing V-shaped switching are examined [published in Phys. Rev. Lett., 87, 015701 (2001) and Phys. Rev. E, 65, 041714 (2002)]. The 'random' and 'collective' models have a difference in the molecular distribution during the switching as described before. The difference can be detected by the improved analysis of the polarized Raman scattering. The process of the molecular reorientation in the V-shaped switching is discussed in terms of the

interlayer molecular interaction. The interlayer molecular interaction is evaluated by the dependence of the $\boldsymbol{c}$-director distribution on the dc electric field strength. The summary is given in Chapter 6.

Chapter 2

Determination of Orientational Order Parameters by Polarized Raman Scattering Measurement

Polarized vibrational Raman scattering measurement provides both the second- and fourth-order orientational order parameters. There is the additional advantage that a glass sample cell can be used for the polarized Raman scattering measurement. The texture of the sample can be observed by an optical microscope and the electro-optic response can be monitored during the polarized Raman scattering measurement. On the contrary to these advantages, the birefringence in the ordered liquid crystal brings complications to the data analysis in the polarized Raman scattering measurement. To avoid the disturbance by the birefringence, the polarized Raman scattering measurement has been restricted to only the configurations in which the polarization directions of the incident and scattered lights are parallel or perpendicular to the optic axis of the liquid crystal in the nematic and SmA phases with uniaxial symmetry so far.

In this chapter, it is shown that precise order parameters can be obtained by the analysis of the polarized Raman intensities depending on the polarization direction of the incident and scattered lights with respect to the molecular ordering direction when the optical effects are corrected properly.

2.1 Orientational order parameters and polarized Raman intensities in the phase with uniaxial symmetry

Followings are presupposed for simplifications in the analysis of polarized Raman intensities here.

1. A Raman tensor of a vibrational mode for a particular molecule has uniaxial symmetry:

$$\alpha^{\mathrm{Mol}} = \begin{pmatrix} \alpha_{\perp} & & \\ & \alpha_{\perp} & \\ & & \alpha_{\parallel} \end{pmatrix}. \tag{2.1}$$

2. The principal axis of the Raman tensor with the largest value is parallel to the molecular long axis. This indicates the distribution function of the principal axis of the Raman tensor is identical with the distribution function of the liquid crystal molecule.

3. The liquid crystal phase also has uniaxial symmetry, and the symmetry axis is parallel to the substrate plate of a sample cell; nematic or Sm A phase in the homogeneous molecular alignment cell.

2.1.1 Description of Raman tensor in molecular fixed coordinate system

The Raman scattering from a molecule is considered. Here, a molecular fixed coordinate system is defined by the (x, y, z)-Cartesian coordinate where the z axis is parallel to the molecular long axis. The polarizability tensor of the Raman scattering for a molecule

is given in the molecular coordinate system by

$$\begin{aligned}\alpha_{ij}^{\mathrm{Mol}} &= \hat{n}_i^{\mathrm{Mol}} \cdot \alpha^{\mathrm{Mol}} \cdot \hat{n}_j^{\mathrm{Mol}} \\ &= \begin{pmatrix} n_{i1}^{\mathrm{Mol}} & n_{i2}^{\mathrm{Mol}} & n_{i3}^{\mathrm{Mol}} \end{pmatrix} \cdot \begin{pmatrix} \alpha_\perp & & \\ & \alpha_\perp & \\ & & \alpha_\parallel \end{pmatrix} \cdot \begin{pmatrix} n_{j1}^{\mathrm{Mol}} \\ n_{j2}^{\mathrm{Mol}} \\ n_{j3}^{\mathrm{Mol}} \end{pmatrix}, \end{aligned} \tag{2.2}$$

where $\hat{n}_i^{\mathrm{Mol}}$ and $\hat{n}_j^{\mathrm{Mol}}$ are the unit vectors showing the polarization directions of incident light and scattered lights, respectively. The superscripts 'Mol' indicate that the vectors are defined in the molecular fixed coordinate system. The polarization vectors are rewritten with irreducible spherical tensors $\hat{e}_{-q}^{\mathrm{Mol}}$ as

$$\hat{n}_l^{\mathrm{Mol}} = \sum_q (-1)^q n_l^{\mathrm{Mol},(q)} \hat{e}_{-q}^{\mathrm{Mol}}, \quad l = i, j, \tag{2.3}$$

with

$$\hat{e}_0^{\mathrm{Mol}} = \hat{z}, \quad \hat{e}_{\pm 1}^{\mathrm{Mol}} = \mp \frac{1}{\sqrt{2}} (\hat{x} \pm i\hat{y}). \tag{2.4}$$

$\alpha_{ij}^{\mathrm{Mol}}$ is given by Eq. (2.3) and (2.4) as

$$\alpha_{ij}^{\mathrm{Mol}} = \sum_{q,q'} (-1)^{q-q'} n_i^{\mathrm{Mol},(q)} n_j^{\mathrm{Mol},(-q')} \alpha_{-qq'}^{\mathrm{Mol}} \tag{2.5}$$

with

$$\alpha_{-qq'}^{\mathrm{Mol}} = \hat{e}_{-q}^{\mathrm{Mol}} \cdot \alpha^{\mathrm{Mol}} \cdot \hat{e}_{q'}^{\mathrm{Mol}}. \tag{2.6}$$

$n_i^{\mathrm{Mol},(q)}$ and $n_j^{\mathrm{Mol},(q)}$ are the spherical tensor operators of rank 1. Their linear combinations can produce the spherical tensor operators of the rank 0, 1, and 2:

$$T_{km}^{\mathrm{Mol}}(ij) = \sum_{q,q'} (-1)^m (2k+1)^{1/2} \begin{pmatrix} 1 & 1 & k \\ q & -q' & -m \end{pmatrix} n_i^{\mathrm{Mol},(q)} n_j^{\mathrm{Mol},(-q')}, \tag{2.7}$$

where

$$\begin{pmatrix} 1 & 1 & k \\ q & -q' & -m \end{pmatrix} \tag{2.8}$$

is the so-called 3-j symbol. Here, $k = 0, 1, 2$, $|m| \leq k$, and $q - q' = m$. The inverse transformation of Eq. (2.7) is given by

$$n_i^{\mathrm{Mol},(q)} n_j^{\mathrm{Mol},(-q')} = \sum_{k,m} (-1)^m (2k+1)^{1/2} \begin{pmatrix} 1 & 1 & k \\ q & -q' & -m \end{pmatrix} T_{km}^{\mathrm{Mol}}(ij). \tag{2.9}$$

The substitution of Eq. (2.9) for Eq. (2.5) gives

$$\alpha_{ij}^{\mathrm{Mol}} = \sum_{k,m} (-1)^m \alpha^{\mathrm{Mol}}(k,-m) T_{km}^{\mathrm{Mol}}(ij), \tag{2.10}$$

where

$$\alpha^{\mathrm{Mol}}(k,-m) = \sum_{q,q'} (-1)^{q-q'} (2k+1)^{1/2} \begin{pmatrix} 1 & 1 & k \\ q & -q' & -m \end{pmatrix} \alpha_{-qq'}^{\mathrm{Mol}}. \tag{2.11}$$

Let us calculate $\alpha^{\mathrm{Mol}}(0,0)$ as an example. Equations (2.6) and (2.10) give

$$\alpha^{\mathrm{Mol}}(0,0) = \sum_{q,q'} (-1)^{q-q'} \begin{pmatrix} 1 & 1 & 0 \\ q & -q' & 0 \end{pmatrix} \alpha_{-qq'}^{\mathrm{Mol}}, \tag{2.12}$$

where (q,q') is $(0,0)$, $(1,1)$, and $(-1,-1)$. The $\alpha_{-qq'}^{\mathrm{Mol}}$ are calculated as

$$\alpha_{00}^{\mathrm{Mol}} = \hat{e}_0^{\mathrm{Mol}} \cdot \alpha^{\mathrm{Mol}} \cdot \hat{e}_0^{\mathrm{Mol}} = \alpha_{zz}^{\mathrm{Mol}} = \alpha_{\parallel}, \tag{2.13}$$

$$\alpha_{-11}^{\mathrm{Mol}} = \hat{e}_{-1}^{\mathrm{Mol}} \cdot \alpha^{\mathrm{Mol}} \cdot \hat{e}_1^{\mathrm{Mol}} = \frac{1}{\sqrt{2}}(\hat{x} - i\hat{y}) \cdot \alpha^{\mathrm{Mol}} \cdot \left(-\frac{1}{\sqrt{2}}\right)(\hat{x} + i\hat{y}) = -\alpha_{\perp}, \tag{2.14}$$

$$\alpha_{1-1}^{\mathrm{Mol}} = \hat{e}_1^{\mathrm{Mol}} \cdot \alpha^{\mathrm{Mol}} \cdot \hat{e}_{-1}^{\mathrm{Mol}} = -\alpha_{\perp}. \tag{2.15}$$

Thus,

$$\alpha^{\mathrm{Mol}}(0,0) = -\frac{1}{\sqrt{3}}(2\alpha_{\perp} + \alpha_{\parallel}) \tag{2.16}$$

is obtained. Similarly,

$$\alpha^{\mathrm{Mol}}(1,0) = -\frac{i}{\sqrt{2}}(\alpha_{xy}^{\mathrm{Mol}} - \alpha_{yx}^{\mathrm{Mol}}) = 0, \tag{2.17}$$

$$\alpha^{\mathrm{Mol}}(1,\pm 1) = -\frac{1}{2}\left[(\alpha_{zx}^{\mathrm{Mol}} - \alpha_{xz}^{\mathrm{Mol}}) \pm i(\alpha_{zy}^{\mathrm{Mol}} - \alpha_{yz}^{\mathrm{Mol}})\right] = 0, \tag{2.18}$$

$$\alpha^{\mathrm{Mol}}(2,0) = -\frac{1}{\sqrt{6}}(\alpha_{xx}^{\mathrm{Mol}} + \alpha_{yy}^{\mathrm{Mol}} - 2\alpha_{zz}^{\mathrm{Mol}}) = \sqrt{\frac{2}{3}}(\alpha_{\parallel} - \alpha_{\perp}), \tag{2.19}$$

$$\alpha^{\mathrm{Mol}}(2,\pm 1) = \mp\frac{1}{2}\left[(\alpha_{zx}^{\mathrm{Mol}} + \alpha_{xz}^{\mathrm{Mol}}) \pm i(\alpha_{zy}^{\mathrm{Mol}} + \alpha_{yz}^{\mathrm{Mol}})\right] = 0 \tag{2.20}$$

and

$$\alpha^{\mathrm{Mol}}(2,\pm 2) = \frac{1}{2}\left[(\alpha_{xx}^{\mathrm{Mol}} - \alpha_{yy}^{\mathrm{Mol}}) \pm i(\alpha_{xy}^{\mathrm{Mol}} + \alpha_{yx}^{\mathrm{Mol}})\right] = 0. \tag{2.21}$$

2.1.2 Description of Raman tensor in laboratory fixed coordinate system

Now let us calculate $\alpha_{ij}^{\mathrm{Lab}}$ defined for a molecule in the laboratory fixed coordinate system which is the reference system for the measurement. The rotation operator

$D(\Omega)$ is defined to express the transformation from the molecular fixed coordinate system to the laboratory fixed one. Ω represents (α, β, γ) which are the Euler angles showing the rotational transformation between the coordinate systems. When $D(\Omega)$ is described in terms of the Wigner rotation matrix, $T^{\mathrm{Mol}}_{km}(ij)$ is related to the laboratory fixed coordinate system by

$$T^{\mathrm{Mol}}_{km}(ij) = D(\Omega)F^{\mathrm{Lab}}_{km}(ij)D^{-1}(\Omega) = \sum_{m'} F^{\mathrm{Lab}}_{km'}(ij)D^{(k)*}_{mm'}(\Omega), \tag{2.22}$$

where the superscripts 'Lab' stand for the definition in the laboratory fixed coordinate system. With substituting Eq. (2.22) for Eq. (2.10),

$$\alpha^{\mathrm{Lab}}_{ij} = \sum_{k,m,m'} F^{\mathrm{Lab}}_{km'}(ij)D^{(k)*}_{mm'}(\Omega)\alpha^{\mathrm{Mol}}(k,-m). \tag{2.23}$$

$F^{\mathrm{Lab}}_{km'}(ij)$ is given by

$$F^{\mathrm{Lab}}_{km'}(ij) = \sum_{q,q'}(-1)^{m'}(2k+1)^{1/2}\begin{pmatrix} 1 & 1 & k \\ q & -q' & -m' \end{pmatrix} n_i^{\mathrm{Lab},(q)} n_j^{\mathrm{Lab},(-q')}. \tag{2.24}$$

2.1.3 Polarized Raman scattering intensity

Here, the polarized Raman intensities obtained for the homogeneous molecular alignment cell in the actual measurement are calculated. The 'laboratory' fixed coordinate is constituted by X, Y, and Z axes (Fig. 2.1). This coordinate system describes the averaged molecular orientation. The Z axis is parallel to the $\boldsymbol{n}$-director and the XZ plane is parallel to the substrate plane of the sample cell. The 'measurement' coordinate system is fixed on the polarized light used in the measurement. The incident light comes into the cell along the Y_{meas} and Y axes, and the polarization direction is parallel to the Z_{meas} axis. The scattered light goes back along the Y_{meas} and Y axes, that is, the back scattering configuration is adopted. The polarization directions of the scattered lights parallel to the Z_{meas} and X_{meas} are chosen here.

The angles between the Z axis and the polarization directions of the incident and scattered lights are ω and ω', respectively. The electric fields of the incident and the scattered light at the depth Y from the surface, $\boldsymbol{E}_{(Y)}(\omega)$ and $\boldsymbol{E}'_{(Y)}(\omega')$, are described as

$$\boldsymbol{E}_{(Y)}(\omega) = T_X \sin\omega e^{-\delta X}\hat{X} + T_Z \cos\omega \hat{Z} \tag{2.25}$$

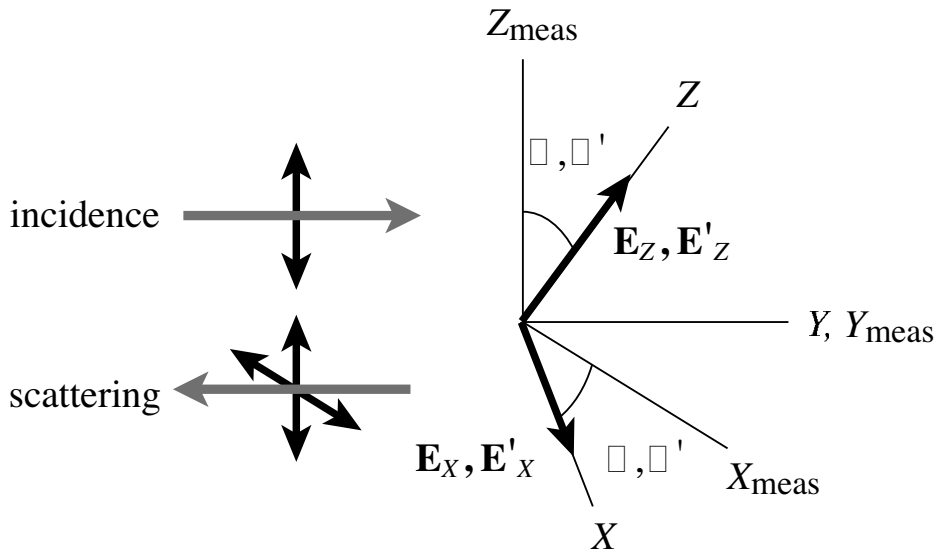

Figure 2.1: Laboratory fixed coordinate system

and

$$\boldsymbol{E}'_{(Y)}(\omega') = T'_X \sin\omega' e^{-\delta X'} \hat{X} + T'_Z \cos\omega' \hat{Z}. \tag{2.26}$$

δX and $\delta X'$ are the phase differences between the Z and X polarized lights at the incidence and the scattering, respectively;

$$\delta X = \frac{2\pi Y(n_Z - n_X)}{\lambda} = \frac{2\pi Y \Delta n}{\lambda} \tag{2.27}$$

and

$$\delta X' = \frac{2\pi Y \Delta n}{\lambda'}, \tag{2.28}$$

where λ and λ' are the wavelengths of the incident and scattered lights, and n_M ($M = Z$ and X) are the principal refractive indices of the liquid crystal sample along the M axis. T_M and T'_M are the transmission coefficients for the M components of the electric fields at the interface between the substrate and the liquid crystal. They are calculated by

$$T_M = \frac{2n_g}{n_g + n_M} \tag{2.29}$$

and

$$T'_M = \frac{2n_M}{n_g + n_M}, \tag{2.30}$$

where n_g is the refractive index of the substrate plate. $\boldsymbol{E}_{(Y)}(\omega)$ is rewritten in terms of the irreducible spherical tensors as

$$\boldsymbol{E}_{(Y)}(\omega) = \sum_q (-1)^q n_i^{\mathrm{Lab},(q)} \hat{e}_{-q}^{\mathrm{Lab}}. \tag{2.31}$$

Here,

$$\hat{e}_0^{\mathrm{Lab}} = \hat{Z}, \quad \hat{e}_{\pm 1}^{\mathrm{Lab}} = \mp \frac{1}{\sqrt{2}} (\hat{Y} \pm i\hat{X}), \tag{2.32}$$

then we have

$$n_i^{\mathrm{Lab},(0)}(\omega) = T_Z \cos\omega, \tag{2.33}$$

$$n_i^{\mathrm{Lab},(1)}(\omega) = -\frac{i}{\sqrt{2}} T_X \sin\omega e^{-i\delta X}, \tag{2.34}$$

and

$$n_i^{\mathrm{Lab},(-1)}(\omega) = -\frac{i}{\sqrt{2}} T_X \sin\omega e^{-i\delta X}. \tag{2.35}$$

$\boldsymbol{E}'_{(Y)}(\omega')$ is also represented by similar expressions:

$$n_j^{\mathrm{Lab},(0)}(\omega') = T'_Z \cos\omega, \tag{2.36}$$

$$n_j^{\mathrm{Lab},(1)}(\omega') = -\frac{i}{\sqrt{2}} T'_X \sin\omega e^{-i\delta' X}, \tag{2.37}$$

and

$$n_j^{\mathrm{Lab},(-1)}(\omega') = -\frac{i}{\sqrt{2}} T'_X \sin\omega e^{-i\delta' X}. \tag{2.38}$$

Only $\alpha(0,0)$ and $\alpha(2,0)$ are taken into consideration as seen in Eqs. (2.16)–(2.21), so that, the calculations are carried out for $(k, m, m') = (0,0,0), (2,0,0), (2,0,\pm 1)$, and $(2,0,\pm 2)$.

The case of $\omega = \omega'$ is considered. $F_{00}^{\mathrm{Lab}}(ij)$ is calculated as

$$\begin{aligned}
F_{00}^{\mathrm{Lab}}(ij) =& \sum_{q,q'} \begin{pmatrix} 1 & 1 & 0 \\ q & -q' & 0 \end{pmatrix} n_i^{\mathrm{Lab},(q)}(\omega) n_j^{\mathrm{Lab},(-q')}(\omega') \\
=& \begin{pmatrix} 1 & 1 & 0 \\ 0 & 0 & 0 \end{pmatrix} T_Z T_Z' \cos^2\omega \\
&+ \begin{pmatrix} 1 & 1 & 0 \\ 1 & -1 & 0 \end{pmatrix} \left(-\frac{i}{\sqrt{2}}\right)^2 T_X T_X' \sin^2\omega \cdot e^{-i\delta X} e^{-i\delta X'} \\
&+ \begin{pmatrix} 1 & 1 & 0 \\ 1 & -1 & 0 \end{pmatrix} \left(-\frac{i}{\sqrt{2}}\right)^2 T_X T_X' \sin^2\omega \cdot e^{-i\delta X} e^{-i\delta X'} \\
=& -\frac{1}{\sqrt{3}} \left[T_Z T_Z' \cos^2\omega + T_X T_X' \sin^2\omega \cdot e^{-i(\delta X + \delta X')} \right]. \qquad (2.39)
\end{aligned}$$

Similarly,

$$F_{20}^{\mathrm{Lab}}(ij) = \frac{1}{\sqrt{6}} \left[2T_Z T_Z' \cos^2\omega - T_X T_X' \sin^2\omega \cdot e^{-i(\delta X + \delta X')} \right], \qquad (2.40)$$

$$F_{21}^{\mathrm{Lab}}(ij) = -\frac{i}{2} \left[\cos\omega \sin\omega \cdot \left(T_X T_Z' e^{-i\delta X} + T_X' T_Z e^{-i\delta X'} \right) \right] = F_{2-1}^{\mathrm{Lab}}(ij), \qquad (2.41)$$

and

$$F_{22}^{\mathrm{Lab}}(ij) = -\frac{i}{2} T_X T_X' \sin^2\omega \cdot e^{-i(\delta X + \delta X')} = F_{2-2}^{\mathrm{Lab}}(ij). \qquad (2.42)$$

Thus, Eq. (2.23) is calculated as

$$\begin{aligned}
\alpha_{ij,(Y)}(\omega,\omega) =& \sum_{k,m,m'} F_{km'}^{L}(ij) D_{mm'}^{(k)*}(\Omega) \alpha^{\mathrm{Mol}}(k,-m) \\
=& a \left[T_Z T_Z' \cos^2\omega + T_X T_X' \sin^2\omega \cdot e^{-i(\delta X + \delta X')} \right] D_{00}^{(0)*}(\Omega) \\
&+ \frac{1}{3} b \left[2T_Z T_Z' \cos^2\omega - T_X T_X' \sin^2\omega \cdot e^{-i(\delta X + \delta X')} \right] D_{00}^{(2)*}(\Omega) \\
&- \frac{i}{\sqrt{6}} b \cos\omega \sin\omega \cdot (T_X T_Z' e^{-i\delta X} + T_X' T_Z e^{-i\delta X'}) \\
&\times \left[D_{01}^{(2)*}(\Omega) + D_{0-1}^{(2)*}(\Omega) \right] \\
&- \frac{i}{\sqrt{6}} b \left[T_X T_X' \sin^2\omega \cdot e^{-i(\delta X + \delta X')} \right] \left[D_{02}^{(2)*}(\Omega) + D_{0-2}^{(2)*}(\Omega) \right], \qquad (2.43)
\end{aligned}$$

where

$$\alpha^{\mathrm{Mol}}(0,0) = -\frac{1}{\sqrt{3}}(2\alpha_\perp + \alpha_\parallel) = -\sqrt{3}a \qquad (2.44)$$

and

$$\alpha^{\mathrm{Mol}}(2,0) = \frac{2}{\sqrt{6}}(\alpha_{\parallel} - \alpha_{\perp}) = \frac{2}{\sqrt{6}}b. \tag{2.45}$$

The instantaneous polarized Raman intensity for one molecule at Y is given by $\alpha^*_{ij,(Y)}\alpha_{ij,(Y)}$. The liquid crystal molecule undergoes thermal agitation. When enough molecules in the same circumstance are measured, the polarized Raman intensity at Y, $I_{(Y)}(\omega,\omega')$, is given by

$$I_{(Y)}(\omega,\omega') \equiv \langle \alpha^*_{ij,(Y)}\alpha_{ij,(Y)} \rangle = \int d\Omega \; \alpha^*_{ij,(Y)}\alpha_{ij,(Y)} f(\Omega), \tag{2.46}$$

where $f(\Omega)$ is the orientational molecular distribution function. Here, the Clebsch-Gordan series expansion is used:

$$D^{(j1)*}_{m1n1}(\Omega)\, D^{(j2)}_{m2n2}(\Omega) = \sum_{jmn} (-1)^{m1-n1} (2j+1) \begin{pmatrix} j1 & j2 & j \\ -m1 & m2 & m \end{pmatrix} D^{(j)*}_{mn}(\Omega) \begin{pmatrix} j1 & j2 & j \\ -n1 & n2 & n \end{pmatrix}. \tag{2.47}$$

The uniaxial symmetry of $f(\Omega)$ presupposed here requires

$$\left\langle D^{(k)}_{mm'}(\Omega) \right\rangle = \int d\Omega D^{(k)}_{mm'}(\Omega) f(\Omega) = 0 \tag{2.48}$$

when m and $m' \neq 0$. Accordingly, the only following terms are calculated:

$$\left\langle D^{(2)*}_{00}(\Omega)\, D^{(2)}_{00}(\Omega) \right\rangle = \frac{1}{5} + \frac{2}{7}\left\langle D^{(2)}_{00}(\Omega) \right\rangle + \frac{18}{35}\left\langle D^{(4)}_{00}(\Omega) \right\rangle, \tag{2.49}$$

$$\begin{aligned} \left\langle D^{(2)*}_{01}(\Omega)\, D^{(2)}_{01}(\Omega) \right\rangle &= \frac{1}{5} + \frac{1}{7}\left\langle D^{(2)}_{00}(\Omega) \right\rangle - \frac{12}{35}\left\langle D^{(4)}_{00}(\Omega) \right\rangle \\ &= \left\langle D^{(2)*}_{0-1}(\Omega)\, D^{(2)}_{0-1}(\Omega) \right\rangle, \end{aligned} \tag{2.50}$$

and

$$\begin{aligned} \left\langle D^{(2)*}_{02}(\Omega)\, D^{(2)}_{02}(\Omega) \right\rangle &= \frac{1}{5} - \frac{2}{7}\left\langle D^{(2)}_{00}(\Omega) \right\rangle + \frac{3}{35}\left\langle D^{(4)}_{00}(\Omega) \right\rangle \\ &= \left\langle D^{(2)*}_{0-2}(\Omega)\, D^{(2)}_{0-2}(\Omega) \right\rangle. \end{aligned} \tag{2.51}$$

Thus, the polarized Raman intensity at Y is given by

$$I_{(Y)}(\omega,\omega) = C_1(\omega) + C_2(\omega)\left\langle D^{(2)}_{00}(\Omega) \right\rangle + C_3(\omega)\left\langle D^{(4)}_{00}(\Omega) \right\rangle + C_4(\omega) R_{(Y)}. \tag{2.52}$$

The coefficients $C_1(\omega)$ to $C_4(\omega)$ and $R_{(Y)}$ are given by the following equations:

$$\begin{aligned}
C_1(\omega) = & \\
& a^2 T_x^2 T_x'^2 + \frac{4}{45} b^2 T_x^2 T_x'^2 \\
& + \left[-2a^2 T_x^2 T_x'^2 + \frac{b^2}{45} \left(-8 T_x^2 T_x'^2 + 3 T_z^2 T_x'^2 + 3 T_x^2 T_z'^2 \right) \right] \cos^2 \omega \\
& + \left[a^2 \left(T_x^2 T_x'^2 + T_z^2 T_z'^2 \right) \right. \\
& \left. + \frac{b^2}{45} \left(4 T_x^2 T_x'^2 - 3 T_z^2 T_x'^2 - 3 T_x^2 T_z'^2 + 4 T_z^2 T_z'^2 \right) \right] \cos^4 \omega,
\end{aligned} \tag{2.53}$$

$$\begin{aligned}
C_2(\omega) = & \\
& - \frac{2}{3} ab T_x^2 T_x'^2 - \frac{4}{63} b^2 T_x^2 T_x'^2 \\
& + \left[\frac{4}{3} ab T_x^2 T_x'^2 + \frac{b^2}{63} \left(8 T_x^2 T_x'^2 + 3 T_z^2 T_x'^2 + 3 T_x^2 T_z'^2 \right) \right] \cos^2 \omega \\
& + \left[\frac{b^2}{63} \left(-4 T_x^2 T_x'^2 - 3 T_z^2 T_x'^2 - 3 T_x^2 T_z'^2 + 8 T_z^2 T_z'^2 \right) \right. \\
& \left. + \frac{ab}{3} \left(-2 T_x^2 T_x'^2 + 4 T_z^2 T_z'^2 \right) \right] \cos^4 \omega,
\end{aligned} \tag{2.54}$$

$$\begin{aligned}
C_3(\omega) = & \\
& \frac{3}{35} b^2 T_x^2 T_x'^2 + \frac{b^2}{35} \left(-6 T_x^2 T_x'^2 - 4 T_z^2 T_x'^2 - 4 T_x^2 T_z'^2 \right) \cos^2 \omega \\
& + \frac{b^2}{35} \left(3 T_x^2 T_x'^2 + 4 T_z^2 T_x'^2 + 4 T_x^2 T_z'^2 + 8 T_z^2 T_z'^2 \right) \cos^4 \omega,
\end{aligned} \tag{2.55}$$

$$C_4(\omega) = T_x T_x' T_z T_z' \cos^2 \omega - T_x T_x' T_z T_z' \cos^4 \omega, \tag{2.56}$$

and

$$\begin{aligned}
R_{(Y)} = & \, c_1 \left[a^2 - \frac{2}{45} b^2 + \left(\frac{ab}{3} - \frac{4b^2}{63} \right) \left\langle D_{00}^{(2)}(\Omega) \right\rangle - \frac{4b^2}{35} \left\langle D_{00}^{(4)}(\Omega) \right\rangle \right] \\
& + c_2 b^2 \left(\frac{1}{15} + \frac{1}{21} \left\langle D_{00}^{(2)}(\Omega) \right\rangle - \frac{4}{35} \left\langle D_{00}^{(4)}(\Omega) \right\rangle \right),
\end{aligned} \tag{2.57}$$

where

$$c_1 = e^{i\delta X} e^{i\delta X'} + e^{-i\delta X} e^{-i\delta X'} \tag{2.58}$$

and

$$c_2 = e^{i\delta X} e^{-i\delta X'} + e^{-i\delta X} e^{i\delta X'}. \tag{2.59}$$

Consequently, the measured intensity is obtained by the integration of Eq. (2.52) from $Y = 0$ to d, where d is the sample thickness:

$$I(\omega,\omega) \equiv I_{\parallel}(\omega) = \int_0^d I_{(Y)}(\omega,\omega) \propto C_1(\omega) + C_2(\omega)\langle P_2(\cos\omega)\rangle + C_3(\omega)\langle P_4(\cos\omega)\rangle + C_4(\omega)R. \tag{2.60}$$

The birefringence affects only the parameter R, which is given by

$$\begin{aligned} R =& r_1\left[2a^2 - \frac{4}{45}b^2 + \left(\frac{2}{3}ab - \frac{8}{63}b^2\right)\langle P_2(\cos\beta)\rangle - \frac{8}{35}b^2\langle P_4(\cos\beta)\rangle\right] \\ &+ r_2 b^2\left[\frac{2}{15} + \frac{2}{21}\langle P_2(\cos\beta)\rangle - \frac{8}{35}\langle P_4(\cos\beta)\rangle\right]. \end{aligned} \tag{2.61}$$

Here r_1 and r_2 depend on the sample thickness d, birefringence Δn, incident laser light wavelength λ, and scattered light wavelength λ':

$$r_1 = \sin(K_1 d)/K_1 d \tag{2.62}$$

and

$$r_2 = \sin(K_2 d)/K_2 d, \tag{2.63}$$

with

$$K_1 = \frac{2\pi\Delta n(\lambda + \lambda')}{\lambda\lambda'} \tag{2.64}$$

and

$$K_2 = \frac{2\pi\Delta n(\lambda - \lambda')}{\lambda\lambda'}. \tag{2.65}$$

When $\omega = 0$ and $\pi/2$, C_4 becomes zero and the birefringence effect disappears.

For the case of $\omega' = \omega + \pi/2$, similar calculation gives

$$I_{(Y)}(\omega,\omega+\frac{\pi}{2}) = C_5(\omega) + C_6(\omega)\left\langle D_{00}^{(2)}(\Omega)\right\rangle + C_7(\omega)\left\langle D_{00}^{(4)}(\Omega)\right\rangle - C_4(\omega)R_{(Y)}. \tag{2.66}$$

The coefficients $C_5(\omega)$ to $C_7(\omega)$ are given by following equations:

$$\begin{aligned}
C_5(\omega) = & \\
& \frac{b^2 T_x^2 T_z'^2}{15} + \left[a^2 \left(T_x^2 T_x'^2 + T_z^2 T_z'^2\right)\right. \\
& \quad \left. + \frac{b^2}{45}\left(4T_x^2 T_x'^2 - 6T_x^2 T_z'^2 + 4T_z^2 T_z'^2\right)\right] \cos^2\omega \\
& + \left[a^2 \left(-T_x^2 T_x'^2 - T_z^2 T_z'^2\right)\right. \\
& \quad \left. + \frac{b^2}{45}\left(-4T_x^2 T_x'^2 + 3T_z^2 T_x'^2 + 3T_x^2 T_z'^2 - 4T_z^2 T_z'^2\right)\right] \cos^4\omega, \qquad (2.67)
\end{aligned}$$

$$\begin{aligned}
C_6(\omega) = & \\
& \frac{b^2 T_x^2 T_z'^2}{21} + \left[\frac{ab}{3}\left(-2T_x^2 T_x'^2 + 4T_z^2 T_z'^2\right)\right. \\
& \quad \left. + \frac{b^2}{63}\left(-4T_x^2 T_x'^2 - 6T_x^2 T_z'^2 + 8T_z^2 T_z'^2\right)\right] \cos^2\omega \\
& + \left[\frac{ab}{3}\left(2T_x^2 T_x'^2 - 4T_z^2 T_z'^2\right)\right. \\
& \quad \left. + \frac{b^2}{63}\left(4T_x^2 T_x'^2 + 3T_z^2 T_x'^2 + 3T_x^2 T_z'^2 - 8T_z^2 T_z'^2\right)\right] \cos^4\omega, \qquad (2.68)
\end{aligned}$$

and

$$\begin{aligned}
C_7(\omega) = & \\
& -\frac{4}{35} b^2 T_x^2 T_z'^2 + \frac{b^2}{63}\left(3T_x^2 T_x'^2 + 8T_x^2 T_z'^2 + 8T_z^2 T_z'^2\right)\cos^2\omega \\
& + \frac{b^2}{35}\left(-3T_x^2 T_x'^2 - 4T_z^2 T_x'^2 - 4T_x^2 T_z'^2 - 8T_z^2 T_z'^2\right)\cos^4\omega. \qquad (2.69)
\end{aligned}$$

Thus, the measured intensity is described by

$$\begin{aligned}
I(\omega, \omega + \frac{\pi}{2}) & \equiv I_\perp(\omega) \\
& \propto C_5(\omega) + C_6(\omega)\left\langle P_2(\cos\omega)\right\rangle + C_7(\omega)\left\langle P_4(\cos\omega)\right\rangle - C_4(\omega) R. \qquad (2.70)
\end{aligned}$$

Since the scattered light is collected by an objective lens, the polarized Raman intensity is affected by the effect of a refracting angle when the scattered light passes by the interface between the liquid crystal material and the substrate [58–61]. Hence this effect must be corrected by

$$I_{\parallel,\mathrm{meas}}(\omega) = \frac{I_\parallel(\omega)}{n_{Z_{\mathrm{meas}}}(\omega)^2} \qquad (2.71)$$

and

$$I_{\perp,\mathrm{meas}}(\omega) = \frac{I_{\perp}(\omega)}{n_{X_{\mathrm{meas}}}(\omega)^2}, \tag{2.72}$$

where

$$n_{Z_{\mathrm{meas}}}(\omega) = \frac{n_Z n_X}{\sqrt{n_Z^2 \sin^2\omega + n_X^2 \cos^2\omega}} \tag{2.73}$$

and

$$n_{X_{\mathrm{meas}}}(\omega) = \frac{n_Z n_X}{\sqrt{n_Z^2 \cos^2\omega + n_X^2 \sin^2\omega}}. \tag{2.74}$$

In the isotropic phase, both $\langle P_2(\cos\beta)\rangle$ and $\langle P_4(\cos\beta)\rangle$ become zero and the polarized Raman intensities do not depend on ω, therefore, the depolarization ratio is given by

$$R_{\mathrm{iso}} = \frac{I_{\perp}}{I_{\parallel}} = \frac{3b^2}{45a^2 + 4b^2}. \tag{2.75}$$

This relation gives a/b from the depolarization ratio in the isotropic phase.

The fitting procedure with Eqs (2.60) and (2.70) gives the orientational order parameters from the measured polarized Raman intensities depending on ω, where the fitting parameters are $\langle P_2(\cos\beta)\rangle$, $\langle P_4(\cos\beta)\rangle$, a/b, and R.

2.2 Demonstration in a nematic liquid crystal system

The advantage of the analysis using Eq. (2.60) and (2.70) is demonstrated in this section. A usual experimental setup for the polarized Raman scattering measurement is drawn in Fig. 2.2. The green light at 514.5 nm wavelength from an Ar ion laser (Spectra-Physics, BeamLok 2060) is used for the excitation light source. The cell is mounted in a temperature-controlled oven ($\pm$0.1 K). The backscattered light is collected by a telescope lens (f = 130 mm and f/d = 1.3) and focused on an optical fiber that transmits the light to a monochromator (Spex, 270M) combined with a multichannel detector (Princeton Instruments, IPDA 512). When the time-resolved measurement is performed for the observation of the molecular reorientation during the electro-optic response, the transmitted light passing through the sample cell is detected by a photodiode, so that the Raman scattering measurement can be synchronized with the electro-optic response.

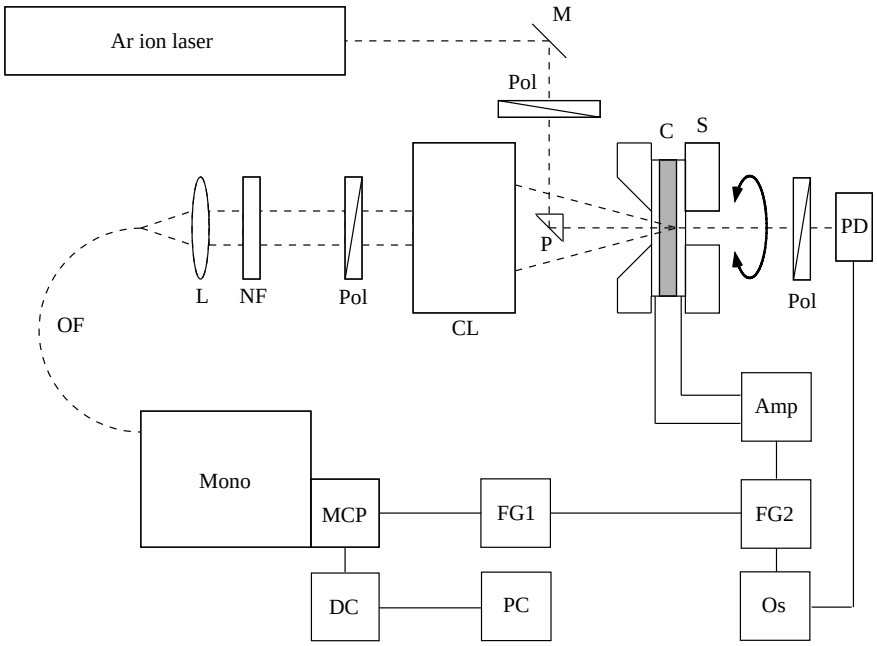

Figure 2.2: Schematic drawing of a experimental setup for polarized Raman scattering measurement. M, mirror; Pol, polarizer; P, prism; C, sample cell; S, rotating stage; PD, photodiode; CL, Cassegrain lens; NF, Raman notch filter; L, camera lens; OF, optical fiber; Mono, monochromator; MCP, multichannel photodiode array; DC, detector controller; PC, personal computer; FG1, function generator for the gate pulse; FG2, function generator for applying the electric field to the sample; Amp, high-speed amplifier; Os, oscilloscope. The broken lines represent light streams and the solid lines represent electric signals.

The experimental results obtained for a nematic liquid crystal, trans-4-pentyl-(4-cyanophenyl)-cyclohexane (PCH-5), are shown in Fig. 2.3. Figure 2.3(A) shows the polarized Raman spectra in isotropic phase. Two Raman lines appear in the measured region, one at 2220 cm^{-1} is assigned to the CN stretching mode (CN line) and the other is assigned to the phenyl stretching mode (phenyl line). The longest principal axes of their Raman tensors are almost parallel to the molecular long axis. They are well separated with each other and from the other lines, therefore, they suit the probe for investigating the molecular orientational order. The depolarization ratios for the phenyl line and the CN line in the isotropic phase are 0.496 and 0.259, respectively.

Figures 2.3(B-1) and 2.3(B-2) show the polarized Raman intensity variations plotted for the angle between the polarization direction of the incident laser light and the $\boldsymbol{n}$-director, ω. The liquid crystal molecules are homogeneously aligned in the sample cell with 50 μm thickness. $\omega = 0$ represents that the polarization direction of the incident light is parallel to the $\boldsymbol{n}$-director. $I_{\parallel,\mathrm{meas}}(\omega)$ shows the maximum at $\omega = 0°$ and 180° while the minimum at 90°. The maximum intensities are about ten times larger than the minimum intensity. On the other hand, $I_{\perp,\mathrm{meas}}(\omega)$ shows the maximum at $\omega = 45$ and 135° while the minimum at 0, 90, and 180°. The maximum intensities are two or more times larger than the minimum intensities. In this experiment, the measuring points are 19 for both $I_{\parallel,\mathrm{meas}}(\omega)$ and $I_{\perp,\mathrm{meas}}(\omega)$, and the signal to noise ratio is as three times improved as the case measuring only at the $\omega = 0$ and 90°. Furthermore, there is an additional advantage of which the fitting calculation can use the larger values than those at $\omega = 90°$ in $I_{\parallel,\mathrm{meas}}(\omega)$ and $\omega = 0$ and 90° in $I_{\perp,\mathrm{meas}}(\omega)$.

The fitting procedure using Eqs. (2.60) and (2.70) gives the orientational order parameters with high precision; $\langle P_2(\cos\beta)\rangle = 0.56 \pm 0.01$ and $\langle P_4(\cos\beta)\rangle = 0.17 \pm 0.01$ for the phenyl line, and $\langle P_2(\cos\beta)\rangle = 0.54 \pm 0.01$ and $\langle P_4(\cos\beta)\rangle = 0.16 \pm 0.02$ for the CN line. Here, $n_Z = 1.58$, $n_X = 1.48$, and $n_g = 1.46$ are used for the refractive indices. The same orientational order parameters are obtained from the different Raman lines assigned to the vibrational mode of the different parts of the molecule. This result is very natural with considering of the rigid core body in the molecule.

As seen in this example, the precision in the determination of the orientational order parameter from the polarized Raman scattering can be significantly improved

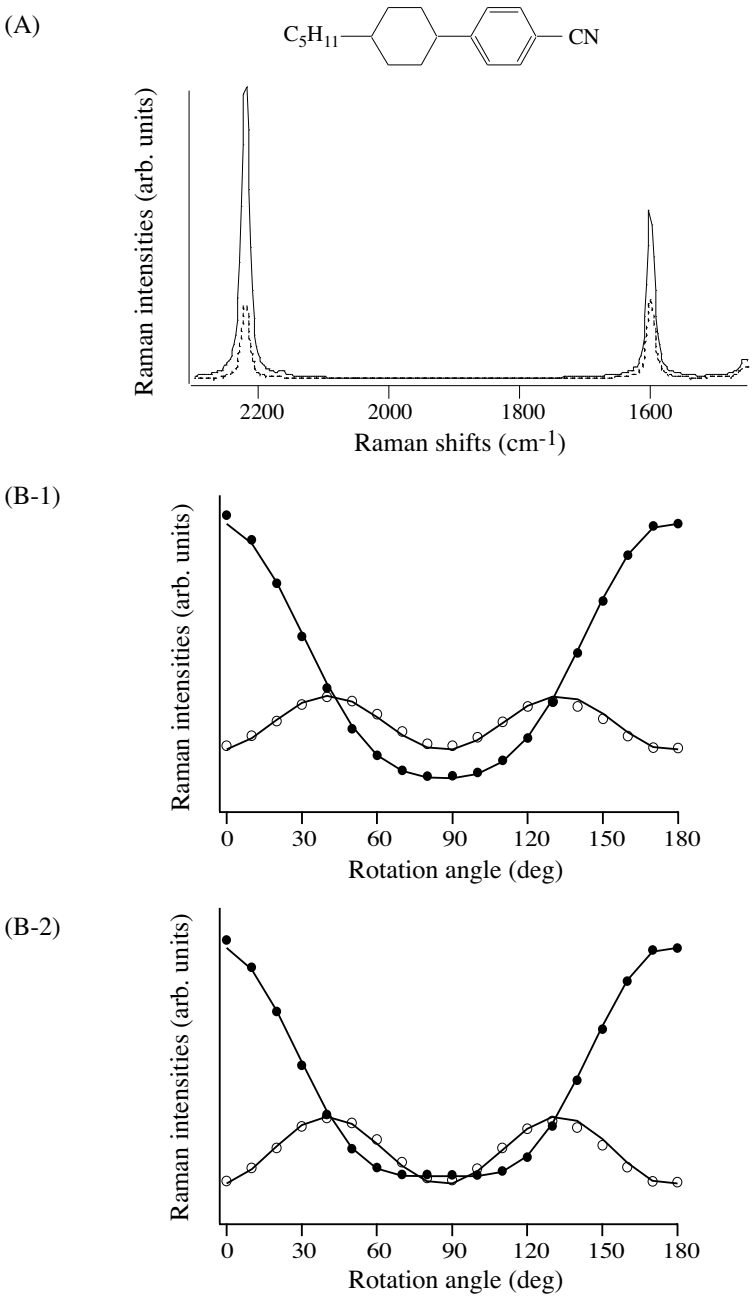

Figure 2.3: (A) Polarized Raman spectra in isotropic phase of PCH-5. The solid line and broken line show $I_{\parallel}$ and $I_{\perp}$, respectively. (B) Polarized Raman intensities are plotted for the angle between the polarization direction of the incident laser light and the $\boldsymbol{n}$-director, ω; the phenyl line at 1600 cm^{-1} (B-1), and the CN line at 2220 cm-1 (B-2). The solid circles and open circles show $I_{\parallel,\mathrm{meas}}(\omega)$ and $I_{\perp,\mathrm{meas}}(\omega)$, respectively. The lines show the best fitting results by Eq. (2.60) and (2.70).

so that this method is very effective for some subtle problems such as a time-resolved measurement for the investigation of the molecular reorientation induced by an external field.

Chapter 3

Investigations of Orientational Order for an Antiferroelectric Liquid Crystal

[Published in Physical Review E **63**, 02176 (2001)]

3.1 Introduction

Since Chandani *et al.* had discovered an antiferroelectric liquid crystal phase in MHPOBC [25,26], the mechanisms of the successive phase transitions and the appearances of the subphases have been investigated by various methods with interests in science as well as in applications. The phase sequence and the transition temperatures of the optically pure MHPOBC are as below: isotropic – 148°C – smectic-A (SmA) – 122°C – smectic-C_α* (SmC_α*) – 120.9°C – smectic-C* (SmC*) – 119.2°C – smectic-C_γ* (SmC_γ*) – 118.4°C – smectic-C_A* (SmC_A*) – 65°C – crystal [27, 62]. The phase structures are described in Chapter 1. The appearance of the SmC* and its variant phases are closely related with intermolecular interaction in adjacent layers [4, 63–67].

In this chapter, the dependence of orientational order parameters on the phases is investigated by the polarized Raman scattering measurements for the thick homogeneous alignment cell (25 μm thick) of MHPOBC. The molecular orientational ordering must be biaxial in the SmC* and its variant phases because the anisotropic molecular

interaction in the adjacent layers hinders the molecular free rotation around its long axis. It was observed under an electric field by infrared (IR) absorbance measurements that the the rotation of the C=O group around the molecular long axis was hindered and the biased direction was different in the SmC^* and the SmC_A^* phase [21, 68, 69]. However, any spectroscopic observation of the biaxiality without any external field has not been reported so far. The polarized Raman scattering measurement is applied to the observation of the molecular orientational ordering in the SmA, SmC^* and its variant phases of MHPOBC.

Experimentally some optical phenomena disturb the data analysis of the Raman scattering measurement, for example, the effects of the birefringence of the ordered liquid crystal as described in the preceding chapter. There are plenty of reports on the measurement of the order parameters in the nematic and SmA phases so far [10,13–17]. The order parameters of MHPOBC have been already reported in SmA phase [14]. However, the analysis of the phases other than the uniaxial nematic and SmA phases becomes more complicated. In phases other than uniaxial ones, the Raman intensities depend on the way smectic layers are piled up. Under the proper correction of the optical disturbance originated from the smectic layer structure, however, the orientational order parameters $\langle P_2(\cos\beta)\rangle$ and $\langle P_4(\cos\beta)\rangle$ can be defined as long as liquid crystal molecules uniaxially distribute within a layer. In this chapter the correction for the analysis in SmC^* and its variant phases of MHPOBC will be derived, which take account of the peculiar optical disturbance by the following origins; i.e., the tilt angle of the molecular axis with the smectic layer normal, the spiral structure, and the layer tilt angle from the substrate surface normal due to the chevron layer structures [4–9].

3.2 Theoretical treatments

3.2.1 Definition of the reference coordinate systems

The molecular orientational order parameter is obtained by the analysis of the polarized Raman intensity [10,11]. The backscattering configuration for the homogeneously aligned sandwich cell is assumed here [cf. Figs. 1.4(B) and 2.1]. It is necessary to define

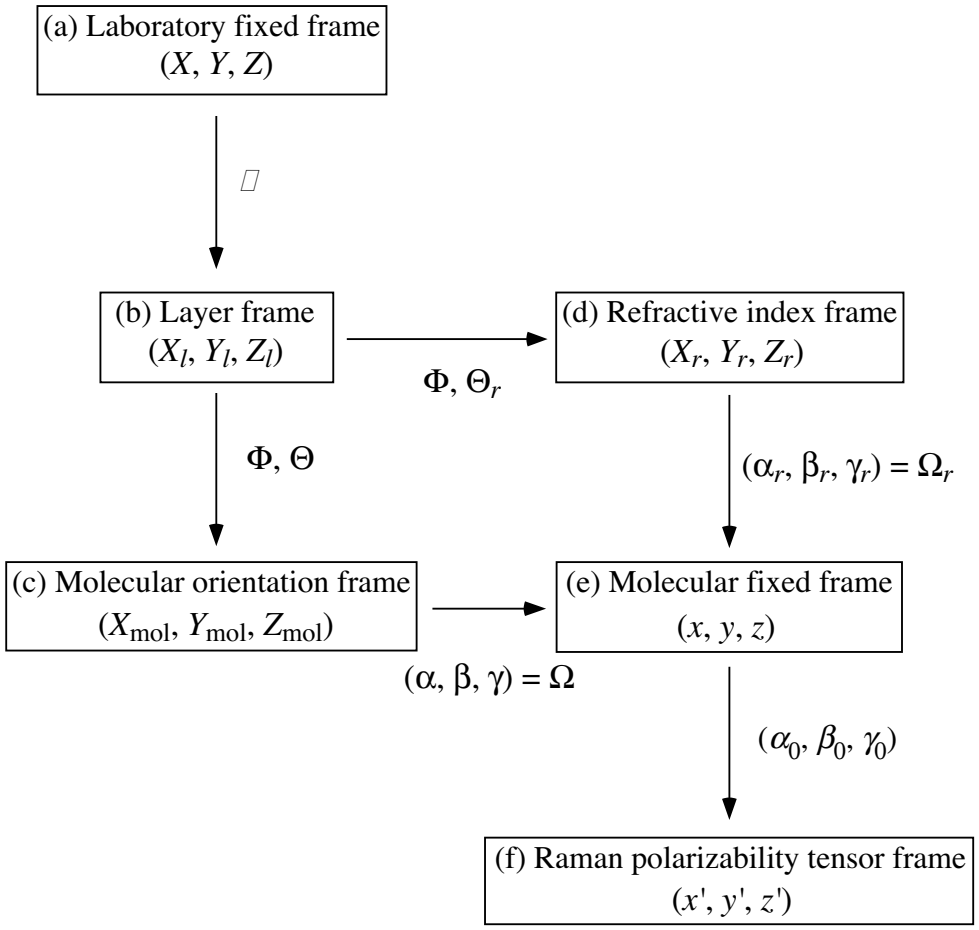

Figure 3.1: Schematic diagram of coordinate system. The details are described in theoretical treatment section.

the orientational relation between the individual molecules and a reference coordinate system for the description of the molecular orientational distribution. Raman polarizability tensors of the individual molecules were described in the reference coordinate system by using several Cartesian coordinate systems that are based on the smectic layer structure, and the transformations among the coordinate systems are explained here. A schematic diagram and the drawings of the coordinate systems are given in Figs. 3.1 and 3.2, respectively. The coordinate systems are defined according to Fig. 3.1(a)–3.1(f). (a) A laboratory fixed coordinate frame is the reference coordinate system that is defined by X, Y, and Z with respect to the sample cell, here [Fig. 3.2(a)], the XZ plane is parallel to the glass substrate of the cell. The incident laser beam comes into the cell and the scattered light goes back along the Y axis. Here, the

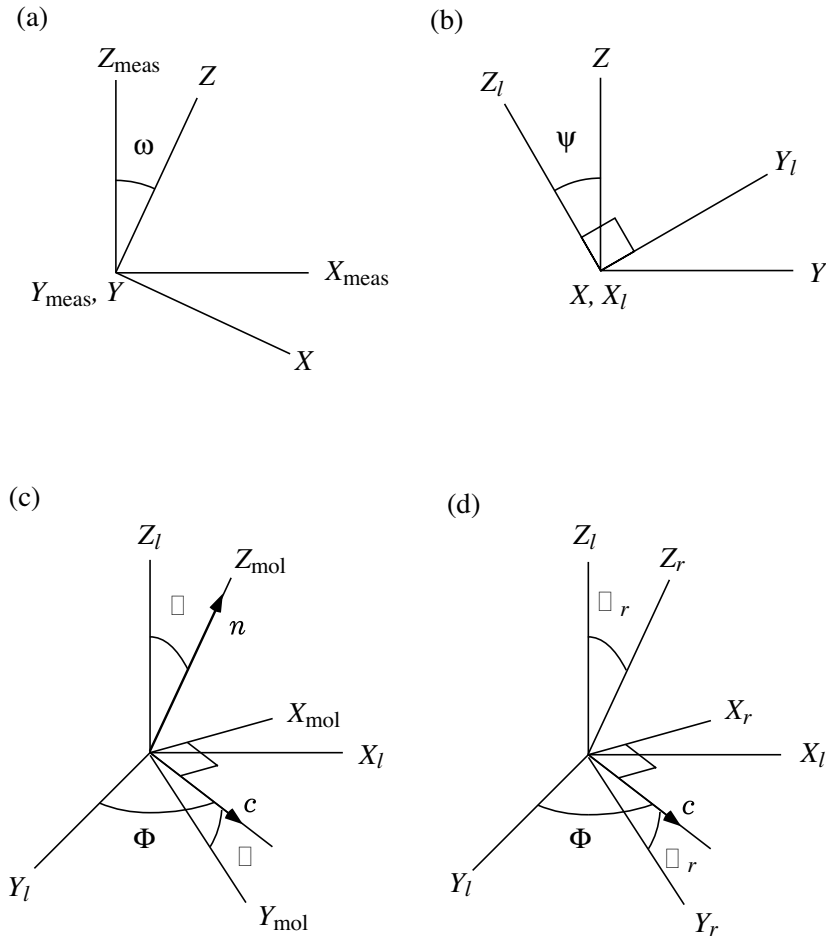

Figure 3.2: The defined coordinate systems. (a) The laboratory fixed frame and the measurement coordinate frame. (b) The laboratory fixed frame and the layer fixed frame. (c) The layer frame and the molecular orientation frame. (d) The layer frame and the refractive index frame.

incident laser light is polarized parallel to the $Z_{\rm meas}$ axis as defined in the preceding chapter. (b) A layer frame is defined by X_l, Y_l, and Z_l on the layer of smectic phase [Fig. 3.2(b)]. The Z_l axis is parallel to the layer normal and tilts from the Z axis by the angle $+\Psi$ or $-\Psi$ because the layer is inclined from the glass plates due to the chevron layer structure. The X_l axis is parallel to the X axis. (c) A molecular orientation frame is defined by $X_{\rm mol}$, $Y_{\rm mol}$, and $Z_{\rm mol}$ for one smectic layer [Fig. 3.2(c)]. The $Z_{\rm mol}$ axis is the center of the molecular orientational distribution in this layer, that is, the $Z_{\rm mol}$ axis is parallel to the $\boldsymbol{n}$-director defined within the layer. The rotational transformation from the layer frame to the molecular orientation frame is described by the angles of Φ and Θ. Φ is the angle between the $\boldsymbol{c}$-director and the X_l axis. The Θ is the angle between the $Z_{\rm mol}$ and the Z_l axes. In SmA phase, $\Phi = 0$ and the molecular orientation frame coincides with the layer frame. (d) A refractive index frame is defined by X_r, Y_r, and Z_r [Fig. 3.2(d)]. These axes are identical with the optic elasticity axes and refractive indices are defined in this frame. The refractive index frame is not the same as the molecular orientation frame in the phase with helical structure, if the helical pitch is longer than a wavelength of light, because the optical property is given by an average over helically twisted layers with the wavelength of light. However, at the center of these layers, the averaged optical plane defined as a plane containing two optic axes is parallel to the $Y_{\rm mol}Z_{\rm mol}$ plane of the molecular orientation frame in SmC*, SmC_γ* and SmC_A* phase of MHPOBC system [31]. Therefore, the transformation from layer frame to the refractive index frame is defined by Ψ and Θ_r as the analog of molecular orientation frame. (e) A molecular fixed frame is defined by x, y and z on the individual molecules. The z axis is defined to be parallel to the molecular long axis. α, β, and γ are defined as the Euler angles that transform the molecular orientation frame to the molecular fixed frame. (f) A Raman tensor frame is defined by x', y' and z'. In this frame the Raman tensor of a vibrational mode for a particular molecule is diagonalized and has the form of

$$\begin{pmatrix} \alpha_{x'x'} & & \\ & \alpha_{y'y'} & \\ & & \alpha_{z'z'} \end{pmatrix}.$$

α_{MM} ($M = x', y', z'$) is a MM component of the Raman tensor in this frame and $\alpha_{z'z'}$ is the largest. The z' axis is not parallel to the z axis generally. The Euler angles (α_0, β_0, γ_0) transform the molecular fixed frame to the Raman tensor frame.

Now it is assumed that the polarization vectors of the incident light and the scattered light are within the XZ plane and make the angles ω and ω' with Z axis, respectively [Fig. 3.2(a)]. $\boldsymbol{E}_{(Y)}$ and $\boldsymbol{E'}_{(Y)}$ are defined as the electric fields of incident light and scattered light at the depth Y from the surface of the liquid crystal, and they can be decomposed into X_r, Y_r, and Z_r components of the refractive index frame,

$$\boldsymbol{E}_{(\mathrm{Y})} = E_{X_r} e^{-i\delta X_r} \hat{X}_r + E_{Y_r} e^{-i\delta Y_r} \hat{X}_r + E_{Z_r} \hat{Z}_r \tag{3.1}$$

and

$$\boldsymbol{E'}_{(\mathrm{Y})} = E'_{X_r} e^{-i\delta' X_r} \hat{X}_r + E'_{Y_r} e^{-i\delta' Y_r} \hat{Y}_r + E'_{Z_r} \hat{Z}_r, \tag{3.2}$$

where the phase factors of $e^{-i\delta X_r}$, $e^{-i\delta Y_r}$, $e^{-i\delta' X_r}$, and $e^{-i\delta' Y_r}$ are introduced to give the correction for the retardation effect that is due to the birefringence of the ordered liquid crystal. δX_r, δY_r, $\delta' X_r$, and $\delta' Y_r$ are the phase difference of the X_r and Y_r components with the Z_r component.

3.2.2 Smectic phase structure and electric fields of lights

The peculiar structure of each smectic phase should be reflected on the further effective optical correction for the electric fields of the incident laser light and the scattered light. The effective corrections for each smectic phase are summarized below. For example, SmC^* and the other variant phases exhibit helical structure and optical biaxiality; then one should give a close examination for the proper correction. The relation between the molecular orientation frame and the refractive index frame is also described.

SmA phase

SmA phase is optically uniaxial and $\Theta = 0$, so that the refractive index frame, the molecular orientation frame and the layer frame are identical with each other. When a layer tilt for the substrates Ψ is taken into account [4, 70], the electric fields of the

incident and the scattered lights are given by

$$\begin{aligned}\boldsymbol{E}_{(Y)} &= e^{-i\delta X_r}\left(T_X \sin\omega\right)\hat{X}_r + e^{-i\delta Y_r}\left(T_Z \sin\Psi\cos\omega\right)\hat{Y}_r \\ &\quad + \left(T_Z \cos\Psi\cos\omega\right)\hat{Z}_r, \qquad (3.3)\\ \boldsymbol{E'}_{(Y)} &= e^{-i\delta' X_r}\left(T'_X \sin\omega'\right)\hat{X}_r + e^{-i\delta' Y_r}\left(T'_Z \sin\Psi\cos\omega'\right)\hat{Y}_r \\ &\quad + \left(T'_Z \cos\Psi\cos\omega'\right)\hat{Z}_r. \qquad (3.4)\end{aligned}$$

T_M and T'_M are transmission coefficients for M components of electric field at the interface between substrate and liquid crystal. They are calculated by

$$T_M = \frac{2n_g}{n_g + n_M}, \quad T'_M = \frac{2n_M}{n_g + n_M}. \qquad (3.5)$$

n_g is the refractive index of glass substrate and n_M are the principal refractive indices of the liquid crystal when the light is polarized to M axis. These values are calculated as

$$n_Z = \frac{n_\perp n_\parallel}{\sqrt{n_\perp^2 \cos^2\Psi + n_\parallel^2 \sin^2\Psi}}, \quad n_X = n_\perp, \qquad (3.6)$$

where $n_\parallel$ and $n_\perp$ are the principal refractive indices of liquid crystal.

SmC_α* phase

In SmC_α* phase, the helical pitch is smaller than wavelengths of the incident and scattered light [71]. Then the phase is optically uniaxial and the refractive index frame is identical with the layer frame. The electric field of light is given by Eqs. (3.3) and (3.4) as for the SmA phase.

SmC* phase

SmC* phase is optically biaxial [31] and has a helical structure. In this phase, the helical pitch H is larger than the wavelength of the light [28, 72], so that the optical elasticity axes or the refractive index frame axes are not identical with the molecular orientation frame axes. Optic elasticity axes at Φ would be given by the average of the molecular orientation frame between $\Phi - \pi\lambda/H$ and $\Phi + \pi\lambda/H$, because the spatial resolution could be determined by the wavelength of the light λ. Hence $\hat{Z}_r$ is described

in the layer frame as

$$\hat{Z}_r = Z_r \begin{pmatrix} \sin\Theta\langle\langle\sin\Phi'\rangle\rangle \\ \sin\Theta\langle\langle\cos\Phi'\rangle\rangle \\ \cos\Theta \end{pmatrix}, \tag{3.7}$$

where $\langle\langle\cdots\rangle\rangle$ denotes statistical average from $\Phi' = \Phi - \pi\lambda/H$ to $\Phi' = \Phi + \pi\lambda/H$. $\langle\langle\cos\Phi'\rangle\rangle$ and $\langle\langle\sin\Phi'\rangle\rangle$ are calculated as

$$\langle\langle\cos\Phi'\rangle\rangle = \int_{\Phi-\pi\lambda/H}^{\Phi+\pi\lambda/H} \cos\Phi' d\Phi' \Big/ \int_{\Phi-\pi\lambda/H}^{\Phi+\pi\lambda/H} d\Phi = \frac{H}{\pi\lambda}\sin\left(\frac{\pi\lambda}{H}\right)\cos\Phi, \tag{3.8}$$

$$\langle\langle\sin\Phi'\rangle\rangle = \int_{\Phi-\pi\lambda/H}^{\Phi+\pi\lambda/H} \sin\Phi' d\Phi' \Big/ \int_{\Phi-\pi\lambda/H}^{\Phi+\pi\lambda/H} d\Phi = \frac{H}{\pi\lambda}\sin\left(\frac{\pi\lambda}{H}\right)\sin\Phi, \tag{3.9}$$

so that

$$\hat{Z}_r = Z_r \times \begin{pmatrix} \frac{H}{\pi\lambda}\sin\left(\frac{\pi\lambda}{H}\right)\sin\Theta\sin\Phi \\ \frac{H}{\pi\lambda}\sin\left(\frac{\pi\lambda}{H}\right)\sin\Theta\cos\Phi \\ \cos\Theta \end{pmatrix}. \tag{3.10}$$

In the same way as $\hat{Z}_r$,

$$\hat{X}_r = X_r \times \begin{pmatrix} \frac{H}{\pi\lambda}\sin\left(\frac{\pi\lambda}{H}\right)\cos\Theta\cos\Phi \\ \frac{H}{\pi\lambda}\sin\left(\frac{\pi\lambda}{H}\right)\cos\Theta\sin\Phi \\ \cos\Theta \end{pmatrix}, \tag{3.11}$$

$$\hat{Y_r} = Y_r \times \begin{pmatrix} \frac{H}{\pi\lambda}\sin\left(\frac{\pi\lambda}{H}\right)\cos\Theta\cos\Phi \\ \frac{H}{\pi\lambda}\sin\left(\frac{\pi\lambda}{H}\right)\cos\Theta\sin\Phi \\ \cos\Theta \end{pmatrix}. \tag{3.12}$$

Consequently, $\boldsymbol{E}_{(\mathrm{X})}$ and $\boldsymbol{E'}_{(\mathrm{X})}$ are given by

$$\begin{aligned}
\boldsymbol{E}_{(\mathrm{Y})} &= e^{-i\delta X_r}\left(-T_Z K \sin\Phi \sin\Psi \cos\omega + T_X K \cos\Phi \sin\omega\right)\hat{X}_r \\
&+ e^{-i\delta Y_r}\left(-T_Z \sin\Theta \cos\Psi \cos\omega + T_Z K \cos\Phi \cos\Theta \sin\Psi \cos\omega\right. \\
&\quad \left. + T_X K \sin\Phi \cos\Theta \sin\omega\right)\hat{Y}_r \\
&+ \left(T_Z \cos\Theta \cos\Psi \cos\omega + T_Z K \cos\Phi \sin\Theta \sin\Psi \cos\omega\right. \\
&\quad \left. + T_X K \sin\Phi \sin\Theta \sin\omega\right)\hat{Z}_r, \qquad (3.13) \\
\boldsymbol{E'}_{(\mathrm{Y})} &= e^{-i\delta' X_r}\left(-T'_Z K' \sin\Phi \sin\Psi \cos\omega' + T'_Y K' \cos\Phi \sin\omega'\right)\hat{X}_r \\
&+ e^{-i\delta' Y_r}\left(-T'_Z \sin\Theta \cos\Psi \cos\omega' + T'_Z K' \cos\Phi \cos\Theta \sin\Psi \cos\omega'\right. \\
&\quad \left. + T'_Y K' \sin\Phi \cos\Theta \sin\omega'\right)\hat{Y}_r \\
&+ \left(T'_Z \cos\Theta \cos\Psi \cos\omega' + T'_Z K' \cos\Phi \sin\Theta \sin\Psi \cos\omega'\right. \\
&\quad \left. + T'_Y K' \sin\Phi \sin\Theta \sin\omega'\right)\hat{Z}_r, \qquad (3.14)
\end{aligned}$$

Where

$$K = \frac{H}{\pi\lambda}\sin\left(\frac{\pi\lambda}{H}\right), \quad K' = \frac{H}{\pi\lambda'}\sin\left(\frac{\pi\lambda'}{H}\right), \qquad (3.15)$$

and λ and λ' are the wavelengths of the incident and the scattered light in the medium, respectively.

Though T_M and T'_M depend on Φ in SmC^* phase, their variations are small enough to use Eqs. (3.5) and (3.6) approximately [31].

SmC_A* phase

In SmC_A* phase Θ is apparently zero at the spatial resolution of the light and the refractive index frame is identical with molecular orientation frame, because $\boldsymbol{c}$-director is reversed in the adjacent layer. In this phase, T_M and T'_M vary as in SmC^* phase. However, the variation of $n_\perp$ is very small in this phase also [31], so that T_M and T'_M can be calculated by Eqs. (3.5) and (3.6) approximately. Therefore the electric field of light is treated as in SmA phase. Hence the electric fields of the lights are given by Eqs. (3.3) and (3.4).

SmC_γ* phase

The average of the molecular tilt angle is apparently $\Theta/2$ at the spatial resolution of light, because $\boldsymbol{c}$-director is reversed once by the period of three layers in this phase [29, 31–33]. This phase is optically biaxial like the SmC* phase. Therefore the electric fields of lights are obtained by substituting $\Theta/2$ for Θ in the Eqs. (3.13) and (3.14). T_M and T'_M are approximated by Eqs. (3.5) and (3.6) also here.

3.2.3 Polarized Raman intensities

When the measured area is sufficiently large compared with the helical pitch, the Raman intensity is obtained by averaging for one period of the helical pitch,

$$I(\omega, \omega') \propto \int_0^{\pi} \sin\Theta d\Theta \int_0^{2\pi} d\Phi \int_0^{d} dY \langle \left|\alpha_{(Y)}(\omega, \omega')\right|^2 \rangle, \tag{3.16}$$

where $\alpha_{(Y)}(\omega, \omega')$ is the Raman polarizability tensor described in the molecular orientation frame, d is the sample thickness, and $\langle \left|\alpha_{(Y)}(\omega, \omega')\right|^2 \rangle$ is thes integrated value over the orientation of the liquid crystal,

$$\langle \left|\alpha_{(Y)}(\omega, \omega')\right|^2 \rangle = \int d\Omega \left|\alpha_{(Y)}(\omega, \omega')\right|^2 f(\Omega). \tag{3.17}$$

$f(\Omega)$ is the orientational distribution function of the molecular long axis or z axis with respect to the Z_{mol} axis and Ω denotes Euler angles (α, β, γ). Furthermore, the effect of a refracting angle on the Raman intensity must be taken into consideration and the measured intensity is obtained from

$$I_{\mathrm{meas}}(\omega, \omega') = \frac{I(\omega, \omega')}{n_{(\omega')^2}}, \tag{3.18}$$

where $n(\omega')$ is the refractive index at ω' given by

$$n(\omega') = \frac{n_Z n_X}{\sqrt{n_Z^2 \sin^2\omega' + n_X^2 \cos^2\omega'}}. \tag{3.19}$$

n_X and n_Z are the refractive indices of a liquid crystal material for the light polarized along the X axis and the Z axis, respectively. The combination of ω and ω' will be fixed at two configurations of $\omega' = \omega$ and $\omega' = \omega + \pi/2$. Here it was assumed that the ideal helical structure was formed in the chiral smectic phases, that is, the molecular orientational distribution was uniaxial with respect to the layer frame. With the

aid of the computer software Mathematica 2.2 (Wolfram Research, Inc.), Eqs. (3.16) and (3.18) are evaluated and rearranged. When the sample thickness is sufficiently large compared to the wavelengths of the incident and the scattered lights, the polarized Raman intensities are represented as a function of ω and the orientational order parameters;

$$\begin{aligned} I(\omega,\omega)_{\mathrm{meas}} &\equiv I_{\parallel}(\omega) \\ &= C_1(\cos\omega) + C_2(\cos\omega)\,\langle P_2(\cos\beta_{\mathrm{app}})\rangle \\ &\quad + C_3(\cos\omega)\,\langle P_4(\cos\beta_{\mathrm{app}})\rangle + C_4(\cos\omega)R, \qquad (3.20) \\ I(\omega,\omega+\pi/2)_{\mathrm{meas}} &\equiv I_{\perp}(\omega) \\ &= C_5(\cos\omega) + C_6(\cos\omega)\,\langle P_2(\cos\beta_{\mathrm{app}})\rangle \\ &\quad + C_7(\cos\omega)\,\langle P_4(\cos\beta_{\mathrm{app}})\rangle - C_4(\cos\omega)R. \qquad (3.21) \end{aligned}$$

$C_1(\cos\omega)$ to $C_7(\cos\omega)$ are the fourth-order functions of $\cos\omega$, whose coefficients depend on Θ and Ψ, the refractive index of the liquid crystal material and the glass substrate, helical pitch, and the Raman tensor. The coefficients for odd order terms of $C_1(\cos\omega)$ to $C_7(\cos\omega)$ are zero because of the symmetry of the system. R represents the component of retardation amplitude that depends on the sample thickness. $\langle P_2(\cos\beta_{\mathrm{app}})\rangle$ and $\langle P_4(\cos\beta_{\mathrm{app}})\rangle$ are the second- and the fourth-order orientational order parameters of the z' axis of Raman tensor with respect to the Z_l axis, and β_{app} is the angle between the z' axis and the Z_l axis. It should be noticed that the effect of the retardation on the Raman intensity is not zero even if $\omega = 0^\circ$ or $\omega = 90^\circ$ when the refractive index frame is inclined with respect to the incident light and the scattered light because of the helical structure. Therefore the orientational order parameters cannot be evaluated properly by the measurements of depolarization ratios only at $\omega = 0^\circ$ and $\omega = 90^\circ$, and at least three different measurement points of ω are needed.

It is supposed that the Raman tensor is uniaxial, namely, $\alpha_{x'x'} = \alpha_{y'y'} = \alpha_{\perp}$ and $\alpha_{z'z'} = \alpha_{\parallel}$ and the z' axis of the Raman tensor can rotate freely around the z axis of the molecular fixed frame. When the orientational molecular distribution defined in one layer has a cylindrical symmetry, $\langle P_2(\cos\beta_{\mathrm{app}})\rangle$ and $\langle P_4(\cos\beta_{\mathrm{app}})\rangle$ could be rewritten with the molecular orientational order parameters $\langle P_2(\cos\beta)\rangle$ and $\langle P_4(\cos\beta)\rangle$ with

respect to z axis in the molecular orientation frame as following equations:

$$\begin{aligned}\langle P_2(\cos\beta_{\rm app})\rangle &= \frac{1}{2}\left(3\cos^2\Theta-1\right)\frac{1}{2}\left(3\cos^2\beta_0-1\right)\langle P_2(\cos\beta)\rangle \\ &= \frac{1}{2}\left(3\cos^2\Theta-1\right)\langle P_2(\cos\beta')\rangle\,, \qquad (3.22)\\ \langle P_4(\cos\beta_{\rm app})\rangle &= \frac{1}{8}\left(35\cos^4\Theta-30\cos^2\Theta+3\right) \\ &\quad\times\frac{1}{8}\left(35\cos^4\beta_0-30\cos^2\beta_0+3\right)\langle P_4(\cos\beta)\rangle \\ &= \frac{1}{8}\left(35\cos^4\Theta-30\cos^2\Theta+3\right)\langle P_4(\cos\beta')\rangle\,, \qquad (3.23)\end{aligned}$$

where β_0 is the angle between z' axis and z axis, $\langle P_2(\cos\beta')\rangle$ and $\langle P_4(\cos\beta')\rangle$ are the orientational order parameters of the z' axis of the Raman tensor with respect to z axis. It should be noticed that apparent values of $\langle P_2(\cos\beta_{\rm app})\rangle$ and $\langle P_4(\cos\beta_{\rm app})\rangle$ would be reduced by Θ and β_0, and even become zero with the specific value of Θ and β_0 at the so called magic angle value.

In isotropic phase, both $\langle P_2(\cos\beta)\rangle$ and $\langle P_4(\cos\beta)\rangle$ are zero and the depolarization ratio $R_{\rm iso}$ is calculated as

$$R_{\rm iso} \equiv I_\perp/I_\parallel = 3b^2/\left(45a^2+4b^2\right), \qquad (3.24)$$

where a and b correspond to the average value and the anisotropy of the Raman tensor, respectively, and calculated by

$$a = \frac{1}{3}(\alpha_\parallel + 2\alpha_\perp) \qquad (3.25)$$

$$b = (\alpha_\parallel - \alpha_\perp) \qquad (3.26)$$

Thus the orientational order parameter is obtained from the analysis of $I_\parallel(\omega)$, $I_\perp(\omega)$, and $R_{\rm iso}$ using Eqs. (3.20)–(3.24) if the structural parameters are known. It should be noticed that only $\langle P_2(\cos\beta')\rangle$ and $\langle P_4(\cos\beta')\rangle$ are possible to be evaluated from these equations because β_0 is a unknown parameter, here.

3.3 Experiments

The molecular structure of (S)-MHPOBC is shown in Fig. 3.3. MHPOBC has three benzene rings and two ester bonds, one is in a center of the core part and another is

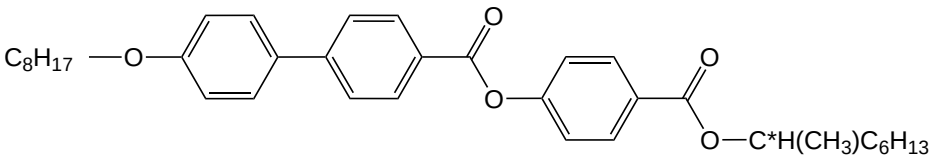

Figure 3.3: Chemical structure of MHPOBC.

attached to the end of the core part or the chiral part. In order to confirm the purity of the sample, the phase transition temperatures were measured by the differential scanning calorimeter of TA Instruments DSC 2920 [26, 27]. The experimental cell was prepared as follows and the homogeneous alignment was accomplished. The sample was sandwiched between two indium tin oxide-coated quartz plates with the thickness of 25 μm by using poly(ethylene terephthalate) spacers. The quartz plates were spin coated with polyimide and one of them was rubbed in one direction. The cell was set on the rotating stage, which was equipped with the heat controller that adjusted temperature with the accuracy of ± 0.1°C with a controller (Yokogawa, UP550). The condition of alignment was checked by a polarizing optical microscope. Many focal conics were observed except for SmA phase, but the whole image was sufficiently dark and it was assumed that they did not affect Raman intensities much. Hence, the disturbance of alignment by these defects was ignored [14].

The polarized Raman spectra were measured by the following system. The green light at 514.5 nm from an argon ion laser (Spectra-Physics, BeamLok 2060) was used for excitation. The exciting light was polarized by a glan laser prism. Scattered light was collected by a lens in the back light scattering configuration and introduced to a polarizer, a Raman notch filter and a monochromator (Spex, 270M) combined with a multichannel detector (Princeton Instruments, IPDA 512). The incident laser power was set at 0.5 W and the slit width of the monochromator was 50 μm in all measurements. The depolarization ratios of Raman lines were estimated by the measurement for isotropic phase at 150°C. The Raman lines were deconvoluted with Lorentzian function to obtain integrated intensities.

Polarized Raman spectra were measured at various polarization directions of the incident laser light, and the angle of the orientation between the polarization direction

of the laser light and liquid crystal alignment were set from 0° to 180° at steps of 10°. The temperature was varied from 90 to 140°C. In order to confirm the phase of the sample during the Raman scattering measurement, simultaneous monitoring of the capacitance of the cell was done by a LCR meter (YHP, 4262A), as shown in Fig. 3.5. The frequency of the test signal was 1 kHz. In the ferroelectric phase (SmC^*) the capacitance shows a peak value due to a spontaneous polarization, but in the antiferroelectric (SmC_A^*) and paraelectric phase (SmA), it drops down. In the ferrielectric phases (SmC_α^* and SmC_γ^*), it exhibits decreasing values [4, 32, 73].

The theoretical predictions of the Raman tensors were carried out by an *ab initio* restricted Hartree-Fock calculation with the 3-21G basis set using the Gaussian 94 package [74].

The refractive indices of liquid crystal for which the light is polarized parallel and perpendicular to the Z_l axis, $n_\parallel$, and $n_\perp$ were obtained from ref. [31]. The refractive index of quartz plates n_g was 1.46.

Helical pitches were measured by the diffraction method [75, 76] with He–Ne laser at 632.8 nm.

3.4 Results

Figure 3.4 shows the polarized Raman spectra in isotropic phase at 150°C. Three Raman lines were investigated, i.e., C-C stretching mode of three benzene rings at 1600 cm^{-1} , which is abbreviated as "phenyl,"C=O stretching mode of chiral carbonyl group at 1720 cm^{-1},"chiral CO,"and C=O stretching mode of core carbonyl group at 1740 cm^{-1}, "core CO" [14, 77]. Their depolarization ratios are listed in Table 3.1. The shifts of the Raman lines in crystal–SmI^* phase transition [77] have been reported, but any shift and change of line width were not observed in the successive phase transitions from isotropic to SmC_A^* phase. This shows that no major changes occur either in the normal coordinates or in the intermolecular interactions during these phase transitions.

The results of an *ab initio* calculation are listed in Table 3.1. The calculated depolarization ratios of three Raman lines in question generally agree with the observed values in isotropic phase. The Raman activities predicted by the *ab initio* calculations

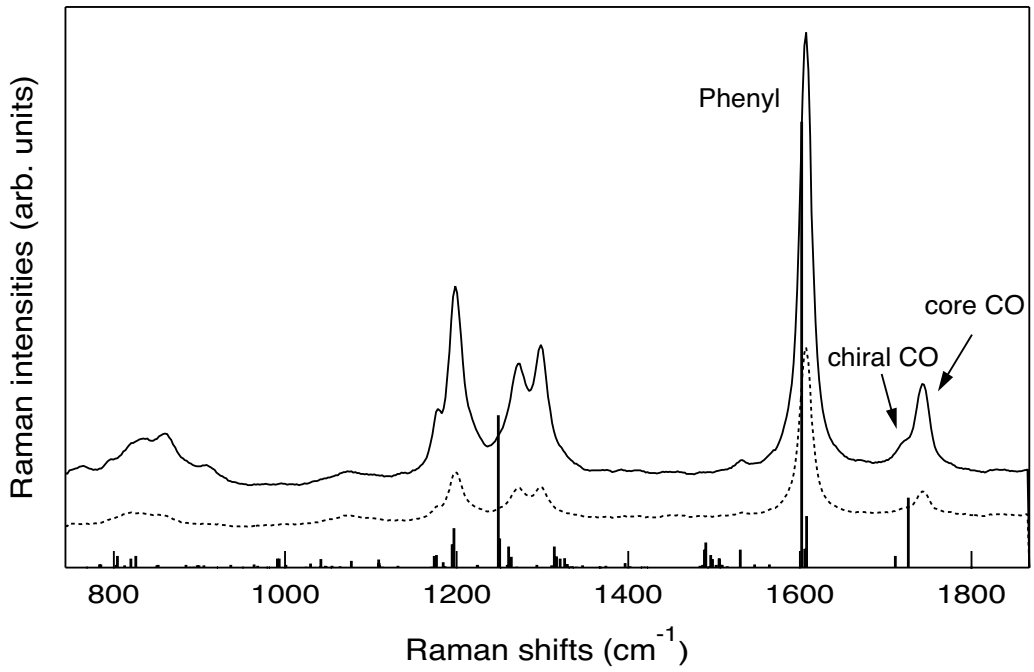

Figure 3.4: The polarized Raman spectrum in isotropic phase at 150°C (the solid line for $I_{\parallel}$; the broken line for $I_{\perp}$) and the Raman activities obtained from *ab initio* calculations (the sticks).

Table 3.1: *Ab initio* calculation results. α_{MM} $(M = x', y', z')$ is a MM component of the Raman tensor in Cartesian coordinate of Raman tensor frame.

	depolarization ratios		Raman tensors		
Raman lines	Obs.	Calc.	$\alpha_{x'x'}$	$\alpha_{y'y'}$	$\alpha_{z'z'}$
phenyl	0.382	0.389	0.13	0.50	10.6
chiral CO	0.221	0.298	0.01	0.10	1.75
core CO	0.263	0.280	0.01	0.45	4.25

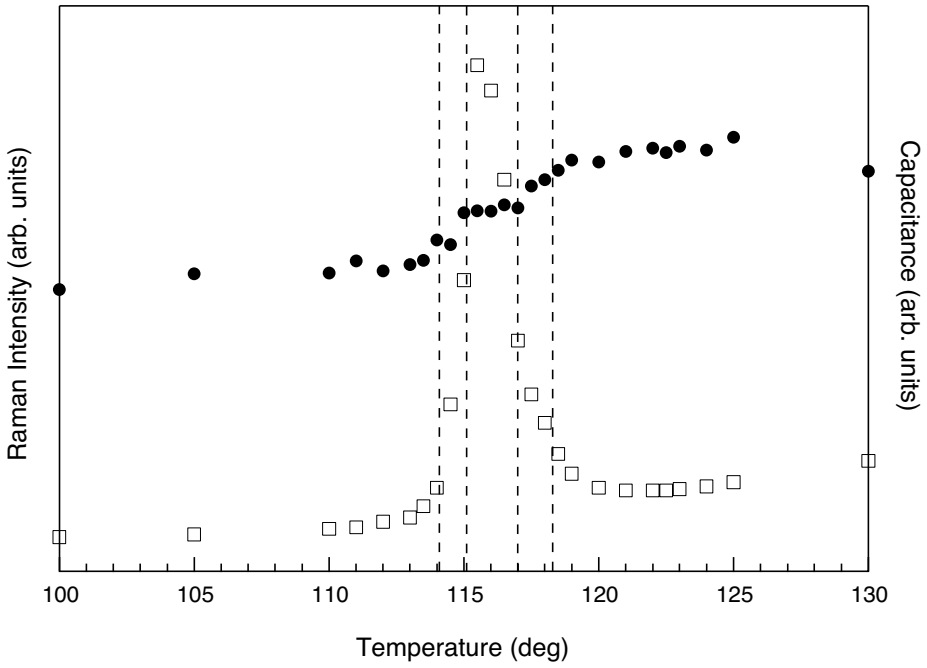

Figure 3.5: Temperature dependence of the capacitance (□) and the polarized intensity of phenyl line (•). The vertical broken lines show transition temperatures. The phase sequence is SmA – SmC_α* – SmC* – SmC_γ* – SmC_A*.

are shown with solid lines in Fig. 3.4. Their Raman shifts and activities are consistent with measured spectra. The calculated Raman tensors are also listed in the table. It was confirmed that each $\alpha_{z'z'}$ is considerably large compared to other components and thus these Raman lines are suitable for the evaluations of the orientational order parameters. The calculated angles between the z' axis and the biphenyl link are about 10° for phenyl line and chiral CO line, and almost 0° for core CO line. It was found that all of the z' axes of the Raman tensors lie towards the molecular long axis.

The capacitance and the polarized component of the phenyl line at $\omega = 0$ were obtained by the parallel measurement in the cooling process. The results are plotted as a function of the temperature in Fig. 3.5. The capacitance gradually decreased from the high temperature side down to 120°C, then it leaped to the maximum at 115°C. Thereafter, it dropped around 113°C and became steady. On the other hand, the Raman intensity decreased from 118°C to 113°C. This decrease in the Raman intensity would be mainly owing to the increase of the Θ after SmA–SmC_α* phase transition [14],

as explained before. [Refer to Eqs. (3.20)–(3.23).] The drastic change of the observed capacitance gave a good indication of the transition temperature, as shown in Fig. 3.5.

The helical pitches of the homogeneous cell used here were three or four times longer than the value reported for free standing film in SmC^* and SmC_A^* phase [28, 72]; i.e., 1700 nm in the SmC^* phase and 2000–4000 nm in the SmC_A^* phase. The substrates affect the helical pitch by wall anchoring effects. In SmC_γ^* phase, the helical pitch was too long to be measured by the diffraction method. Judging from the values in SmC^* and SmC_A^* phase, it was estimated around 8000 nm.

The polarized and depolarized components of the Raman scattering for the three Raman lines measured at 115.6°C (SmC^* phase) are plotted against the polarization direction of incident laser light in Fig. 3.6. The solid lines show the fitting results by Eqs. (3.20)–(3.24), where the parameters a, b, $\langle P_2(\cos\beta')\rangle$, $\langle P_4(\cos\beta')\rangle$, and R were determined by the fitting procedure under the assumption of the cylindrical symmetric Raman polarizability tensors for a molecule. The other parameters used here are summarized in Table 3.2, where layer tilt angles Ψ and molecular tilt angles Θ had been given by previous workers [4, 14], and H is the helical pitch.

The obtained orientational order parameters $\langle P_2(\cos\beta')\rangle$ and $\langle P_4(\cos\beta')\rangle$ are shown in Fig. 3.7. Sticks show the errors that were evaluated from the standard deviation of the fitting process. The error for $\langle P_4(\cos\beta')\rangle$ is larger than $\langle P_2(\cos\beta')\rangle$ because of the larger sensitivity to the Raman intensity. In SmA phase, the order parameter evaluated from the phenyl line is agreed with the values reported by Kim *et al.* [14]. All $\langle P_2(\cos\beta')\rangle$ gradually increased with decreasing temperature, as one generally expected for the ordering process of liquid crystal. It should be noted that a bit smaller value of $\langle P_2(\cos\beta')\rangle$ for core CO line than for the other lines was obtained. This small difference in the value would give the angle β_0 between the z' axis of the Raman tensor and the molecular long axis, as described in discussion. On the other hand, $\langle P_4(\cos\beta')\rangle$ exhibited drastic variation as temperature was decreased, that is, it smoothly increased in SmA phase, scattered in SmC_α^*, SmC^*, SmC_γ^* phases, and dropped in SmC_A^* phase.

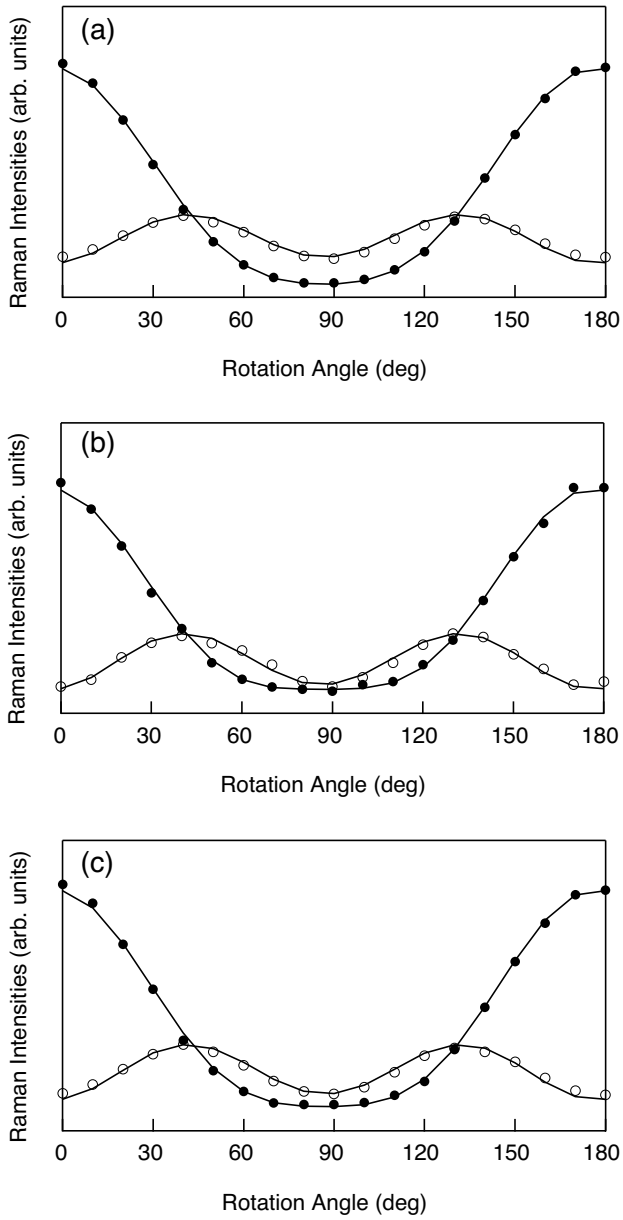

Figure 3.6: The dependence of the polarized Raman intensities on the polarization direction of incident laser light at 115.6°C (SmC^* phase) for phenyl line (a), core CO line (b), chiral CO line (c). Solid marks are $I_{\parallel}(\omega)$ and open marks are $I_{\perp}(\omega)$. The lines show the results of the fitting with Eqs. (3.20) and (3.21).

Table 3.2: Parameters used in the fitting. n_Z, n_Y, Ψ and Θ are taken from references [4, 14, 31].

Phase	Temp. (°C)	n_Z [31]	n_Y [31]	Ψ [4] (deg.)	Θ [14] (deg.)	H (nm)
SmA	140	1.63	1.50	6	–	–
	130	1.63	1.50	7	–	–
	121	1.63	1.50	8	–	–
	118.4	1.63	1.50	10.5	–	–
SmC_α*	117.2	1.63	1.50	12	12	–
SmC*	115.6	1.63	1.50	13.5	15	1700
SmC_γ*	114.8	1.63	1.50	14	16.5	8000
SmC_A*	113	1.62	1.50	15	18.5	–
	100	1.62	1.50	16.5	23	–
	90	1.62	1.50	17	24.5	–

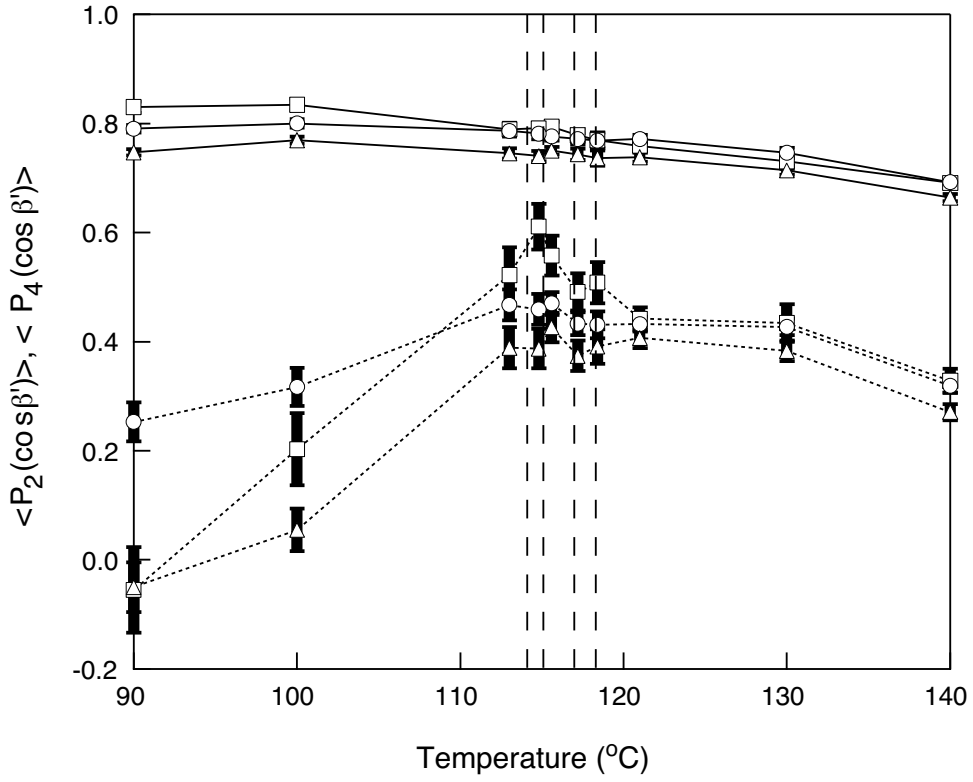

Figure 3.7: The second- and the fourth-order orientational order parameters, $\langle P_2(\cos\beta')\rangle$ and $P_4(\cos\beta')$; $\circ$, phenyl line; $\triangle$, core CO line; $\square$, chiral CO line. The solid lines show $\langle P_2(\cos\beta')\rangle$ and the dotted lines show $P_4(\cos\beta')$. The vertical broken lines show transition temperatures.

3.5 Discussion

3.5.1 Orientational order parameter in SmA phase

In SmA phase, $\langle P_2(\cos\beta')\rangle$ and $\langle P_4(\cos\beta')\rangle$ gradually increased with decreasing temperature. This phenomenon is as one generally would expect for the ordering process of liquid crystals. The small differences of $\langle P_2(\cos\beta')\rangle$ and $\langle P_4(\cos\beta')\rangle$ for core CO line from those for the other lines are noted in Fig. 3.7. According to Eqs. (3.22) and (3.23) the angle β_0 of core CO line is evaluated as 9° when z' axes of phenyl and chiral CO lines were assumed to be identical with the molecular long axis. The common statistics under the assumption of the cylindrical symmetry could be adopted for the molecular orientational distribution in SmA phase.

3.5.2 The biaxial orientational distribution of molecules in SmC* and its variant phase

The value of $\langle P_4(\cos\beta')\rangle$ exhibited a peculiar variation after SmC_α* phase. The dispersion in variation in SmC_α*, SmC*, SmC_γ* phases and decrease in SmC_A* phase are unusual under the assumption of the cylindrically symmetric orientational distribution of molecules. This discrepancy would be caused by the breakdown of the assumption of the uniaxiality for the molecular orientational distribution. It has been suggested that the rotation of the C=O group around the molecular long axis is hindered in SmC* and its subphases [21, 68].

Now the orientational order parameters $\langle D^{(L)*}_{m'm}(\Omega)\rangle$ must be introduced to express the biaxiality of the molecular orientational distribution [10] , and the polarized Raman intensities are given by the functions of $\langle D^{(L)*}_{m'm}(\Omega)\rangle$ and the structural parameters.

When the molecular orientational distribution function $f_{\rm mol}(\alpha,\beta,\gamma)$ has a relation of $f(\alpha,\beta,\gamma) = f(\pi+\alpha,\pi-\beta,\pi+\gamma)$, $f(\alpha,\beta,\gamma)$ can be expanded with Wigner rotation matrix in the molecular orientation frame as follows [10].

$$f(\Omega) = \sum_{L=\text{even}} \sum_{m,m'=-L}^{L} \frac{2L+1}{8\pi^2} a^{(L)}_{m'm} D^{(L)}_{m'm}(\Omega), \tag{3.27}$$

where Ω represents α, β, and γ. $a^{(L)}_{m'm}$ is given by

$$a^{(L)}_{m'm} = \int_0^{2\pi} d\alpha \int_0^{\pi} \sin\beta d\beta \int_0^{2\pi} d\gamma D^{(L)*}_{m'm}(\Omega) f(\Omega) = \left\langle D^{(L)*}_{m'm}(\Omega) \right\rangle . \tag{3.28}$$

When it is taken into account that the system has a cylindrical symmetry about Z_l axis because of the helical structure and the Raman tensor frame is tilted against the molecular fixed frame, the polarized Raman intensities are given by the same equations (3.20) and (3.21). Here $\langle P_L(\cos\beta_{\rm app})\rangle$ is related to $\left\langle D^{(L)*}_{m'm}(\Omega) \right\rangle$ by

$$\langle P_L(\cos\beta_{\rm app})\rangle = \sum_{m,m'=-L}^{L} A^{(L)}_{m'm}(\Theta, \alpha_0, \beta_0, \gamma_0) \langle D^{(L)*}_{m'm}(\Omega)\rangle, \tag{3.29}$$

where the coefficient $A^{(L)}_{m'm}(\Theta, \alpha_0, \beta_0, \gamma_0)$ is a function of Θ, α_0, β_0, and γ_0; e.g., when $m = m' = 0$, $A^{(L)}_{00} = P_L(\cos\Theta) P_L(\cos\beta_0)$.

At present, it is supposed that molecular distribution is biaxial and the molecule can rotate around its long axis freely. Then,

$$\langle P_L(\cos\beta_{\rm app})\rangle = P_L(\cos\Theta) P_L(\cos\beta_0) \sum_{m=-L}^{L} \langle D^{(L)*}_{0m}(\alpha, \beta)\rangle. \tag{3.30}$$

$\langle P_4(\cos\beta_{\rm app})\rangle$ is independent of γ, because the z' axis distributes uniaxially around z axis. $\langle D^{(L)*}_{00}(\Omega)\rangle$ correspond to $\langle P_L(\cos\beta)\rangle$ and depends on only β. It was deduced from the above equation that the decrease of $\langle P_4(\cos\beta_{\rm app})\rangle$ in SmC_A* phase was due to the terms $\langle D^{(L)*}_{0m}(\alpha, \beta)\rangle_{m\neq 0}$ and the different β_0 for each Raman line caused the scattering of $\langle P_4(\cos\beta_{\rm app})\rangle$ at lower temperature range than the SmA–SmC_α* phase transition. On the other hand, $\langle P_4(\cos\beta_{\rm app})\rangle$ of phenyl line and chiral CO line exchanged their order with each other in this phase. This phenomenon can not be explained by Eq. 3.30, since β_0 is constant for the temperature variation and Θ and $\langle D^{(L)*}_{0m}(\alpha, \beta)\rangle$ are independent of Raman line.

Accordingly, it was inferred that the molecular rotation around its long axis is hindered. Then Eq. (3.29) is obtained. [Compare with Eqs. (3.22), (3.23), and (3.30).] It is supposed tentatively that the molecular rotation around its long axis is perfectly restricted as $\alpha = 0$ and $\gamma = 0$ and the Raman tensor of a molecule has a cylindrical symmetry. When $\alpha_0 = 0$, then $\beta_{\rm app} = \Theta + \beta + \beta_0$ is obtained and $\langle P_L(\cos\beta_{\rm app})\rangle$ is reduced. Meanwhile when $\alpha_0 = \pi$, $\beta_{\rm app} = \Theta + \beta - \beta_0$ and $\langle P_L(\cos\beta_{\rm app})\rangle$ is increased.

Similarly, when $\alpha = 0$, $\gamma = \pi$, and $\alpha_0 = 0$, then $\beta_{\rm app} = \Theta + \beta - \beta_0$. That is, $\langle P_L(\cos\beta_{\rm app})\rangle$ largely depends on the value of α_0, a hindered direction, and a strength of hindrance to the molecular rotation around its long axis.

$\langle D^{(4)*}_{m'm}(\Omega)\rangle$ are higher order parameters than $\langle D^{(2)*}_{m'm}(\Omega)\rangle$. The higher order parameter generally exhibits sharper variation to the change of orientational distribution. On the other hand, $\langle D^{(4)*}_{00}(\Omega)\rangle$ is originally minor term than $\langle D^{(2)*}_{00}(\Omega)\rangle$. Then small disturbance by the $\langle D^{(4)*}_{m'm}(\Omega)\rangle$ looks much exaggerated to the minor term of $\langle D^{(4)*}_{00}(\Omega)\rangle$. This would be the reason why the apparent $\langle P_4(\cos\beta')\rangle$ showed more drastic reduction and scattering by the hindrance of molecular rotation than $\langle P_2(\cos\beta')\rangle$.

Following image could be drawn for a relation between the phase and the molecular orientational distribution. In SmA phase, MHPOBC molecule distribute uniaxially around its director. After transition to SmC_α* phase, the molecules tilt away from the helical axis, so that the orientational distribution could be biaxial. In this phase, the molecular rotation around its long axis might be somewhat hindered, and the apparent orientational order parameters show scattering due to different values of α_0 and β_0 for each Raman line. Then, in the SmC_A* phase, the molecular rotation is rather hindered and the hindered direction might be changed as reported before [21,68] while the biaxiality of the molecular orientational distribution is increased, thus the apparent $\langle P_4(\cos\beta')\rangle$ is reduced.

3.6 Conclusions

The equation of the polarized Raman intensity was derived as a function of the orientational order parameter and the polarization direction of incident laser light, where it was taken into account how the structure influences the optical properties in SmC* and the subphases. The polarized Raman scattering measurements of MHPOBC without any external field were analyzed according to this equation, and the second- and the fourth-order orientational order parameters were evaluated in the successive smectic phases. The unusual decrease in the orientational order parameters were observed in SmC_A* phases with decreasing of temperature. It was indicated that they stemmed from the growth of the biaxiality of the molecular orientational distribution as tem-

perature decreases because of the hindrance of the molecular rotation around its long axis.

Chapter 4

Molecular Ordering Deformation Induced by Externally Applied Electric Field in an Antiferroelectric Liquid Crystal

[Published in Japanese Journal of Applied Physics, in press (2002)]

4.1 Introduction

Ferro- [24] and antiferroelectricities [25] were found in the tilted smectic liquid crystal. The properties of the electro-optic phenomena in those phases are expected for applications to displays [25, 78]. Although the mechanisms of the appearance of the two phases have not been understood completely so far, it is of no doubt that interlayer interactions such as local dipole-dipole interaction and steric interaction play important roles [4,65,68,79,80]. The tilted subphases are characterized by the arrangement of the $\boldsymbol{c}$-director, which is a unit vector representing the molecular tilting sense around the smectic layer normal. The antiferroelectric SmC_A* phase is constructed by the repetition of the anticlinic bilayer structure in which the azimuthal angle of the $\boldsymbol{c}$-director, ϕ, is altered by π between the layers. When the homogeneously aligned sample cell

of the antiferroelectric liquid crystal is observed by a polarizing microscope with the crossed Nicol configuration where two polarizers cross each other and the layer normal is parallel to one of the polarizers, the tristable electro-optic response is observed [81].

A small transmission of light is frequently observed in the pretransitional regime below the critical electric field where the transition from antiferro- to ferroelectric phase takes place [69, 81]. Occasionally, a very intense transmission in the pretransitional regime is observed [69]. This electro-optic phenomenon in the pretransitional regime of the antiferroelectric phase shows that the difference in ϕ of the adjacent layers, $\Delta\phi$, deviates from π and the averaged molecular orientation tilts from the layer normal. This deviation of $\Delta\phi$ from π causes the appearance of spontaneous polarization. Wang *et al.* [82], and Qian and Taylor [83] have shown theoretically that the molecular reorientation like the nematic Fréedericksz transition occurs due to this spontaneous polarization, and Zhang *et al.* [84] and Wen *et al.* [85] have observed it by optical measurement. The deviation is closely related to the interlayer interaction. Therefore, the molecular reorientation in the pretransitional regime provides the essential information about the molecular interaction between adjacent layers.

In this chapter, the molecular reorientation of the homogeneously aligned antiferroelectric liquid crystal, which is induced by an externally applied electric field, is investigated by polarized Raman scattering measurements. The distribution of the $\boldsymbol{c}$-director along the axis perpendicular to the substrate plane, or Y axis, is estimated by a model calculation. Comparison of the theory with the results obtained by the model calculation shows the necessity of reconsidering the theoretical treatment of the interlayer interaction and/or the process in the molecular reorientation induced by an external electric field.

4.2 Experiment

The antiferroelectric liquid crystal sample used here is CS-4001 (Chisso Co.), which shows the following phase sequence: isotropic – (88.2°C) – SmA – (70.9°C) – SmC^* – (69.4°C) – SmC^*_γ – (68.6°C) – SmC^*_A. The spontaneous polarization, P_s, is 7.97×10^{-4} C m^{-2} at 25 °C.

A homogeneously aligned cell of 4 μm thickness was prepared by sandwiching the sample between two quartz substrates that were separated by spacer particles. The substrates were coated with ITO ($\sim$50 nm thick, $\sim$100 Ω/sq., $\sim$80% transmission at 500 nm) and aligning polyimide (Nissan Chemical, RN-1266, $\sim$200 nm thick). Only one of the substrates was rubbed in one direction and sense. The cell was mounted in a temperature-controlled oven ($\pm$0.1 K). Texture observation by a polarizing optical microscope (Olympus, BX50) was performed to check the quality of alignment before and after the polarized Raman scattering measurements.

Raman spectra were measured in the backward scattering geometry along the Y_{meas} axis perpendicular to the substrate plane [86–88]. The Z_{meas}- and X_{meas}-polarized Raman spectra were obtained by rotating the sample cell from 0° to 180° about the Y_{meas} axis when the incident laser was polarized along the Z_{meas} axis. Here the X_{meas}, Y_{meas}, and Z_{meas} axes constitute the right-handed measurement coordinate frame. The Raman line at 1600 cm^{-1}, which is assigned to the C-C stretching mode of benzene ring, is suitable for the probe investigating the molecular ordering because this line is well separated from the other lines and the tensor is almost parallel to the molecular long axis. The Z_{meas}- and X_{meas}-polarized Raman lines at 1600 cm^{-1} were fitted with a Lorentzian curve and the integrated intensities, $I_{\parallel,\mathrm{meas}}$ and $I_{\perp,\mathrm{meas}}$, were calculated. The depolarization ratio of the Raman line in the isotropic phase, $R_{\mathrm{iso}} = I_{\parallel,\mathrm{meas}}/I_{\perp,\mathrm{meas}}$, is 0.386. The green light at 514.5 nm from an Ar-ion laser (Spectra-Physics, BeamLok 2060) was used for excitation. The beam was focused on a well-aligned area of the sample cell. The diameter of a focused spot was about 700 μm. The scattered light was collected by a telescope lens (f = 130 mm and f/d = 1.3) and focused on an optical fiber that transmitted the light to a monochromator (Spex, 270M) combined with a multichannel detector (Princeton Instruments, IPDA 512). The incident laser power was set at 0.5 W and the slit width of the monochromator was 200 μm.

The intensity of the laser light passing the cell and a polarizer that was set in the crossed Nicol configuration was measured by a photodiode. The electro-optic response was monitored for confirmation of the tristable switching.

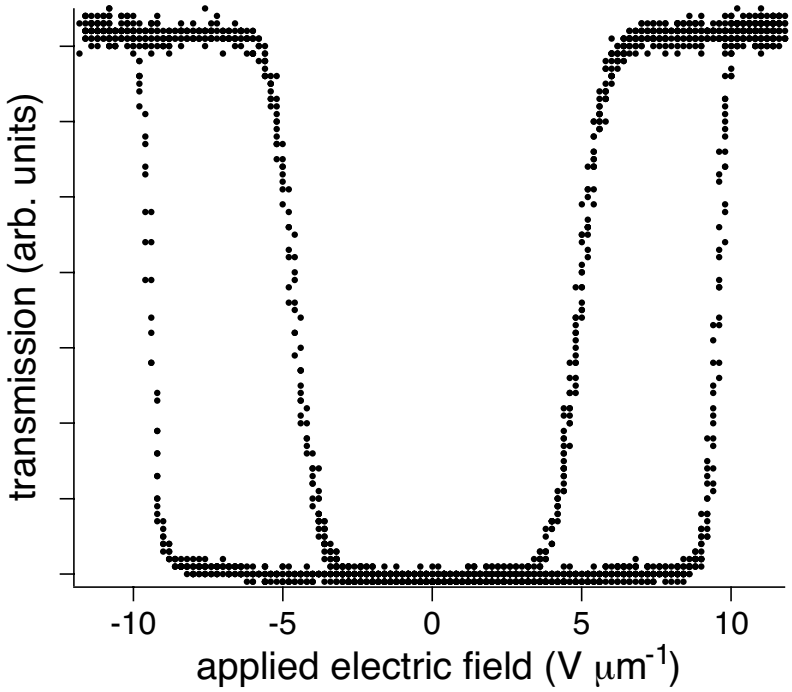

Figure 4.1: Tristable electro-optic response of CS-4001 in SmC_A^* at a frequency of 1 Hz triangular waveform field (40°C).

4.3 Results

Figure 4.1 shows the electro-optic response at the frequency of 1 Hz in the crossed Nicol configuration where the layer normal is perpendicular to the analyzer. The electro-optic response exhibits typical tristable switching with a small pretransitional phenomenon. The critical field of the transition from antiferro- to ferroelectric phase is approximately 9 V μm^{-1}. The small pretransitional phenomenon below the critical field strength is observed. This shows that the averaged molecular orientation deviates a little from the layer normal and the deviation of $\Delta\phi$ from π is small.

Figure 4.2 shows the polar plots of polarized Raman intensities of the phenyl C-C stretching mode under the static electric field at 40°C. Figure 4.2(a) was obtained at the initial state without applying any electric field, which is prepared by cooling down from the isotropic phase. Figures 4.2(b) and 4.2(c) were obtained in the pretransitional regime and Fig. 4.2(d) was obtained in the field-induced ferroelectric phase. The Raman intensities of the phenyl C-C stretching mode at 1600 cm^{-1} are plotted

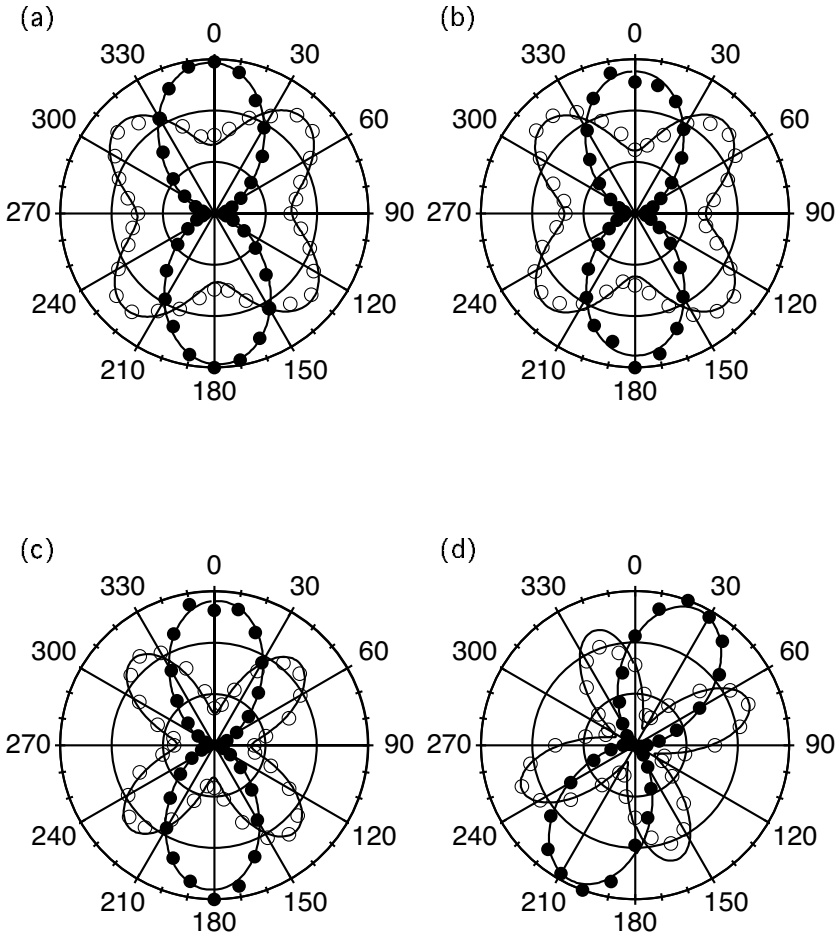

Figure 4.2: Polar plots of polarized Raman intensities of the phenyl C-C stretching mode at 1600 cm^{-1} (in arbitrary units) as a function of the rotation angle of the sample cell (in degrees) at (a) the initial state without any electric field, (b) 3.5 V $\mu\mathrm{m}^{-1}$, (c) 9.2 V $\mu\mathrm{m}^{-1}$, and (d) 11.5 V $\mu\mathrm{m}^{-1}$: •, $I_{Z,\mathrm{meas}}$; ∘, $I_{X,\mathrm{meas}}$. The solid lines show the best-fitting results in the analyses.

against the rotation angle of the cell, ω'. The points at $\omega' = 0$ and 180° indicate that the layer normal is parallel to the polarization direction of the incident laser light; $\omega' = \omega + \Delta\omega$, where $\Delta\omega$ is the deviation of the molecular averaged orientation axis from the layer normal. The maximum point of $I_{\parallel,\mathrm{meas}}(\omega')$ gives the molecular averaged orientation. It stays almost parallel to the layer normal below the critical electric field [Figs. 4.2(a)–4.2(c)] and it tilts at 24.6° above that field [Fig. 4.2(d)]. The averaged orientation tilts only 2.9° from the layer normal even at 9.2 V $\mu\mathrm{m}^{-1}$ just below the critical electric field [Fig. 4.2(c)]. This agrees with the small pretransitional phenomenon in the electro-optic response as shown in Fig. 4.1. However, it is obvious that the intensity of $I_{\perp,\mathrm{meas}}(0°)$ decreases as the applied electric field strength increases. This shows that some molecular reorientation is induced by the electric field although the antiferroelectric ordering is kept.

When the Raman polarizability tensor of the phenyl C-C stretching mode has cylindrical symmetry, the $I_{\parallel,\mathrm{meas}}(\omega)$ and $I_{\perp,\mathrm{meas}}(\omega)$ give the apparent 2nd- and 4th-order 'molecular' orientational order parameters by means of the fitting procedure described in Chapter 2 [86, 88] because the longest principal axis of the tensor is almost parallel to the molecular long axis. It should be noted that the 'apparent' orientational order parameters obtained here represent not only the thermal fluctuation for an individual molecule but also the 'averaged' molecular distribution which is projected to the XZ plane when it is macroscopically observed along the Y axis (cf. Chapter 3) [86–88]. Even for an arbitrary molecular distribution, which may not be cylindrically symmetric, the apparent center axis of the molecular distribution can be still determined so that $I_{\parallel,\mathrm{meas}}(\omega)$ and $I_{\perp,\mathrm{meas}}(\omega)$ are written in the same forms as Eqs. (2.60) and (2.70), provided that $\langle P_2(\cos\beta)\rangle$ and $\langle P_4(\cos\beta)\rangle$ are regarded as the corresponding apparent ones, $\langle P_2(\cos\beta)\rangle_{\mathrm{app}}$ and $\langle P_4(\cos\beta)\rangle_{\mathrm{app}}$ (see Section 3.5). The molecular orientational distributions that will be studied in this chapter are not generally cylindrically symmetric; hence $\langle P_2(\cos\beta)\rangle_{\mathrm{app}}$ and $\langle P_4(\cos\beta)\rangle_{\mathrm{app}}$ will be determined by using experimentally obtained $I_{\parallel,\mathrm{meas}}(\omega)$ and $I_{\perp,\mathrm{meas}}(\omega)$.

The solid lines in Figs. 4.2(a)–4.2(d) show the best-fitting results by Eq. (2.60) and (2.70). Here, we use $n_{\mathrm{g}} = 1.46$, $n_X = 1.5$, and $\Delta n \equiv n_Z - n_X = \Delta n_0 \langle P_2(\cos\beta)\rangle$ with $\Delta n_0 = 0.15$ in the analysis. Typical errors in the fitting process are 0.02 for

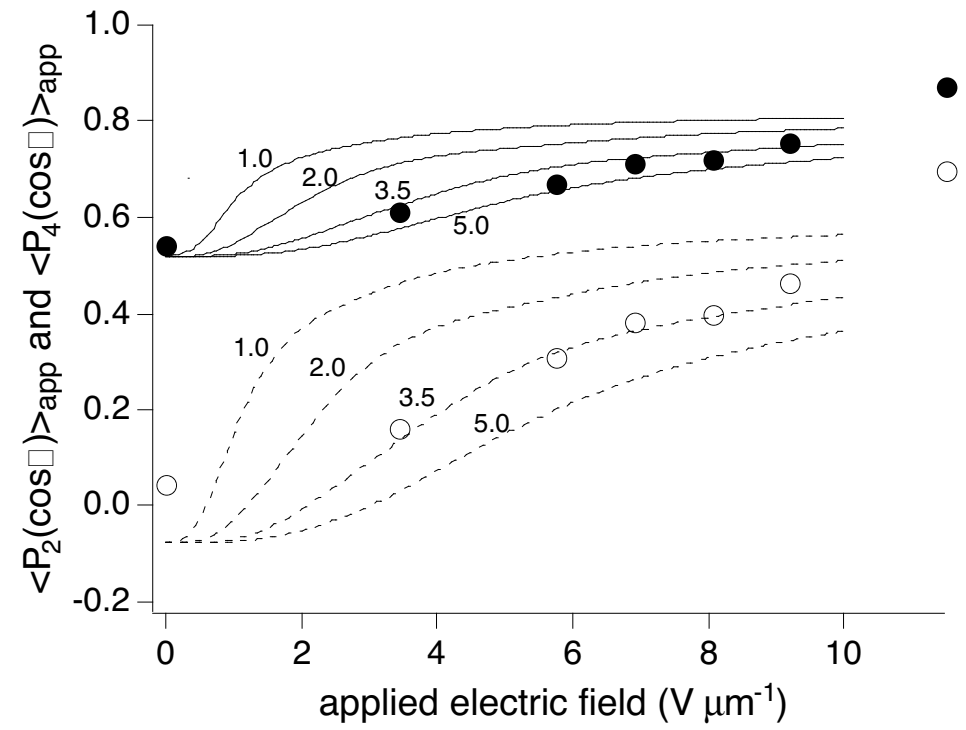

Figure 4.3: Apparent orientational order parameters under static electric field, •: $\langle P_2(\cos\beta)\rangle_{\rm app}$; ○: $\langle P_4(\cos\beta)\rangle_{\rm app}$. The solid lines and dotted lines are $\langle P_2(\cos\beta)\rangle_{\rm app}$ and $\langle P_4(\cos\beta)\rangle_{\rm app}$ given by the model calculation. The numbers beside the lines show the values of $\xi_b E$; 1.0, 2.0, 3.5 and 5.0 V.

$\langle P_2(\cos\beta)\rangle_{\rm app}$ and 0.03 for $\langle P_4(\cos\beta)\rangle_{\rm app}$, respectively. The obtained orientational order parameters from polarized Raman scattering are shown in Fig. 4.3 as a function of the static electric field intensity. The order parameters are very small at the initial state without applying any electric field strength and gradually increase with increasing applied electric field strength. When the applied field exceeds the critical field strength (9.5 V μm^{-1}) and thus the ferroelectric phase is induced, the order parameters reach the highest values. It is confirmed that the continuous molecular reorientation is induced by the electric field in the pretransitional regime while keeping the antiferroelectric anticlinic molecular ordering.

4.4 Model Calculation

It was experimentally found that the molecular reorientation is induced by the external applied electric field in the pretransitional regime. The orientational order parameters are apparent as mentioned above and, therefore, in the tilted antiferroelectric smectic phase, they depend not only on the molecular thermal fluctuation but also on the spatial distribution of the $\boldsymbol{c}$-director in the sample cell [86–88]. The applied electric field used in this experiment suppresses the $\boldsymbol{c}$-director fluctuation but it hardly affects the molecular thermal fluctuation about the molecular long axis and the molecular tilting angle from the layer normal. Therefore, the change in the orientational order in the pretransitional regime indicates that the $\boldsymbol{c}$-director reorientation is induced. To elucidate the $\boldsymbol{c}$-director reorientation in the pretransitional regime, a simple analog of nematic $\boldsymbol{n}$-director reorientation under an electric field in a homogeneous alignment cell is assumed. The spatial distribution of the $\boldsymbol{c}$-director is reproduced, the orientational order parameters are calculated for the given distribution, and the results of these model calculations are compared with the experimental results.

4.4.1 Spatial distribution of the $\boldsymbol{c}$-director along the Y axis

In the case of the homogeneously aligned nematic sample cell, the molecular reorientation is induced by an external electric field due to the dielectric anisotropy of the molecule [89]. If the molecule is strongly anchored to the substrate surface, the nematic $\boldsymbol{n}$-director is deformed along the Y axis when an electric field exceeding the Fréedericksz transition point is applied to the cell. Here the y axis is perpendicular to the substrate plane. The distribution of the nematic $\boldsymbol{n}$-director along the Y axis is given by [89]

$$\tan(\pi/4 - \theta_{\mathrm{n}}/2) = \exp(-Y/\xi_{\mathrm{n}}) + \exp[(-d + Y)/\xi_{\mathrm{n}}] - \exp(-d/\xi_{\mathrm{n}}). \tag{4.1}$$

Here, θ_{n} is the angle between the $\boldsymbol{n}$-director and the substrate plane, d is the thickness of the sample, Y is the displacement from the substrate surface, and ξ_{n} is given by

$$\xi_{\mathrm{n}} = \sqrt{\frac{K}{\Delta\epsilon E^2}}, \tag{4.2}$$

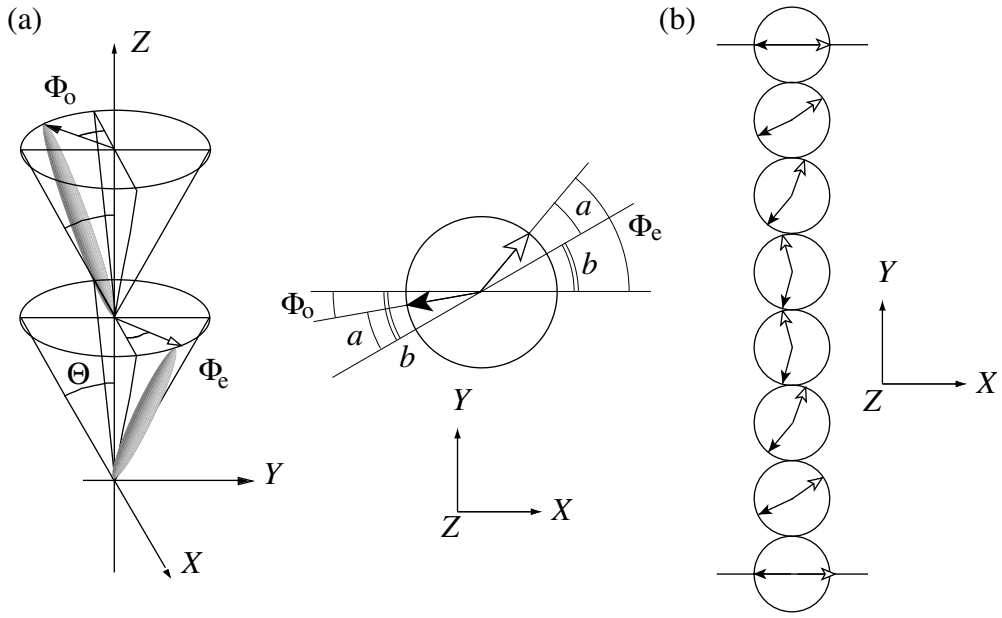

Figure 4.4: Illustrations of the orientational geometry for the model calculation in §4.4. (a) Bilayer structure in the SmC_A* and its projection to the xy-plane parallel to the smectic layer. The xz-plane is parallel to the substrate and the z-axis is perpendicular to the smectic layer. The bookshelf layer structure is assumed. The open and filled arrows represent the $\boldsymbol{c}$-director in the even and odd numbered layers, respectively. The molecule tilts at Θ with respect to the layer normal. (b) The spatial distribution of the $\boldsymbol{c}$-director reorientation along the y-axis in the pretransitional regime. The molecules at both surfaces are fixed as $\phi_e = \phi_o = 0$ or $b = 0$.

where K is the elastic constant, $\Delta\epsilon$ is the dielectric anisotropy, and E is electric field strength applied along the Y axis. The parameter, ξ_{n}, is the 'electric' coherence length and dominates the distribution of the nematic $\boldsymbol{n}$-director along the Y axis.

The case in the antiferroelectric phase is considered [83]. The geometry based on the double-layered structure model with the bookshelf structure is presumed for simplicity, as illustrated in Fig. 4.4(a). The X, Y, and Z axes constitute the right-handed layer frame. The Y axis is perpendicular to the substrate plane and parallel to the Y axis. The Z axis is perpendicular to the layer. The molecules tilt at Θ with respect to the Z axis or the layer normal. Φ_{e} and Φ_{o} are the angles between the substrate plane and the $\boldsymbol{c}$-directors of the even and odd numbered layers, respectively.

Here, $a = (\Phi_e - \Phi_o)/2$ and $b = (\Phi_e + \Phi_o)/2$. $a = 0$ and $a = \pi/2$ give perfectly aligned anticlinic antiferroelectric and synclinic ferroelectric ordering, respectively. At the initial state without any electric field, the liquid crystal molecules are assumed to be in the surface stabilized state with strong anchoring and uniform spatial distribution of the $\boldsymbol{c}$-directors; i.e., $a = 0$ and $b = 0$ at any Y. This is supported by an optical microscope observation. The optical microscope observation shows that the texture at the initial state is recovered from the state with an applied electric field unless the field strength exceeds the critical one, which is higher than the critical field strength inducing the phase transition. The electric spontaneous polarization within a layer, of which magnitude is P_0, is perpendicular to the $\boldsymbol{c}$-director and the layer normal. The spontaneous polarizations at even and odd layers cancel out when $a = 0$. When an electric field exceeding the Fréedericksz transition point is applied along the Y axis, a deviates from zero and the polarization $P_0 \sin a$ appears. This polarization brings about the rotation of the $\boldsymbol{c}$-directors in the bulk while the $\boldsymbol{c}$-directors at the surface are fixed at $b = 0$ by the strong anchoring force. Thus, the deformation of the $\boldsymbol{c}$-directors occurs along the Y axis under the strong molecular anchoring condition [Fig. 4.4(b)]. In the present study, the dielectric anisotropy is negligible compared with P_0 [83, 85]. Qian and Taylor showed theoretically that the field-induced coherence length about b along the Y axis, ξ_b, is inversely proportional to the applied electric field strength [83]. Considering the analogy of the $\boldsymbol{c}$-director in the antiferroelectric phase to the nematic $\boldsymbol{n}$-director, it is found that θ_n and ξ_n correspond to b and ξ_b, respectively. The spatial distribution of b along the Y axis, $f_b(Y)$, is given by substituting the above parameters into eq. (4.1):

$$f_b(Y) = \pi/2 - 2\arctan\left[\exp\left(\frac{-Y}{\xi_b}\right) + \exp\left(\frac{-d+Y}{\xi_b}\right) - \exp\left(\frac{-d}{\xi_b}\right)\right]. \tag{4.3}$$

4.4.2 Calculation of the apparent orientational order parameters

Next, we need to construct the relation between the molecular orientational geometry in a single layer and the apparent orientational order parameters. The orientational order parameters obtained in the electric-field-induced ferroelectric phase represent the molecular distribution in a single layer. Since only the 2nd- and 4th-order terms contribute to the Raman scattering process, the molecular orientational distribution function in the ($X_{\rm E}$, $Y_{\rm E}$, $Z_{\rm E}$)-molecular orientation frame is well approximated by

$$\begin{aligned} & f_{\rm mol,E}(\alpha,\beta,\gamma) \\ & \quad = \sum_{L=0,2,4} \frac{2L+1}{8\pi^2} \langle P_L(\cos\beta)\rangle_{\rm E} P_L(\cos\beta). \end{aligned} \tag{4.4}$$

Here α, β, and γ are the Euler angles defined in the molecular orientation frame, and $\langle P_2(\cos\beta)\rangle_{\rm E}$ and $\langle P_4(\cos\beta)\rangle_{\rm E}$ are the 2nd- and 4th-order parameters experimentally obtained in the electric-field-induced ferroelectric SmC^* phase. $\langle P_2(\cos\beta)\rangle_{\rm E}$ and $\langle P_4(\cos\beta)\rangle_{\rm E}$ result principally from molecular level fluctuations and slightly from the imperfect alignment of the smectic layers as manifested by textures. In the (X, Y, Z)-layer frame, eq. (4.4) can be written as [11]

$$\begin{aligned} & f_{\rm mol,E}(\phi,\theta,\chi) = \tilde{R}(0,\Theta,0) f_{\rm mol,E}(\alpha,\beta,\gamma) \\ & \quad = \sum_{L=0,2,4} \sum_{m=-L}^{L} \frac{2L+1}{8\pi^2} \langle P_L(\cos\beta)\rangle_{\rm E} \\ & \qquad \times D^{(L)}_{m0}(0,\Theta,0) D^{(L)*}_{m0}(\phi,\theta,\chi), \end{aligned} \tag{4.5}$$

where θ, ϕ, and χ are the Euler angles in the (X, Y, Z)-layer frame, $\tilde{R}(0,\Theta,0)$ is the rotation operator that transforms the reference from ($X_{\rm E}$, $Y_{\rm E}$, $Z_{\rm E}$)-molecular frame to (X, Y, Z)-layer frame, and $D^{(L)}_{m0}$ is the rotation matrix [11, 90]. Convoluting the molecular fluctuation given by eq. (4.5) with the in-plane director distribution along the Y axis, $f_Y(\phi',\theta',\chi')$, we obtain the molecular orientational distribution function

$$\begin{aligned} & f_{\rm mol}(\phi,\theta,\chi) \\ & \quad = \int_0^d dy \int_0^{2\pi} d\phi' \int_0^{\pi} \sin\theta' d\theta' \int_0^{2\pi} d\chi' \\ & \qquad \times f_{\rm Y}(\phi',\theta',\chi') f_{\rm mol,E}(\phi-\phi',\theta-\theta',\chi-\chi'). \end{aligned} \tag{4.6}$$

Here,

$$f_Y(\phi', \theta', \chi') = \delta(\theta' - \Theta)$$
$$\times\{\delta\left[\phi' - f_b(Y)\right] + \delta\left[\phi' - f_b(Y) + \pi\right]\}. \tag{4.7}$$

From eqs. (4.4)–(4.7), we obtain the apparent molecular orientational Lth- (L=2 and 4) order parameters

$$\langle P_L(\cos\beta)\rangle_{\rm app} = \sum_{m=-L}^{L} \langle D_{m0}^{(L)*}(\phi, \theta, \chi)\rangle, \tag{4.8}$$

with

$$\begin{aligned}\langle D_{m0}^{(L)*}(\phi, \theta, \chi)\rangle &= \int_0^{2\pi} d\phi \int_0^{\pi} \sin\theta d\theta \int_0^{2\pi} d\chi \\ &\quad \times D_{m0}^{(L)*}(\phi, \theta, \chi) f_m(\phi, \theta, \chi).\end{aligned} \tag{4.9}$$

The model calculation with $\xi_b E = 3.5$ V gives good agreement with the experimental results (Fig. 4.3). At the initial state without any electric field, there is a slight difference between the model calculation and the experimental result. The model calculation at zero electric field gives the orientational order parameters in the surface stabilized antiferroelectric state with uniform spatial distribution. The difference between those orientational order parameters at zero electric field indicates that the distribution of the $\boldsymbol{c}$-director exists in the initial state. The helicity may remain partially at the initial zero electric field in such a relatively thick sample cell. This helix may be completely unwound at 4 V μm^{-1} in a thick sample cell [91]. The model calculation supports the mechanism proposed by Qian and Taylor for the molecular reorientation in the pretransitional regime [83].

4.5 Discussion

The electric coherence length ξ_b estimated here is $3.5/E$ m. The theoretical prediction of ξ_b is approximately given by the following equation derived by Qian and Taylor [83]:

$$\xi_b = \sqrt{\frac{4(U + 2J)K \sin^2\Theta}{P_0^2 E^2}}, \tag{4.10}$$

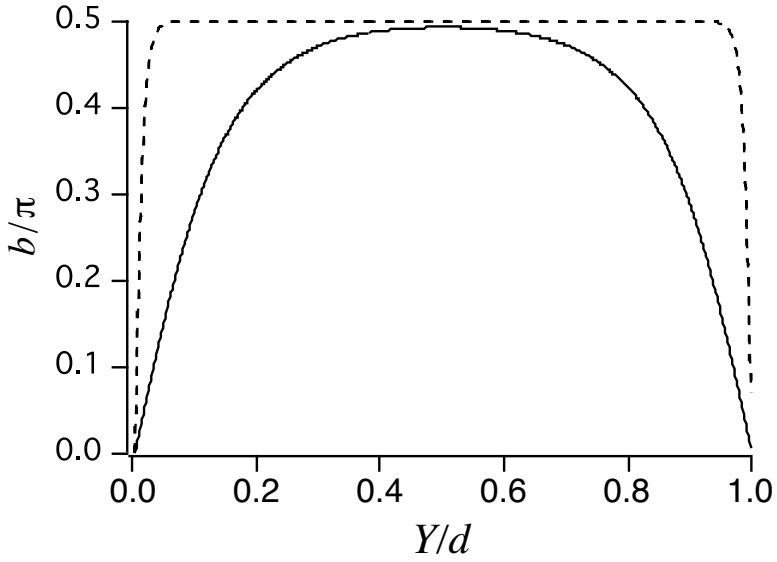

Figure 4.5: Spatial distribution of b along the y-axis at 9.2 V μm^{-1} just below the critical field. The solid line is calculated based on the experimental estimation ($\xi_b E =$ 3.5 V) and the broken line is from the theoretical prediction ($\xi_b E = 0.30$ V). The abscissa is normalized by the sample thickness, $d = 4$ μm.

where U and J are the coupling coefficients of the dipolar and quadrupolar terms in the expansion of the free energy of the interlayer interaction, f_{inter} [83, 92]:

$$f_{\text{inter}} = -U \cos 2a - \frac{J}{2} \cos 4a. \tag{4.11}$$

Here, $P_0 = 7.97 \times 10^{-4}$ C m^{-2} and $\Theta = 24.6°$. Parry-Jones and Elston have experimentally estimated $U = 2.2 \times 10^3$ J m^{-3} and $J = 2.9 \times 10^3$ J m^{-3} [92]. With $K = 10^{-11}$ N as a typical value, $\xi_b E = 0.30$ V is predicted. This predicted value is much shorter than the above estimation. This large discrepancy can be clearly seen in the distribution of b along the Y axis (Fig. 4.5). The value of b given by the theoretical model proposed by Qian and Taylor is almost constant in the bulk, but the experimental result indicates that b exhibits a large distribution even just below the critical electric field.

One may suspect that the presumed initial structure with uniform spatial distribution along the Y axis is not appropriate in the model calculation. Mottram and Elston suggested the twisted antiferroelectric state for the ground state with a strong polar anchoring condition [93]. When sufficient electric field is applied to the cell so

that b is $\pi/2$ in the middle of the sample cell, the uniform state and the twisted state show no difference in the apparent orientational order parameters because the averaged distributions of the c-director are almost identical in the antiferroelectric state with consideration of symmetry in the experiment. Therefore, the value of ξ_b at high field is independent of the initial state.

The discrepancy between the experimental result and the theoretical prediction is partially due to the reduction of the applied electric field strength. The alignment layer, the thickness of which is about one-tenth of the liquid crystal slab, reduces the applied electric field by 50% at the most due to its high resistance [84, 85, 94]. The ionic impurity, which is brought about by decomposing the polyimide due to the continuously incident laser light [95], also reduces the electric field to a certain extent. Moreover, there is uncertainty of the elastic constant. However, the above is not sufficient to explain such a large discrepancy. Previous works had also recognized the discrepancy between the theory and the experimental results at the critical electric field strength inducing Fréedericksz transition in the antiferroelectric phase [84,85]. The experimental value was at least twice as large as the theoretically predicted one. They have mentioned the simplicity in the model used there in addition to the uncertainty of the elastic constant as the cause of the discrepancy. The models used there and proposed by Qian and Taylor neglect sugh minor contributions as the next-nearest-neighbor contribution [96] that was mentioned by Wen *et al.* [85], the electrostatic effect due to the divergence of the spontaneous polarization [97], the higher terms in the expansion of the interlayer interaction, and the dielectric anisotropy.

We should mention the magnitude of spontaneous polarization. The biased direction of the liquid crystal molecule around its long axis is different between the antiferro- and ferroelectric phases [21, 68, 69]. Hence, the effective spontaneous polarization in a single layer, which is perpendicular to the tilting plane, is also different. The difference in the effective spontaneous polarization would be a major contributor to the discrepancy here because of the linear dependence on ξ_b as seen in Eq. (4.10). This difference in the effective spontaneous polarization should be considered in the theory treating the field-induced phase transition and its dynamic process that follows the balance of physical properties such as interlayer interaction, external field, and so on. These

changes in the biased direction and the consequent spontaneous polarization between these phases may be responsible for the cooperative effects in the phase transition.

4.6 Summary

The apparent orientational order parameters are obtained by polarized Raman scattering in the pretransitional regime from the antiferro- to ferroelectric smectic phase at various external electric field strengths. The order parameters increased with increasing electric field strength below the critical field strength where the transition from antiferro- to ferroelectric phase occurred, while the apparent tilt angle remained almost zero. The change in those parameters clearly revealed the reorientation of the $\boldsymbol{c}$-director. This reorientation of the $\boldsymbol{c}$-director was well represented by the equation that describes the field-induced deformation of a nematic $\boldsymbol{n}$-director. The estimated electric coherence length, which is inversely proportional to the applied field strength, was much larger than the theoretical prediction by Qian and Taylor. This suggests the necessity of a more precise description of the interlayer interaction in the tilted smectic phase, including the dependence of the effective spontaneous polarization on the phase.

Chapter 5

Orientational Distribution in Smectic Liquid Crystals showing V-shaped Switching Investigated by Polarized Raman Scattering

[Published in Physical Review Letter **87**, 015701 (2001) and Physical Review E **64**, 041714 (2001)]

5.1 Introduction

The electric field induced phase transition between SmC_A* and SmC* phases is, usually, of first order and characterized by dc threshold, hysteresis, and fingerlike boundary propagation; it is designated as the tristable switching (cf. Chapter 4). However, the electric-field-induced continuous reorientation of a spatially uniform optic axis was observed as the V-shaped switching or the thresholdless analogue optical effect in two kinds of mixtures consisting of some homologues of the prototyped antiferroelectric liquid crystals, MHPOBC and TFMHPOBC [43, 50–52, 98], which were designated as the Inui mixture [Fig. 5.1(A)] and the Mitsui mixture [Fig. 5.1(B)]. These materials exhibit ferro-, ferri-, and/or antiferroelectric phases in thick free-standing films, however, the

V-shaped switching is observed in thin homogeneous cells. It shows neither threshold nor hysteresis, and occurring uniformly without any boundary movement [43,50,53,98]. This peculiar switching has attracted much attention because of its potential applications to a new generation of liquid crystal displays [44–49].

The random switching model was proposed for the V-shaped switching. This switching was regarded as the Langevin-type reorientation process of local in-plane directors, the tilting directions of which are randomly distributed from smectic layer to layer. The tilting correlation of the local in-plane directors between adjacent layers was considered to be lost because of the frustration between ferroelectricity and antiferroelectricity [43, 50–53]. An increasing electric field causes the increasing net spontaneous polarization against the thermal agitation. Another explanation has also been made successfully by the effective internal field model [99]. Seomun *et al.* [100] and Pociecha [101] confirmed that substrate interfaces destroy the antiferroelectric order in thin homogeneous cells, apparently promoting the randomization of the local in-plane directors from layer to layer. Pociecha *et al.* recognized the importance of the frustration in their mixture and proposed a cluster model [101, 102]. They considered that their observed gradual evolution of polar properties results from the concentration change of ferroelectric and antiferroelectric clusters of sizes smaller than the visible light wavelength. There exists no big difference between the cluster and random models, if the concept of clusters is replaced by the correlation lengths parallel and perpendicular to the smectic layer, $\xi_{\parallel}$ and $\xi_{\perp}$, as introduced in the random model. The question concerning the loss of information about the tilting direction between layers is of high physical interest.

On the other hand, Takezoe *et al.* [54], Park *et al.* [23,55], Rudquist *et al.* [56], and Clark *et al.* [57] asserted the charge stabilization and/or the highly collective rotation of the local in-plane directors on the SmC^* tilt cone in the macroscopic scale, and that the frustration did not play any essential role. The polarized IR spectroscopic study indicated the almost complete director alignment parallel to a plane vertical to the substrate plates at zero electric field, which supports the collective rotation [23]. More recently, however, Seomun *et al.* showed that the alignment is not so ideal that supports the charge stabilization [95, 103, 104].

The purpose of this chapter is to understand the mechanism of the V-shaped switching. As a first step, a method of elucidating the alignments of local in-plane directors at the tip of the V was established by utilizing polarized Raman scattering [10, 11, 86, 87, 105]. I have studied the molecular alignments in the two materials, one component of the Inui mixtures [compound (a)] and the Mitsui mixture (Fig. 5.1). In both of the materials, the antiferroelectric phase exists at low temperatures in the bulk but is not stable enough in thin homogeneous cells. The V-shaped switching is always observed at least in the high-temperature region of the antiferroelectric phase. In compound (a), however, it is stable to some extent even in thin homogeneous cells, because the tristable switching is observed in the first-run while the V-shaped switching appears in the subsequence.

5.2 Experiment

Homogeneous cells of compound (a) and the Mitsui mixture listed in Fig. 5.1 were prepared by sandwiching the sample between two quartz substrates separated by spacer particles of 2 μm in diameter. The substrates were coated with indium tin oxide ($\sim$50 nm thick, $\sim$100 Ω/sq, $\sim$80 % transmission at 500 nm) and aligning polyimide (Nissan Chemical, RN-1266, $\sim$200 nm thick). The polyimide was carefully chosen to avoid the excess heating due to laser light absorption [95]. The only one of the substrates was rubbed in one direction and sense. The cell was mounted in a temperature-controlled oven ($\pm$0.1 K). The texture was monitored with a polarizing optical microscope (Olympus, BX50) for checking the alignment quality in each phase.

Raman spectra were obtained in the backward scattering geometry along the Y axis perpendicular to the substrate plates [86, 87]. The Z_{meas}- and X_{meas}-polarized Raman intensities, $I_{\parallel,\mathrm{meas}}$ and $I_{\perp,\mathrm{meas}}$, due to the C-C stretching mode of three benzene rings with a frequency of 1600 cm^{-1} were obtained by rotating the sample cell from 0° to 180° about the Y axis. Here the X, Y, and Z axes constitute the right-handed laboratory frame. The green light at 514.5 nm from an argon ion laser (Spectra-Physics, BeamLok 2060) was used for excitation. The beam was focused on a well-aligned area of the sample cell. The diameter of a focused spot was about 700 μm. The backscattered

(A)

(a) 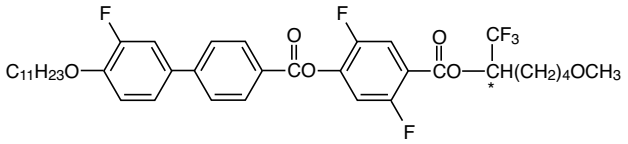

cryst. (ca. -31ºC) anti* (31ºC) ferri* (36ºC) SmA (46ºC) iso.

(b) 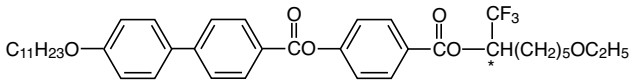

(c) 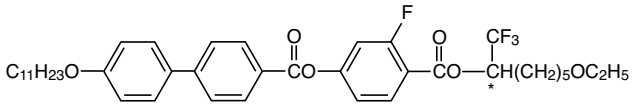

Inui mixture, a:b:c = 40:40:20 (by weight)

SmC_A* (43ºC) SmX* (64ºC) SmA (69ºC) iso.

(B)

(d) 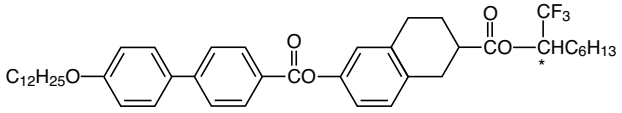

(e) 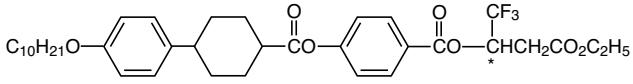

Mitsui mixture, d:e = 63:37 (by weight)

free-standing film; SmI* (32ºC) ferri* (34ºC) AF* (56ºC)
FI* (59ºC) SmC* (79ºC)SmA (100ºC) iso.

Figure 5.1: Chemical structures and phase sequences of (A) Inui mixture, (B) Mitsui mixture, and compound (a).

light was collected by a telescope lens ($f = 130$ mm and $f/d = 1.3$) and focused on an optical fiber, which transmitted the light to a monochromator (Spex, 270M) combined with a multichannel detector (Princeton Instruments, IPDA 512). The incident laser power was set at 0.5 W and the slit width of the monochromator was 200 μm.

The V-shaped switching was obtained by applying an electric field of triangular waveform to the cell at a frequency of 1 Hz. The scattered light at the tip of the V was detected by applying gated pulses of 4 msec width to the detector. I monitored laser light passing through the cell and a polarizer that was set in the crossed Nicol configuration by a photodiode during the Raman scattering measurement, confirming the V-shaped switching.

5.3 Results

Figure 5.2(A) shows the Raman spectra of compound (a) at 50 °C and Fig. 5.2(B) those of the Mitsui mixture at 110 °C in the isotropic phase. The Raman line due to the C-C stretching mode of phenyl rings at 1600 cm^{-1} used is well isolated from other lines. The principal axis with the largest Raman scattering tensor component, $\alpha_{\parallel}$, is almost parallel to the molecular long axis. Consequently, the orientational order parameters of the molecules can be determined by measuring the polarized Raman scattered intensities of the phenyl ring stretching line [86]. The depolarization ratios were 0.391 in compound (a) and 0.356 in the Mitsui mixture, respectively.

5.3.1 Compound (a)

The thin homogeneous cell of compound (a) shows a tristable electro-optic response at 26 °C in the antiferroelectric phase when a dc electric field E is applied statically. Raman intensities of phenyl line, $I_{\parallel,\mathrm{meas}}(\omega')$ and $I_{\perp,\mathrm{meas}}(\omega')$, are plotted against the rotation angle of the sample cell in Figs. 5.3(A)[(i)–(iii)]. The smectic layer normal is along the line connecting 0° to 180° in the figure. The maximum position of $I_{\parallel,\mathrm{meas}}(\omega')$, ω_0, gives the averaged molecular orientation; $\omega' = \omega + \omega_0$. The fitting procedures described in Chapter 2 give the apparent order parameters as summarized in Table 5.1(A). Here, $n_g = 1.46$, $n_X = 1.5$, and $\Delta n \equiv n_Z - n_X = \Delta n_0 \langle P_2(\cos\beta)\rangle$ with

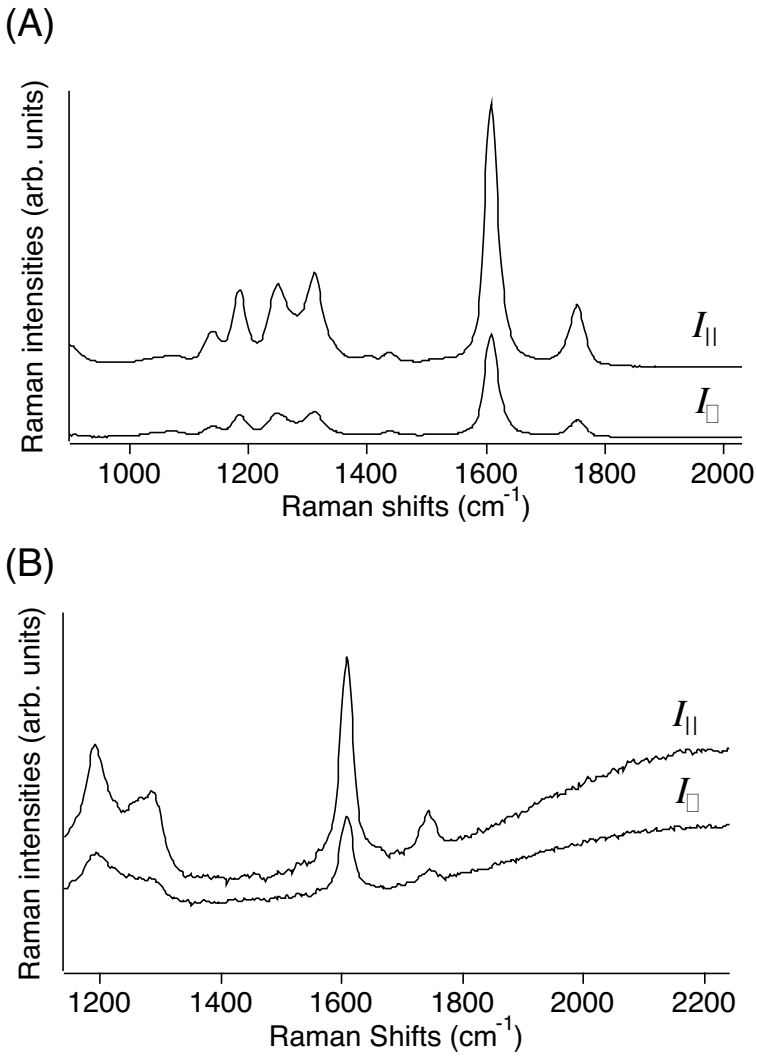

Figure 5.2: Polarized Raman spectra in isotropic phase; (A) compound (a) at 50 °C and (B) Mitsui mixture at 110 °C.

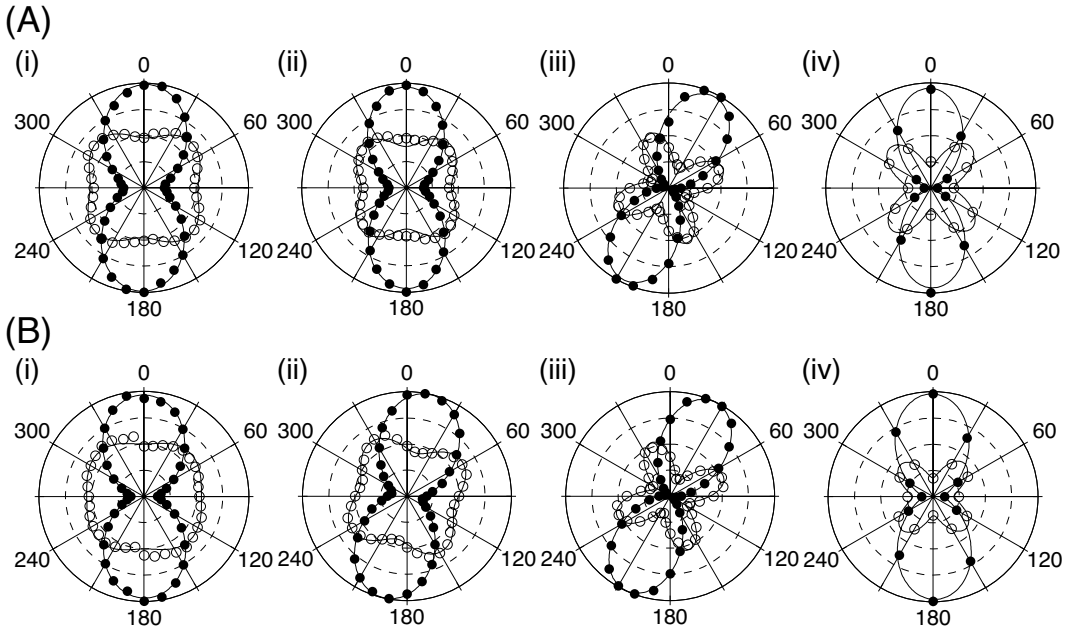

Figure 5.3: Polar plots of polarized Raman scattering intensity (in arbitrary units) vs polarization direction of incident laser light (in degree) for the phenyl line. (A) Compound (a) in antiferroelectric phase at 26 °C under statically applied electric fields of (i) $E = 0$ V, (ii) $E = 2.3$ V/μm, (iii) $E = 4.6$ V/μm, and (iv) at the tip of the V under dynamically applied electric field, (B) Mitsui mixture in antiferroelectric phase at 40 °C under statically applied electric fields of (i) $E = 0$ V, (ii) $E = 1.8$ V/μm, (iii) $E = 5.6$ V/μm, and (iv) at the tip of the V under dynamically applied electric field. Closed and open circles represent $I_{\parallel,\mathrm{meas}}(\omega')$ and $I_{\perp,\mathrm{meas}}(\omega')$, respectively. The relative intensity of $I_{\perp,\mathrm{meas}}(\omega')$ is enlarged by twice as compared to that of $I_{\parallel,\mathrm{meas}}(\omega')$. Solid lines show the best-fitting results of Eqs. (2.60) and (2.70) with $\langle P_2(\cos\beta)\rangle_{\mathrm{app}}$ and $\langle P_4(\cos\beta)\rangle_{\mathrm{app}}$ given in Table 5.1.

Table 5.1: Obtained apparent orientational order parameters; (A) compound (a) at 26°C and (B) Mitsui mixture at 40°C.

(A) compound (a)		
field (V/μm)	$\langle P_2(\cos\beta)\rangle_{\rm app}$	$\langle P_4(\cos\beta)\rangle_{\rm app}$
0 (dc)	0.40 ± 0.01	-0.02 ± 0.01
2.3 (dc)	0.45 ± 0.01	0.04 ± 0.02
4.6 (dc)	0.78 ± 0.02	0.47 ± 0.04
0 (1 Hz)	0.70 ± 0.03	0.35 ± 0.05

(B) Mitsui mixture		
0 (dc)	0.45 ± 0.01	-0.11 ± 0.01
1.8 (dc)	0.46 ± 0.01	-0.02 ± 0.01
5.6 (dc)	0.78 ± 0.01	0.48 ± 0.02
0 (1 Hz)	0.58 ± 0.03	0.20 ± 0.04

$\Delta n_0 = 0.15$ are used in the analysis. The maximum position points to the layer normal at $E = 0$ [Fig. 5.3(A), (i)], because the numbers of layers tilting to the right and to the left are identical in the antiferroelectric phase and their tilt angles are canceled out in the macroscopic average. The orientational order parameters are considerably small. When the dc field below 3.5 V/μm, which is the threshold field from antiferroelectric to ferroelectric state, is applied, the maximum position of $I_{\parallel,\rm meas}$ scarcely tilts from the layer normal [Fig. 5.3(A), (ii)] but the order parameters slightly increases. This means that the local in-plane directors rotate without destroying the antiferroelectric anticlinic structure. [84,85]. When the electric field above the threshold is applied, the maximum position of $I_{\parallel,\rm meas}$ tilts by 28.5° from the smectic layer normal [Fig. 5.3(A), (iii).] The large order parameters reflect that all the local in-plane directors are oriented in one direction parallel to the substrate plates. These changes clearly indicate the tristable

switching.

The V-shaped switching observed by applying an electric field of triangular waveform at 1 Hz is shown in Fig. 5.4(A), where the transmittance of light is plotted against the applied electric field. The transmittance is saturated at about 2.5 V/μm. The polarized Raman scattering was measured at the tip of the V. The intensities are plotted against the rotation angle of the sample cell in Fig. 5.3(A) [(iv)] as a polar plot. The molecules are oriented parallel to the layer normal as is clear in the profile of $I_{\parallel,\mathrm{meas}}$. The orientational order parameters are given in Table 5.1.

5.3.2 Mitsui mixture

The Mitsui mixture shows the V-shaped switching when a dc electric field is applied. Any macroscopic domains are not generated in this switching process. Only the extinction direction changes continuously with increasing the applied electric field.

Figures 5.3(B)[(i)–(iii)] are polar plots of the polarized Raman scattering intensities in the Mitsui mixsture under dc electric fields at 40°C. Table 5.1(B) summarizes the corresponding apparent order parameters. This material shows an antiferroelectric phase in the free-standing film at this temperature. At $E = 0$, the maximum position of $I_{\parallel,\mathrm{meas}}$ points to the layer normal [Fig. 5.3(B), (i)] and hence the apparent tilt angle is zero. The small order parameters indicates that the surface-stabilized state is realized as in compound (a). With an increase in the applied electric field, the apparent molecular tilt angle becomes larger continuously. No threshold is observed and the transmittance shows the V-shaped switching. At $E = 1.8$ V/μm, the maximum position of $I_{\parallel,\mathrm{meas}}$ tilts from the layer normal by 14° [Fig. 5.3(B), (ii)] but the order parameters, $\langle P_2(\cos\beta)\rangle_{\mathrm{app}}$ and $\langle P_4(\cos\beta)\rangle_{\mathrm{app}}$, increase only slightly as given in Table 5.1(B). The transmittance is saturated at about 4 V/μm, where the ferroelectric state is attained. The maximum position of $I_{\parallel,\mathrm{meas}}$ tilts from the layer normal by 26.3° at $E = 5.6$ V/μm [Fig. 5.3(B), (iii).]

Figure 5.4(B) shows the V-shaped switching in the Mitsui mixture at 40°C when the electric field of triangular waveform is applied at 1 Hz. The transmittance saturates at about 4 V/μm as in the case of applying an dc electric field mentioned above. The

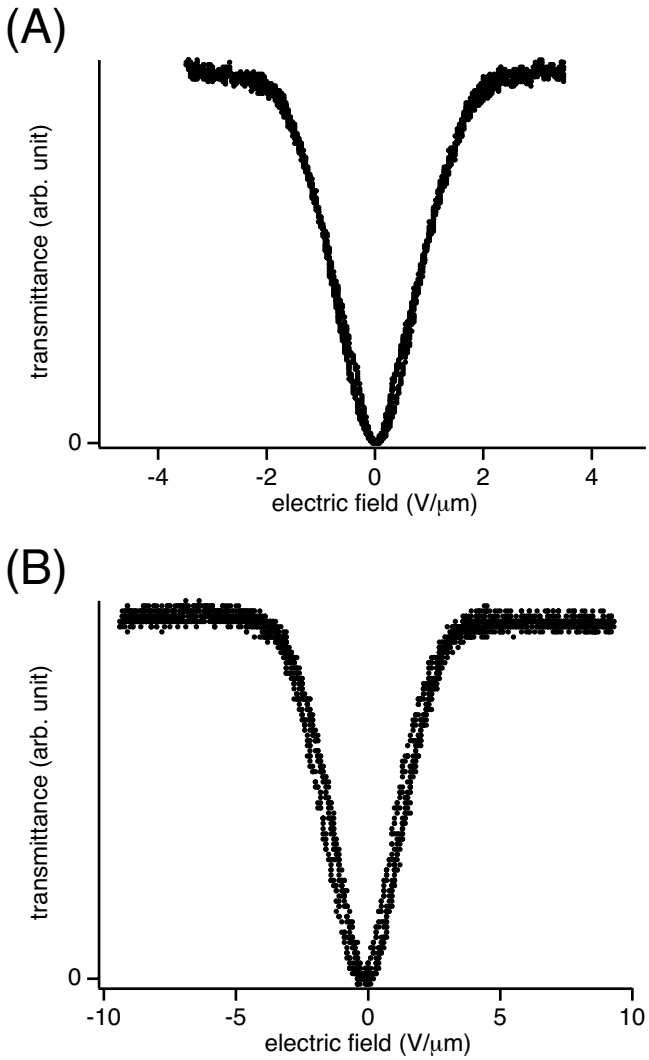

Figure 5.4: Optical response under the crossed Nicol configuration when the polarization direction of the incident laser light is parallel to the layer normal; (A) compound (a) at 26°C and (B) Mitsui mixture at 40°C. Transmittance of light is plotted against the applied field.

polarized Raman scattering intensity measured at the tip of the V-shaped switching is shown in Fig. 5.3(B), [(iv)]. This profile indicates that the molecular distribution center axis is parallel to the layer normal. The fitting procedures described in Chapter 2 give the apparent order parameters [Table 5.1(B).] $n_g = 1.46$, $n_X = 1.5$, and $\Delta n \equiv n_Z - n_X = \Delta n_0 \langle P_2(\cos\beta)\rangle$ with $\Delta n_0 = 0.15$ are also used in the analysis.

5.4 Model calculation

To elucidate the alignment change of local in-plane directors in the switching process by polarized Raman scattering, first some typical distributions of local in-plane directors are presupposed, their apparent order parameters, $\langle P_2(\cos\beta)\rangle_{\rm app}$ and $\langle P_4(\cos\beta)\rangle_{\rm app}$, are calculated, and the experimentally obtained apparent order parameters are compared with the calculated results. It is first assumed that the smectic layer structure is not chevron but bookshelf for the sake of simplicity. The geometry is drawn in the Fig. 5.5(a). The chevron structure complicates the calculations but its influence on the simulated results is relatively small as will be shown later. The following three typical distributions of local in-plane directors were assumed:

$$f_d(\phi,\theta,\chi) = \frac{1}{4\pi\sqrt{2\pi}\sigma_d}\exp\left[-\frac{(\phi-\pi/2)^2}{2\sigma_d^2}\right]\delta(\theta-\Theta), \quad \text{type 1} \tag{5.1}$$

$$f_d(\phi,\theta,\chi) = \frac{1}{8\pi\sqrt{2\pi}\sigma_d}\left\{\exp\left(-\frac{\phi^2}{2\sigma_d^2}\right)+\exp\left[-\frac{(\phi-\pi)^2}{2\sigma_d^2}\right]\right\}\delta(\theta-\Theta), \quad \text{type 2} \tag{5.2}$$

and

$$f_d(\phi,\theta,\chi) = \delta(\theta-\Theta)/(8\pi^2), \quad \text{type 3.} \tag{5.3}$$

Here ϕ, θ, and χ are the Euler angles in the right-handed smectic layer frame. ϕ shows the azimuthal angle of the local in-plane director and $\phi = 0$ corresponds to the X_l axis. The Z_l axis is along the smectic layer normal and the Y_l axis is perpendicular to the substrate plates [86]. The Y_l and Y axes are taken to coincide each other. Type 1 is motivated by SmC^* in the Inui mixture [23, 55–57], type 2 by surface-stabilized SmC_A^* [84], and type 3 by the random model [43, 50, 51, 53]. These three models have symmetry axes parallel to the layer normal.

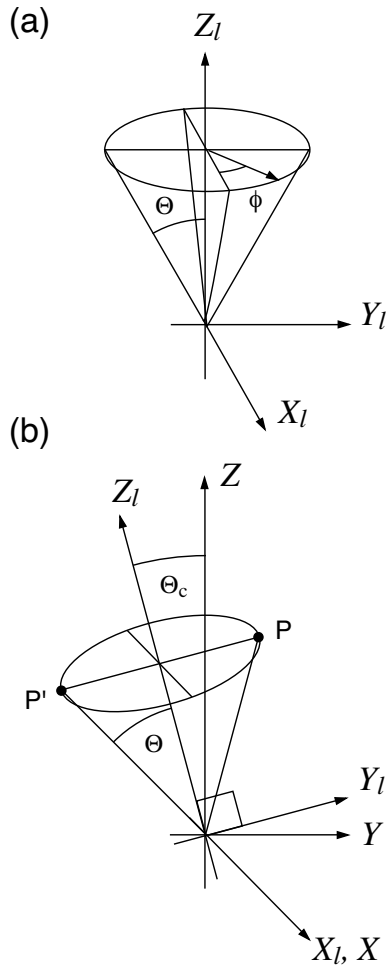

Figure 5.5: Geometry with (a) bookshelf layer structure and (b) the chevron layer structure.

Since only the second- and forth- order terms contribute to the Raman scattering process, the molecular orientational distribution function in the $X_E Y_E Z_E$ molecular orientation frame is well approximated by

$$f_{\mathrm{mol,E}}(\alpha,\beta,\gamma) = \sum_{L=0,2,4} \frac{2L+1}{8\pi^2} \langle P_L(\cos\beta)\rangle_E P_L(\cos\beta). \tag{5.4}$$

Here α, β, and γ are the Euler angles in the molecular orientation frame, $\langle P_2(\cos\beta)\rangle_E$ and $\langle P_4(\cos\beta)\rangle_E$ are the apparent second- and fourth- order parameters experimentally obtained in the electric-field-induced ferroelectric SmC^* state, which result principally from molecular level fluctuations and slightly from the imperfect alignment of the smectic layers as manifested by textures. In the $X_l Y_l Z_l$ smectic layer frame, Eq. (5.4) can be written as [11]

$$\begin{aligned} f_{\mathrm{mol,E}}(\phi,\theta,\chi) &= \tilde{R}(0,\Theta,0) f_{\mathrm{mol,E}}(\alpha,\beta,\gamma) \\ &= \frac{1}{8\pi^2} \sum_{L=0,2,4} \sum_{m=-L}^{L} \langle P_L(\cos\beta)\rangle_E \\ &\quad \times D^{(L)}_{m0}(0,\Theta,0) D^{(L)*}_{m0}(\phi,\theta,\chi), \end{aligned} \tag{5.5}$$

where $D^{(L)}_{m0}(0,\Theta,0)$ is a rotation matrix, and $\tilde{R}(0,\Theta,0)$ is the rotation operator that transforms the $X_E Y_E Z_E$ to $X_l Y_l Z_l$-coordinate frames. Convoluting the molecular fluctuation given by Eq. (5.5) with one of the in-plane director distribution given by Eqs. (5.1)–(5.3), the molecular orientational distribution function f_{mol} is obtained by

$$\begin{aligned} f_{\mathrm{mol}}(\phi,\theta,\chi) &= \int_0^{2\pi}\int_0^{\pi}\int_0^{2\pi} f_d(\phi',\theta',\chi') \\ &\quad \times f_{\mathrm{mol,E}}(\phi-\phi',\theta-\theta',\chi-\chi') d\phi' \sin\theta' d\theta' d\chi'. \end{aligned} \tag{5.6}$$

Inserting Eqs. (5.4) and (5.5) into Eq. (5.6), we obtain the apparent molecular orientational Lth (L=2 and 4) order parameters

$$\langle P_L(\cos\beta)\rangle_{\mathrm{app}} = \sum_{m=-L}^{L} \langle D^{(L)*}_{m0}(\phi,\theta,\chi)\rangle, \tag{5.7}$$

with

$$\begin{aligned} \langle D^{(L)*}_{m0}(\phi,\theta,\chi)\rangle &= \int_0^{2\pi}\int_0^{\pi}\int_0^{2\pi} D^{(L)*}_{m0}(\phi,\theta,\chi) \\ &\quad \times f_{\mathrm{mol}}(\phi,\theta,\chi) d\phi \sin\theta d\theta d\chi. \end{aligned} \tag{5.8}$$

Table 5.2: Simulated orientational order parameters of compound (a) for the bookshelf layer structure. The molecular tilt angles used for simulations were 28.5° at 26°C and 24.7° at 32°C, which were determined experimentally by applying dc electric field above the saturation value.

		26°C		32°C	
	σ_d (°)	$\langle P_2(\cos\beta)\rangle_{\rm app}$	$\langle P_4(\cos\beta)\rangle_{\rm app}$	$\langle P_2(\cos\beta)\rangle_{\rm app}$	$\langle P_4(\cos\beta)\rangle_{\rm app}$
Type 1	0	0.70	0.38	0.64	0.30
	10	0.68	0.35	0.63	0.29
	20	0.65	0.28	0.61	0.25
Type 2	0	0.38	−0.14	0.42	−0.03
	30	0.42	−0.08	0.46	0.02
Type 3	–	0.50	0.04	0.51	0.09

The results of the model calculation for compound (a) is listed in Table 5.2. The orientational order parameters experimentally obtained at 26°C with no applied electric field are well reproduced by the result of the type 2 model with a small σ_d. Moreover, the compound (a) exhibits the tristable switching under statically applied electric field, as mentioned before. These results suggest that the usual surface-stabilized anticlinic molecular alignment without helical structure is formed. The orientational order parameters at the tip of the V are well described by the result of the type 1 with a very small σ_d. The $\langle P_2(\cos\beta)\rangle_{\rm app}$ of 0.63±0.03 and $\langle P_4(\cos\beta)\rangle_{\rm app}$ of 0.27±0.05 were also obtained, respectively, at the tip of the V at 32°C in the ferrielectric phase. These orientational order parameters also coincide with the result of the type 1 with a very small σ_d. Hence, for the compound (a), the small distribution at the tip of the V suggests collective rotation of the local in-plane director.

Table 5.3 summarizes the results of the model calculation for the Mitsui mixture. At 40 °C with no dc field, the orientational order parameters agree with the results given by type 2 with $\sigma_d = 0°$. This result suggests the surface-stabilized molecular alignment. However, the V-shaped switching in the firstrun indicates that the state is

Table 5.3: Simulated orientational order parameters of Mitsui mixture for the bookshelf layer structure. The molecular tilt angles used for simulations were 26.3° at 40°C and 22.8° at 60°C, which were determined experimentally by applying dc electric field above the saturation value.

		40°C		60°C	
	σ_d (°)	$\langle P_2(\cos\beta)\rangle_{\rm app}$	$\langle P_4(\cos\beta)\rangle_{\rm app}$	$\langle P_2(\cos\beta)\rangle_{\rm app}$	$\langle P_4(\cos\beta)\rangle_{\rm app}$
Type 1	0	0.74	0.41	0.74	0.42
	30	0.65	0.25	0.68	0.30
	60	0.57	0.12	0.61	0.19
Type 2	0	0.43	−0.10	0.50	−0.01
	30	0.48	−0.03	0.54	0.06
Type 3	–	0.55	0.09	0.60	0.16

not the usual antiferroelectric, anticlinic molecular alignment. The orientational order parameters at the tip of the V are described by the type 3 or the type 1 with a large σ_d. The orientational order parameters were also obtained at 60°C, where the phase was ferroelectric in a free-standing film. $\langle P_2(\cos\beta)\rangle_{\rm app}$ of 0.60±0.03 and $\langle P_4(\cos\beta)\rangle_{\rm app}$ of 0.12±0.05 were obtained, respectively, at the tip of the V. These values were well described by the type 3 (Table 5.3). Consequently, the molecular orientation of the Mitsui mixture at the tip of the V is characterized by the considerable large distribution of the local in-plane directors.

When the chevron structure was considered, Eq. (5.5) should be modified. The geometry with the chevron layer structure is drawn in Fig. 5.5(b). The Z_l axis, which represents the smectic layer normal, is inclined at Θ_c from Z_c axis which is parallel to the substrate plane. The X_c, Y_c, and Z_c axes constitute the right-handed Cartesian coordinate frame. The X_c axis is identical with the X_l axis. When the model of the type 1 with $\sigma_d = 0$ is applied to the tip of the V, the local in-plane director has two choice of either point, P or P', which are not identical now. It is reasonable to select P with the smaller inclined angle with respect to the substrate plane. The molecular

Table 5.4: Simulated orientational order parameters of compound (a) for the chevron layer structure. The chevron angle was assumed at 15°. The other parameters were identical with Table 5.2

		26°C		32°C	
	σ_d (°)	$\langle P_2(\cos\beta)\rangle_{\rm app}$	$\langle P_4(\cos\beta)\rangle_{\rm app}$	$\langle P_2(\cos\beta)\rangle_{\rm app}$	$\langle P_4(\cos\beta)\rangle_{\rm app}$
Type 1	0	0.74	0.45	0.68	0.35
Type 2	0	0.37	−0.12	0.41	−0.03
Type 3	–	0.49	0.04	0.49	0.09

distribution function was given by

$$f_c(\phi_c, \theta_c, \chi_c) = \tilde{R}(-\pi/2, \Theta_c, 0) f_{\rm mol}(\phi, \theta, \chi), \tag{5.9}$$

where $\tilde{R}(-\pi/2, \Theta_c, 0)$ is the rotation operator that transforms the $X_l Y_l Z_l$ to the $X_c Y_c Z_c$-coordinate frames. In the models of type 2 and 3, the center axis of the molecular orientational distribution, which is parallel to the layer normal, is inclined at Θ_c with respect to the substrate plane. Thus, the apparent orientational order parameters were calculated by considering the chevron layer structure in Eqs. (5.1)–(5.9). Tables 5.4 and 5.5 show the results of the model calculation that takes into consideration the chevron structure for the compound (a) and the Mitsui mixture, respectively. The chevron angle of 15° was assumed because the angle was up to 12° [55]. $\langle P_L(\cos\beta)\rangle_E$ used for this calculation were identical with those used in the calculation with the bookshelf structure because the sufficiently high electric field induces the deformation to the bookshelf structure from the chevron structure [70]. The results showed that the chevron structure does not affect the essential understandings of the molecular distribution at the tip of the V.

Let us consider the polarization-stabilized twisted SmC^* structure proposed by Rudquist *et al.* [56]. The bookshelf structure is also presumed here. The spatial distribution of the local in-plane director along the Y_l axis can be divided into three parts, that is, the bulk of uniform orientation structure with high coherence at $\phi = \pi/2$ in the middle of the cell and the upper and lower thin surface regions with twisted

Table 5.5: Simulated orientational order parameters of Mitsui mixture for the chevron layer structure. The chevron angle was assumed at 15°. The other parameters were identical with Table 5.3

		40°C		60°C	
	σ_d (°)	$\langle P_2(\cos\beta)\rangle_{\rm app}$	$\langle P_4(\cos\beta)\rangle_{\rm app}$	$\langle P_2(\cos\beta)\rangle_{\rm app}$	$\langle P_4(\cos\beta)\rangle_{\rm app}$
Type 1	0	0.77	0.47	0.77	0.46
Type 2	0	0.42	−0.09	0.49	−0.01
Type 3	–	0.54	0.08	0.59	0.15

structure. As we go from one substrate to the other of the liquid crystal sample cell, ϕ increases from zero at one substrate to $\pi/2$ at the interface between the surface and bulk regions, keeps $\pi/2$ in the bulk region, and increases again from $\pi/2$ to π at the other substrate. When the joined two surface regions are supposed to be one uniform twisted structure, the distribution of the local in-plane director is given by the same function as Eq. (5.3) provided the distribution along the Y_l axis instead of the Z_l axis is considered. The distribution in the bulk region is represented by Eq. (5.1) with $\sigma_d = 0$. The averaged distribution of the local in-plane director depends on the ratio of the surface regions in the entire space. The highest value of the apparent orientational order parameter is given in the entire bulk region of the sample cell (type 1 with σ_d in Table 5.2 and 5.3), and the lowest value in the entire surface regions (type 3 in Table 5.2 and 5.3.) This means that the apparent orientational order parameter decreases with an increase of the ratio of the surface regions to the bulk region, and vice versa. The orientational order parameters of the compound (a) at the tip of the V are well described by the type 1. This indicates that the surface regions must be sufficiently thin. On the other hand, in the case of the Mitsui mixture, the low order parameters at the tip of the V can be described by the type 3. This suggests that the surface regions have very large space in the sample cell. However, the twisted structure that extends throughout the cell does not give a dark state. The thickness of the surface regions must be less than the wavelength of the visible light for obtaining the dark

state at the tip of the V. Therefore, the polarization-stabilized twisted SmC^* structure is inappropriate for the Mitsui mixture.

5.5 Discussion

In this way, the V-shaped switching is observed in both extremes of local in-plane director distributions at the tip of the V. One is considerably concentrated at a particular direction or two equivalent ones parallel to a plane perpendicular to the substrate plates, and the other is quite broadly distributed around the smectic layer normal. The former is described by Eq. (5.1) with a very small σ_d and the latter by Eq. (5.3). Two independent mechanisms may be possible to cause the two types of the V-shaped switching, which look apparently the same. However, both the compound (a) and the Mitsui mixture here investigated belong to a group of materials developed under the guiding principle of frustrating ferroelectricity and antiferroelectricity. These materials are closely related to the prototyped antiferroelectric liquid crystals, MHPOBC and TFMHPOBC, and have the quite similar molecular structures around the chiral centers. Moreover, our preliminary studies indicate that there exist some materials in which the distribution of the in-plane directors at the tip of the V is given by Eq. (5.1) with a large standard deviation σ_d [106]. Any distribution between both the extremes appears to be realized by an actual material. Consequently, it is natural to attribute a common cause for the V-shaped switching under consideration. When the director distribution is really concentrated, the charge stabilization and/or the highly collective azimuthal angle rotation of the local in-plane directors on the SmC^* tilt cone in a macroscopic scale can meet the spatial uniformity during the V-shaped switching [23,54–57]. In the switching process from the electric-field-induced ferroelectric state to the one at the tip of the V, however, the highly collective azimuthal angle rotation in a macroscopic scale could hardly explain the spatial uniformity. It is general to anticipate domain formations due to the spatial irregularity on the substrate interfaces in the critical electric field at which the switching starts to occur. The same explanation does not hold for the quite broad distribution as in the Mitsui mixture, either.

Since the electric-field-induced continuous rotation of a spatially uniform optic axis

characterizes the switching, the spatial non-uniformity of local in-plane directors must be restricted within regions smaller than the visible wavelength scale. What is essential to the V-shaped switching under consideration is the easy formation of invisible microdomains in case of need. This must be assured by the extreme softness with respect to the tilting directions and sense that results from the frustration between ferroelectricity and antiferroelectricity. This softness is also indicated by the phenomena of the phase destruction in a thin cell of the Mitsui mixture and of the very slow recovery from the state (alignment) dynamically realized at the tip of the V to the stable one at zero field in compound **a**. An open question is whether the dynamic state is ferroelectric or not [56, 73, 81]? In previous papers, it was reported that the higher temperature phase above the antiferroelectric one is ferrielectric in compound **a** and the Inui mixture [51, 52]. However, recent studies [106, 107] indicate that it is peculiar ferroelectric SmC^*. Because of the biaxial anchoring on polyimide aligning films, the so-called surface stabilized states becomes destabilized and the total anchoring energy of molecules on the SmC^* tilt cone is almost independent of the azimuthal angle. Hence the relatively weak in-plane anchoring must force the molecules to align along the rubbing direction. In addition, the distribution around the rubbing direction may become broad when the twisting power is large. The biaxial anchoring of substrate interfaces destroy the antiferroelectric order and produce the broadly distributed alignment at zero dc field in the Mitsui mixture, which is clearly different from ordinary helical SmC^* because no Goldstone mode is observed. The alignment at the tip of the V, also broadly distributed and almost described by Eq. (5.3), may be much closer to ordinary helical SmC^*; the Goldstone mode may be observed by dynamically measuring the dielectric constant at the tip of the V [56]. The details of evolution from antiferroelectric to ferroelectric are future problems to be studied.

Now, let us consider that the frustration between ferroelectricity and antiferroelectricity from a viewpoint of the free energy that is related with the interaction between the adjacent layers. Considering the symmetry of the phase, the averaged interlayer interaction can be represented in the following form with taking the first two Fourier components [65, 83].

$$v(\Delta\phi) = v_1 \cos\Delta\phi - v_2 \cos 2\Delta\phi, \tag{5.10}$$

where $\Delta\phi$ is an azimuthal angle difference between the local in-plane directors of adjacent layers; $\Delta\phi = 0$ and $\Delta\phi = \pi$ represent the synclinic and the anticlinic orderings, respectively. A small deviation due to the helicity is ignored. Positive v_1 promotes the anticlinic ordering while v_2 represents the energy barrier between synclinic and anticlinic ordering. The distribution of the local in-plane directors critically depends on the barrier v_2. The small v_1 and relatively large v_2 compared with the thermal agitation give a long relaxation time from synclinic to anticlinic ordering. Therefore, the synclinic ordering is conserved under periodically applied electric field at an appropriate frequency for the V-shaped switching. The electric-field-induced ferroelectric state, which is characterized with a small distribution of the in-plane directors, may rotate almost collectively because the total anchoring energy on the SmC^* tilt cone is nearly independent of the azimuthal angle [23, 54–57, 95, 103, 104, 106, 107]. This is actually observed in compound (a). When v_2 is sufficiently small so that the substrate interfaces destroy the anticlinic, antiferroelectric structure [101, 106, 107], the thresholdless switching occurs even in the first run as actually observed in the Mitsui mixture. Moreover, the spatial irregularity on the substrate interfaces, together with the strong twisting power, may promote the large distribution of ϕ during the V-shaped switching. This type of the switching corresponds to the Mitsui mixture.

Actually, the Mitsui mixture is on the subtle balance between the ferroelectricity and antiferroelectricity. In the mixture of compounds (d) and (e), the electro-optic response is really depend on the mixing ratio. Seomun *et al.* [51,100] studied the system in detail, obtaining the temperature mixing ratio phase diagram in thick free-standing films and the corresponding diagram in thin homogeneous cells. At the concentration of 63:37, only one liquid crystal phase other than SmA is distinguished in the latter, while five tilted phases are observed in the former. Substrate interfaces destroy the phase structures. Readiness of destruction critically depends on the concentration. In a 70:30 mixture, an antiferroelectric phase is stable not only in thick films but also in thin cells; the threshold is clearly seen in the first run of the switching, although some thresholdless switching is achieved dynamically. In the 63:37 mixture, however, no antiferroelectric phase stably exists in thin cells because the threshold does not emerge even in the first run, although it does in thick films. The destruction is also

seen as a considerable difference in the temperature dependence of dielectric constants between a 66:34 mixture and the 63:37 mixture. The relative permittivity becomes smaller, the phase transition disappears, and a single phase or state prevails. The state is neither ferroelectric nor antiferroelectric; no helical structure exists, either. These facts support the above discussion for the Mitsui mixture.

Here, the Langevin-type reorientation, which is applicable to the random model [43, 50–53], the effective internal field model [99], and the cluster model [101, 102] for the Mitsui mixture, is presupposed. Because of the smectic layered structure, the correlation length of local in-plane directors along the layer normal is the order of layer spacing, $\xi_{\parallel} \approx d$, and the one in a single layer, $\xi_{\perp}$, is very long. Tilting randomization among smectic layers assures the disappearance of net spontaneous polarization, but an applied electric field induces it according to the Langevin-like in-plane director reorientation. The aligning process is described as

$$\langle \cos\Phi \rangle = \frac{\int_0^{\pi} \exp(x\cos\Phi)\cos\Phi d\Phi}{\int_0^{\pi} \exp(x\cos\Phi) d\Phi} \tag{5.11}$$

by using a ratio of electric aligning energy, $P_{\rm eff}E$, to thermal agitating energy, $kT_{\rm eff}$,

$$x = P_{\rm eff}E/(kT_{\rm eff}). \tag{5.12}$$

The effective dipole moment $P_{\rm eff}$ is given by

$$P_{\rm eff} = d(\xi_{\perp})^2 P_{\rm s}, \tag{5.13}$$

where $P_{\rm s}$ is a net spontaneous polarization observed in Sm-C^*. The thermal agitating energy should also be regarded as an effective one, since constraints imposed by substrate interfaces play an important role. Numerical calculation indicates that the degree of alignment $\langle \cos\Phi \rangle = 0.9$ attains at $x = 5$. For the sake of simplicity, let us consider that ferroelectric SmC^* is realized at $x = 5$. By inserting the experimentally obtained saturation field $E = |E_{\rm s}|$ =2 V μm^{-1} and appropriately presumed $kT_{\rm eff} = 1/40$ eV $= 1.6\times10^{-19}/40$ C V into Eq. (5), we obtain $P_{\rm eff} = 1 \times 10^{-26}$ C m. By further inserting measured $P_{\rm s} = 0.5$ mC m^{-2} and $d = 3.5 \times 10^{-9}$ m in Eq. (6), we can evaluate $\xi_{\perp} = 7.5 \times 10^{-8}$ m = 75 nm. Since the correlation length is much shorter

than the visible light wavelength, the switching process in the Mitsui mixture looks like uniform.

5.6 Conclusions

Polarized Raman scattering technique is very useful for the evaluation of orientational molecular distribution in liquid crystal systems. The orientational order parameters were investigated for two types of liquid crystals showing the V-shaped switching, compound (a) and Mitsui mixture. The results showed two extreme distributions of the local in-plane director at the tip of the V. The compound (a) exhibited a small distribution, while the Mitsui mixture exhibited a large distribution. The small distribution of the local in-plane directors for the compound (a) suggests the collective azimuthal angle rotation in the V-shaped switching process. However, the same explanation does not hold for the Mitsui mixture with quite large distribution of the local in-plane directors at the tip of the V. What is essential to the V-shaped switching is the easy formation of invisible microdomains in case of need. This required the softness with respect to the tilting directions and sense that results from the frustration between ferroelectricity and antiferroelectricity. The difference in the distribution of two types of liquid crystals at the tip of the V was explained by the barrier between synclinic and anticlinic ordering in adjacent layers. The small barrier gave a large distribution at the tip of the V in the dynamic switching, consequently triggered the V-shaped switching even in the firstrun. On the other hand, the large barrier did a small distribution and the tristable switching.

Chapter 6

Summary

Polarized Raman scattering measurement is powerful tool to evaluate the molecular orientational distribution. I investigated the molecular orientational distribution of the liquid crystals showing ferro-, ferri-, and antiferroelectricities by polarized Raman scattering measurements for some phenomena concerning the anisotropic interlayer molecular interactions. The basic concept of the this thesis is described in Chapter 1 and the procedure how the second- and forth-order orientational order parameters are obtained from the polarized Raman intensities is described in Chapter 2.

In Chapter 3, the orientational ordering of MHPOBC was investigated for the successive SmC^* and its variant phases. An improved equation for the analysis of the polarized Raman intensity was derived as a function of polarization direction of incident laser light and the orientational order parameters. Even in the chiral smectic phases, the apparent orientational order parameters, $\langle P_2(\cos\beta')\rangle$ and $\langle P_4(\cos\beta')\rangle$, could be defined by the proper corrections for the smectic layer structure and an optical disturbance. The orientational order parameters were evaluated for three Raman lines which were attributed to the phenyl ring stretching mode of three benzene rings at the core part of the molecule, the core C=O stretching mode of the carbonyl group at the central part of the molecule, and the chiral C=O stretching mode of the carbonyl group at the chiral part of the molecule. An unusual change of the orientational order parameters was observed with decrease of temperature. The irregularity was outstanding in $\langle P_4(\cos\beta')\rangle$. $\langle P_4(\cos\beta')\rangle$ exhibited drastic variation as temperature was decreased, that

is, it smoothly increased in SmA phase, scattered in SmC_α*, SmC*, SmC_γ* phases, and dropped in SmC_A phase. Moreover, $\langle P_4(\cos\beta')\rangle$ of the phenyl line and the chiral CO line exchanged their order with each other in SmC_A* phase. It was concluded that this irregular variation of the order parameter stemmed from the biaxiality of the molecular orientational distribution, which was attributed to the hindrance of molecular rotation on its long axis. This result suggests that the growth of a degree of the hindrance as the temperature decreases is closely related to the appearance and the transitions of the phases because the hindered molecular rotation increases the interlayer molecular interactions.

In Chapter 4, the molecular orientational ordering of an antiferroelectric liquid crystal was studied for the homogeneously aligned thin sample with applying static electric field. The apparent orientational order parameters gradually increased with the applied electric field strength in the pretransitional regime from antiferro- to ferroelectric phase although the averaged molecular orientation was hardly changed. This change of the order parameters shows the molecular reorientation with holding the antiferroelectric anticlinic molecular ordering. The molecular reorientation is represented by a similar equation describing the nematic director deformation induced by an external electric field. The deformation is characterized by the electric coherence length which depends on the elastic constant of the liquid crystal, spontaneous polarization, electric field strength, and interlayer interaction. The estimated electric coherence length was much larger than the theoretical prediction. This suggests the necessities of the more precise theoretical description of the interlayer interaction and the dependence of the effective spontaneous polarization on the phase.

In Chapter 5, the molecular orientational order parameters were obtained in two types of ferro- and antiferroelectric liquid crystal materials showing the thresholdless, hysteresis free, V-shaped switching in thin homogeneous cells. One is the Mitsui mixture and the other is one component of the Inui mixture [compound (a)]. They showed a difference in the stability of the antiferroelectric phase in thin homogeneous cells. In the antiferroelectric phase, the Mitsui mixture exhibited the V-shaped switching induced by both the ac and dc electric field while the compound (a) exhibited the V-shaped switching induced by only the ac electric field but the tristable switching

by the dc electric field. The obtained distribution of the $\boldsymbol{c}$-director at the tip of the V was considerably broad in the Mitsui mixture, while it is narrow in the compound (a). These differences have been explained, mainly, by the barrier between the ferroelectric synclinic and antiferroelectric anticlinic orderings. The considerably small barrier for the Mitsui mixture introduces the low stability of the antiferroelectric anticlinic molecular ordering, so that, the alignment layer surface can easily destroy the anticlinic molecular ordering and induce the randomization of the $\boldsymbol{c}$-director at the tip of the V. Hence, the V-shaped switching is observed even under the dc electric field. Meanwhile, the barrier for the compound (a) is relatively large to hold the synclinic molecular ordering during the switching once the field-induced ferroelectric phase is obtained. However, when the alignment layer surface disturbs the uniform molecular reorientation in the switching, the formation of the invisible maicrodomain is need. Therefore, the V-shaped switching still requires the small anisotropy in the interlayer interaction with respect to the c-director orientations that results from the frustration between ferroelectricity and antiferroelectricity.

Hindered molecular rotation on its long axis increases interlayer molecular interactions. The interlayer molecular interactions cause the ferroelectric synclinic and antiferroelectric anticlinic molecular orderings. The frustration and the competition between the synclinic and anticlinic molecular orderings bring about many interesting phenomena in the ferro-, ferri-, and antiferroelectric smectic phases; e.g., the curious structure of SmC_α* phase and its dependence on the temperature, the successive transition between the SmC variant phases, the process of domain generation and its growth in a field-induced phase transition, the pretransitional phenomenon, and so on. I am sure that the results obtained in this thesis give us clues to the physical description of the above phenomena with the interlayer molecular interactions.

Acknowledgments

I am very thankful to Professor Tatsuhisa Kato for the accomplishment of the studies in this thesis. I would like to express my deep gratitude to Professor Atsuo Fukuda for fruitful discussions, suggestions, and comments about the ferro-, antiferro-, and ferri-electricity of smectic liquid crystals through the collaboration. I am most grateful to Professor Yukio Ouchi of Nagoya University for supplying MHPOBC material and preparing the sample cell. I would like to thank Mitsui Chemicals, Inc., Chisso corporation, and Nissan Chemical Industries, Ltd. for supplying the liquid crystal and aligning polyimide samples used in experiments. I appreciate for bounties by Mitsuo Ito (1994-1998) and Koji Kaya (1999-2001), the director-general of the IMS. I thank the technicians helping me to make the machinery used in the experiments in this thesis.

Bibliography

[1] F. Reinitzer, Monatsch Chem. **9**, 421 (1888).

[2] O. Lehmann, Z. Physikal. Chem. **4**, 462 (1889).

[3] G. Friedel, Ann. Phys. **18**, 273 (1922).

[4] Y. Takanishi *et al.*, Jpn. J. Appl. Phys., Part 1 **30**, 2023 (1991).

[5] A. Suzuki *et al.*, Jpn. J. Appl. Phys., Part 2 **29**, L336 (1990).

[6] Y. Ouchi *et al.*, Jpn. J. Appl. Phys., Part 2 **27**, L725 (1988).

[7] T. P. Rieker *et al.*, Phys. Rev. Lett. **59**, 2658 (1987).

[8] Y. Takanishi, Y. Ouchi, H. Takezoe, and A. Fukuda, Jpn. J. Appl. Phys., Part 2 **28**, L487 (1989).

[9] Y. Ouchi, Y. Takanishi, H. Takezoe, and A. Fukuda, Jpn. J. Appl. Phys., Part 1 **28**, 2547 (1989).

[10] S. Jen, N. A. Clark, P. S. Pershan, and E. B. Priestley, J. Chem. Phys. **66**, 4635 (1977).

[11] C. H. Wang, *Spectroscopy of Condensed Media* (Academic, London, 1985).

[12] *The molecular dynamics of liquid crystals*, *NATO ASI series, ser. C. Mathematical and Physical Sciences; Vol. 431*, edited by G. R. Luckhurst and C. A. Veracini (Kluwer Academic, Dordrecht, 1994).

[13] M. Constant and D. Decoster, J. Chem. Phys. **76**, 1708 (1982).

[14] K. H. Kim *et al.*, Jpn. J. Appl. Phys., Part 1 **33**, 5850 (1994).

[15] R. Seeliger, H. Haspeklo, and F. Noack, Mol. Phys. **49**, 1039 (1983).

[16] K. Miyano, J. Chem. Phys. **69**, 4807 (1978).

[17] S. N. Prasad and S. Venugopalan, J. Chem. Phys. **75**, 3033 (1981).

[18] G. R. Luckhurst and R. N. Yeates, J. Chem. Soc. Faraday Trans. II **72**, 996 (1976).

[19] S. Miyajima and T. Hosokawa, Phys. Rev. B **52**, 4060 (1995).

[20] T. Nakai, H. Fujimori, D. Kuwahara, and S. Miyajima, J. Phys. Chem. B **103**, 417 (1999).

[21] K. H. Kim, K. Ishikawa, H. Takezoe, and A. Fukuda, Phys. Rev. E **51**, 2166 (1995).

[22] M. P. Fontana, B. Rosi, N. Kirov, and I. Dozov, Phys. Rev. A **33**, 4132 (1986).

[23] B. Park *et al.*, Jpn. J. Appl. Phys., Part 1 **38**, 1474 (1999).

[24] R. B. Meyer, L. Liebert, L. Strzelecki, and P. Keller, J. Phys. Lett. (France) **36**, L69 (1975).

[25] A. D. L. Chandani *et al.*, Jpn. J. Appl. Phys., Part 2 **27**, L729 (1988).

[26] A. D. L. Chandani *et al.*, Jpn. J. Appl. Phys., Part 2 **28**, L1261 (1989).

[27] M. Fukui *et al.*, Jpn. J. Appl. Phys., Part 2 **28**, L849 (1989).

[28] A. D. L. Chandani *et al.*, Jpn. J. Appl. Phys., Part 2 **28**, L1265 (1989).

[29] J. Lee *et al.*, Jpn. J. Appl. Phys., Part 1 **29**, 1122 (1990).

[30] K. Hiraoka *et al.*, Jpn. J. Appl. Phys., Part 2 **30**, L1819 (1991).

[31] E. Gorecka *et al.*, Jpn. J. Appl. Phys., Part 1 **29**, 131 (1990).

[32] K. Hiraoka *et al.*, Jpn. J. Appl. Phys., Part 2 **29**, L103 (1990).

[33] J. Lee *et al.*, J. Phys.: Condens. Matter **2**, SA271 (1990).

[34] P. Mach *et al.*, Phys. Rev. Lett. **81**, 1015 (1998).

[35] P. Mach *et al.*, Phys. Rev. E **60**, 6793 (1999).

[36] N. Okabe *et al.*, Jpn. J. Appl. Phys., Part 2 **31**, L793 (1992).

[37] P. Bak, Phys. Today **December**, 38 (1986).

[38] P. Bak and J. von Boehm, Phys. Rev. B **21**, 5297 (1980).

[39] Y. Ouchi, H. Takezoe, and A. Fukuda, Jpn. J. Appl. Phys., Part 1 **26**, 1 (1987).

[40] P. E. Cladis and H. R. Brand, Liq. Cryst. **14**, 1327 (1993).

[41] J. feng Li *et al.*, Phys. Rev. B **52**, R13075 (1995).

[42] X. Y. Wang *et al.*, Phys. Rev. Lett. **80**, 4478 (1998).

[43] S. Inui *et al.*, J. Mater. Chem. **6**, 671 (1996).

[44] L. K. M. Chan *et al.*, in *20 th Int. Display Research Conf. IDRC 2000 (Palm Beach, Florida)* (2000).

[45] T. Yoshida *et al.*, in *Conf. Summaries of FLC '99 (Darmstadt, Germany)* (1999).

[46] J. Ogura *et al.*, in *IDW '99 (Sendai, Japan) Digest* (1999).

[47] T. Yoshida *et al.*, in *IDW '00 (Kobe, Japan) Digest* (2000).

[48] R. Hasegawa, H. Yamaguchi, R. Fukushima, and K. Takatoh, in *Conf. Summaries of FLC '99 (Darmstadt, Germany)* (1999).

[49] R. Hasegawa *et al.*, Journal of the SID **9/2**, 107 (2001).

[50] A. Fukuda, in *Proc. Asia Display '95 (Hamamatsu, Japan)* (Soc. for Information Display, Santa Ana, CA, 1995).

[51] T. Matsumoto *et al.*, J. Mater. Chem. **9**, 2051 (1999).

[52] M. Takeuchi *et al.*, Ferroelectrics **246**, 1 (2000).

[53] S. S. Seomun *et al.*, Jpn. J. Appl. Phys., Part 1 **36**, 3586 (1997).

[54] H. Takezoe *et al.*, in *Proc. Asia Display '98 (Seoul, Korea)* (Soc. for Information Display, Santa Ana, CA, 1998).

[55] B. Park *et al.*, Phys. Rev. E **59**, R3815 (1999).

[56] P. Rudquist *et al.*, J. Mater. Chem. **9**, 1257 (1999).

[57] N. A. Clark, D. Coleman, and J. E. Maclennan, Liq. Cryst. **27**, 985 (2000).

[58] M. Lax and D. F. Nelson, Phys. Rev. B **4**, 3694 (1971).

[59] M. Lax and D. F. Nelson, J. Opt. Soc. Am **65**, 668 (1975).

[60] R. Akiyama, M. Hasegawa, A. Fukuda, and E. Kuze, Jpn. J. Appl. Phys., Part 1 **20**, 2019 (1981).

[61] G.-P. Chen, H. Takezoe, and A. Fukuda, Jpn. J. Appl. Phys., Part 1 **28**, 56 (1989).

[62] S. Asahina *et al.*, Liq. Cryst. **23**, 339 (1997).

[63] K. Hori and K. Endo, Bull. Chem. Soc. Jpn. **66**, 46 (1993).

[64] T. Nakai *et al.*, J. Phys. Chem. B **103**, 406 (1999).

[65] M. A. Osipov and A. Fukuda, Phys. Rev. E **62**, 3724 (2000).

[66] J. W. Goodby, J. Mater. Chem. **1**, 307 (1991).

[67] G. Heppke, P. Kleineberg, and D. Lotzsch, Liq. Cryst. **14**, 67 (1993).

[68] K. Miyachi *et al.*, Phys. Rev. E **52**, R2153 (1995).

[69] A. Fukuda *et al.*, Mol. Cryst. Liq. Cryst. **303**, 379 (1997).

[70] M. Johno *et al.*, Jpn. J. Appl. Phys., Part 2 **29**, L111 (1990).

[71] V. Laux *et al.*, Ferroelectrics **179**, 25 (1996).

[72] J. Li, H. Takezoe, and A. Fukuda, Jpn. J. Appl. Phys., Part 1 **30**, 532 (1991).

[73] K. Hiraoka *et al.*, Jpn. J. Appl. Phys., Part 2 **29**, L1473 (1990).

[74] M. Frisch, J. Foresman, and A. Frisch, *Gaussian 94, Development version* (Gaussian, Inc., Pittsburgh, PA, 1994).

[75] E. Sackmann *et al.*, J. Am. Chem. Soc. **90: 13**, 3567 (1968).

[76] K. Kondo, H. Takezoe, A. Fukuda, and E. Kuze, Jpn. J. Appl. Phys., Part 1 **21**, 224 (1982).

[77] K. H. Kim *et al.*, Liq. Cryst. **16**, 185 (1994).

[78] N. A. Clark and S. T. Lagerwall, Appl. Phys. Lett. **36**, 899 (1980).

[79] A. Fukuda *et al.*, J. Mater. Chem. **4**, 997 (1994).

[80] I. Nishiyama and J. W. Goodby, J. Mater. Chem. **2**, 1015 (1992).

[81] M. Johno *et al.*, Jpn. J. Appl. Phys., Part 2 **29**, L107 (1990).

[82] X. Y. Wang, T. Kyu, A. M. Rudin, and P. L. Taylor, Phys. Rev. E **58**, 5919 (1998).

[83] T. Qian and P. L. Taylor, Phys. Rev. E **60**, 2978 (1999).

[84] S. Zhang *et al.*, Phys. Rev. Lett. **84**, 4140 (2000).

[85] B. Wen *et al.*, Phys. Rev. E **62**, 8152 (2000).

[86] N. Hayashi and T. Kato, Phys. Rev. E **63**, 021706 (2001).

[87] N. Hayashi *et al.*, Phys. Rev. Lett. **87**, 015701 (2001).

[88] N. Hayashi *et al.*, Phys. Rev. E **65**, 041714 (2002).

[89] P. G. D. Gennes and J. Prost, *The Physics of Liquid Crystals*, second edition ed. (Clarendon Press, Oxford, 1993).

[90] R. N. Zare, *Angular momentum : understanding spatial aspects in chemistry and physics*, *VT:Baker lecture series* (Wiley, New York, 1987).

[91] L. A. Parry-Jones and S. J. Elston, Phys. Rev. E **63**, 050701(R) (2001).

[92] L. A. Parry-Jones and S. J. Elston, Appl. Phys. Lett. **79**, 2097 (2001).

[93] N. J. Mottram and S. J. Elston, Phys. Rev. E **62**, 6787 (2000).

[94] S. Zhang *et al.*, Phys. Rev. E **62**, R5911 (2000).

[95] S. S. Seomun *et al.*, Appl. Phys. Lett. **79**, 940 (2001).

[96] M. Yamashita, J. Phys. Soc. Jpn. **65**, 2122 (1996).

[97] M. Nakagawa and T. Akahane, J. Phys. Soc. Jpn. **55**, 1516 (1986).

[98] C. Tanaka, T. Fujiyama, T. Maruyama, and S. Nishiyama, in *Abst. of 21st Jpn. Liq. Cryst. Conf. (Sendai, Japan)* (Japanese Liquid Crystal Society, Tokyo, 1995).

[99] P. E. Cladis and H. R. Brand, Ferroelectrics **213**, 63 (1998).

[100] S.-S. Seomun *et al.*, Liq. Cryst. **26**, 151 (1999).

[101] D. Pociecha, M. Glogarova, E. Gorecka, and J. Mieczkowski, Phys. Rev. E **61**, 6674 (2000).

[102] E. Gorecka, D. Pociecha, M. Glogarova, and J. Mieczkowski, Phys. Rev. Lett. **81**, 2946 (1998).

[103] S. S. Seomun *et al.*, J. Mater. Chem. **10**, 2791 (2000).

[104] S. S. Seomun *et al.*, Phys. Rev. E **64**, 040701(R) (2001).

[105] S. Jen, N. A. Clark, and P. S. Pershan, Phys. Rev. Lett. **31**, 1552 (1973).

[106] A. Fukuda *et al.*, in *AD/IDW '01 (Nagoya, Japan) Digest* (2001).

[107] T. Matsumoto *et al.*, Jpn. J. Appl. Phys., Part 2 **40**, L817 (2001).

Publication List

“Investigation of orientational order for an antiferroelectric liquid crystal by polarized Raman scattering measurements”, N. Hayashi and T. Kato, Physical Review E **63**, 021706 (2001).

“Probable Langevin-like director reorientation in an interface-induced disordered SmC*-like state of liquid crystals characterized by frustration between ferro- and antiferroelectricity”, N. Hayashi, T. Kato, T. Aoki, T. Ando, A. Fukuda, and S. S. Seomun, Physical Review Letter **87**, 015701 (2001).

“Orientational distributions in smectic liquid crystals showing V-shaped switching investigated by polarized Raman scattering”, N. Hayashi, T. Kato, T. Aoki, T. Ando, A. Fukuda, and S. S. Seomun, Physical Review E **65**, 041714 (2002)

“Molecular ordering deformation induced by externally applied electric field in an antiferroelectric liquid crystal”, N. Hayashi, T. Kato, T. Ando and A. Fukuda, Japanese Journal of Applied Physics **41**, 5292 (2002).

Other Publications

"Electrophoretic light scattering of alkyl- and oleyldimethylamine oxide micelles", T. Imae and N. Hayashi, Langmuir **9**, 3385 (1993).

"State correlated Raman spectroscopy", Naoki Hayashi and Tatsuhisa Kato, Proceedings of the International Conference of the Two-Dimensional Correlation Spectroscopy, Eds., Y. Ozaki and I.Noda, American Institute of Physics, New York (1999).

"Structures of fibrous supramolecular assemblies constructed by amino acid surfactants: Investigation by AFM, SANS, and SAXS", T. Imae, N. Hayashi, T, Matsumoto, T. Tada and M. Furusaka, Journal of Colloid and Interface Science **225**, 285 (2000).

"Surface molecular alignment by in-plane anchoring in the cell showing the V-shaped switching", S. S. Seomun, J. K. Vij, N. Hayashi, T. Kato and A. Fukuda, Applied Physics Letter **79**, 940 (2001).